Fracture Prediction of Fully Clamped Circular Brittle Plates Subjected to Impulsive Loadings

Lingjie Cai

This thesis is submitted for partial consideration
towards the degree of Doctor of Philosophy

in

The department of civil and structural engineering
at the university of Sheffield

Thursday 16th March, 2023

I would like to dedicate this thesis to Luyao ...

Acknowledgements

Firstly, I would like to thank my PhD supervisors, Dr. Sam Rigby and Prof. Luca Susmel for their support, guidance and friendship throughout my PhD. The quality of the work owes much to their dedication and attention to detail and I hope we will keep in touch.

Also I would like to thank Prof. Sam Clarke for his input on the suggestions for my teaching and demonstration. Thanks also to the rest of the Blast and Impact Dynamics group, I will hold fond memories of the spontaneous trips to the Red Deer, the Forum, the Lane 7 and the Head of Steam!

The research is funded by the Faculty of Engineering at the University of Sheffield, thanks to the panel who chose me.

I would like to thank my parents for their agreement on my leave for four years. I would also like to thank my parents-in-law, Huisheng Yang and Chunmei Gao for their support throughout. Finally, I would like to thank my wife, Luyao Yang. Thanks for your four years of company. Thanks for all the delicious dishes cooked for me. I owe you a wedding. Let's go for it after my graduation!

Abstract

When a high explosive detonates at some distance from the structure, the generated hot gas with high magnitude pressure and temperature expand rapidly and force the surrounding air out of the volume it occupies. As a consequence, a high pressure shock discontinuity namely a shock wave is produced. As this shock propagates away from the charge, it may inflict widespread damage to any structure that it impacts on. It is the challenge of structural engineers to improve the blast-resistant performance of the vulnerable structures and design adequate and efficient protective engineering systems against such extreme loading.

Most of studies on the response of plate subjected to blast loadings focus on the transient or permanent deformation without any failure occur. Available methods in the literature for predicting failure response only works for one specific load distribution while distribution of blast loadings could be significantly due to various scenarios. Predictive method are therefore required that can predict the failure response of plates under loading with arbitrary distribution and intensity that are fast to run and accurate.

Conducting the experimental research dealing with blast loads needs to consider both cost and safety issues. Besides, numerical analysis requires a high computational time. Therefore, the given analytical approach provides an alternative for failure response investigation.

This thesis proposes an analytical method to predict failure response of plates under more than one specific loading distribution. Besides, this thesis provides dimensionless $I - K$ diagrams that could quickly determine the potential failure modes a plate will suffer under the given blast loading.

The results of this thesis should be used to guide analytical approach development for the prediction of failure response of plates subjected to blast loadings. The simple method developed in this thesis can be employed for design purposes, especially, at the early stages requiring an understanding of the structural failure response and help to rapid evaluation of the likely damage a structure will sustain in the event of blast.

Contents

List of Figures

List of Tables

Nomenclature

Greek Symbols

ψ_r	angular rotation of the normal to the neutral surface in the radial direction
ψ_θ	angular rotation of the normal to the neutral surface in the circumferential direction
α	$\frac{1-\nu^2}{\nu}$
β	$\frac{c_p}{c_s}$
γ_{ij}	shear strain
γ_{xz}	transverse shear strain
γ_{yz}	transverse shear strain
γ_z	transverse normal stress
κ	shear correction factor
ν	poison ratio
ω	transverse displacement
π	$\simeq 3.14\ldots$
ρ	density
σ_{ii}	normal stress
σ_i	normal stress with single subscript
τ	dimensionless time, $\frac{tc_p\sqrt{12}}{h}$
τ_{ij}	shear stress
u_θ	angular displacement

ε_{ii} normal strain

ε_i normal strain with single subscript

ε_z transverse normal strain

ξ dimensionless radial coordinate, $\frac{r\sqrt{12}}{h}$

Other Symbols

δM finite value

$\dot{x}_0$ initial velocity

$\overline{M}$ $\frac{M_r h}{D}$

$\overline{N}$ $\frac{M_\theta h}{\nu D}$

$\overline{P}$ $\frac{Ph^3}{12D}$

$\overline{Q}$ $\frac{Q_r h^2}{D\sqrt{12}}$

$\overline{V}$ $\frac{V\sqrt{12}}{\beta c_p}$

$\overline{W}$ $\frac{Wh}{c_p}$

θ angular coordinate

A plate area

D flexural rigidity

E Young's modulus

e volumetric strain given by $\varepsilon_x + \varepsilon_y + \varepsilon_z$

E_k kinetic energy

E_{kl} lower bound kinetic energy

E_{ku} upper bound kinetic energy

F triangular pulse

$F(t)$ a spatially uniform load

$F_{e,max}$ linearly-decaying peak force

$F_e(t)$ equivalent load

G shear modulus

h thickness of the plate

I impulse for positive phase duration

I total impulse

i impulse

i specific impulse

K impulse enhancement factor

K_0 an empirical constant which differs depending on the specified damage level

K_L load transformation factor

K_M mass transformation factor

K_S stiffness transformation factor

k_e equivalent stiffness

KE kinetic energy

L span of the simply supported structure

λ_i eigenvalue

L^i left eigenvector

M_r resultant moment in radial direction

$M_{r\theta}$ resultant twisting moment

M_θ resultant bending moment in circumferential direction

M_e equivalent mass

M_a Moment at the point a

M_b Moment at the point b

M_r fracture criterion for radial bending

M_θ fracture criterion for circumferential bending

P transverse pressure

p_0 ambient air pressure

$p_{so,max}$ peak overpressure

$p_{so,min}$ negative phase peak overpressure

Q_r resultant shear force in radial direction

Q_θ resultant shear force in circumferential direction

p_0 radial coordinate

R threshold safe stand-off in metres

R_u resistance of the SDOF system

T natural period

t time

t_d positive phase duration

$t_{d,lin}$ linearly-decaying load duration

t_{d^+} positive phase duration

t_{d^-} negative phase duration

θ_{max} maximum normal stress

U strain energy

u displacement along x coordinates

u_r radial displacement

V transverse velocity

v displacement along y coordinates

v initial velocity

W angular rotation velocity

W charge mass in kg TNT

w displacement along z coordinates

x_{max} maximum displacement is at midspan

x_{st} the static displacement that would result if the force F were applied as a static load

z transverse coordinate

z_E elastic limit

z_{max} peak dynamic deflection

d_t taper length

R thickness of explosive sheet

R plate radius

r radial coordinate

V peak velocity

Acronyms / Abbreviations

$CFRP$ Carbon Fibre Reinforced Polymer

DIC Digital Image Correlation

DLF Dynamic Load Factor

FEM finite element method

$FFLD$ Fracture Forming Limit Diagram

LN linen phenolic

MOC method of characteristics

MSS Maximum Shear Stress

ODE ordinary differential equation

PDE partial differential equation

$PMMA$ polymethylmethylmethacrylate

$SDOF$ Single Degree of Freedom

$SETF$ Specific Energy to Tensile Fracture

YEM Youngdahl Equivalent Method

Chapter 1

Introduction

THIS PhD thesis will work towards developing a better understanding of the failure behaviour of the blast-induced plate and providing a novel method capable of predicting its failure behaviour with reasonable accuracy.

This chapter will serve to outline the structure of the thesis, its motivation, its objectives as well as the original contributions.

1.1 Background and Motivation

Terror attacks on critical infrastructure and vulnerable targets using a range of explosives, e.g., from large vehicle-borne explosives to small hand-held devices, is among the most serious security challenges facing the international community today – and it is ever more and more common over the past few decades (Feyerabend 1996; Keane and Esper 2009; Ganguly 2009; Ben-Ezra et al. 2017; Jureńczyk 2018; Shrestha and Fluri 2023). On the morning of April 19, 1995, a truck packed with around 3,000 kg of high explosives was detonated at the north entrance of the Alfred P. Murrah Federal Building in downtown Oklahoma City, USA. As a result, the explosion and partial collapse of the nine-story building killed 168 people including 19 children, injuring approximately 850, with 219 children lost at least one parent and seven thousand people lost their workplace (Flynn 1995). It was reported that the blast destroyed or damaged 324 other buildings within a 16 block radius, shattered glass in 258 nearby buildings, causing an estimated 652 million worth of damage (Mehreganian et al. 2019b). Similar examples of high-casualty terrorist attacks on buildings and critical infrastructure are shown in Table 1.1 (Micallef et al. 2014; Wang et al. 2022; Zhang et al. 2013; Li and Meng 2002; Chen et al. 2017).

Another concern for the blast protection community, except the malicious attacks, is the accidental explosions which caused by modern high explosives, boiling liquid expanding vapour explosions, gunpowder and other chemical reactions [i]. Several notable accidental explosions have occurred in recorded history, with disastrous results, such as Hemel Hempstead, U.K. (2005); Tianjin, China (2015) and Beirut, Lebanon (2020). Thus, it becomes imperative to critically assess blast resistance of structures that may not have been designed to resist explosions, such as crucial civilian as well as governmental and defence buildings and structures.

The complex nature and the intrinsic large uncertainties characterizing blast loads makes the design and analysis of a building against these loads beyond the scope of traditional civil engineering. It is vital, therefore, that research into quantification of the effects of blast loading on structures is focused on methods for rapid evaluation of the likely damage a structure or a structural component will sustain in the event of an accidental or malicious explosion. The field of blast protection engineering, however, is held back by one key issue: we are currently unable to determine how a blast load will cause a protective system to fail. Without this knowledge, we are unable to provide adequate and efficient protection systems and the level of scientific understand within this field remains limited.

This thesis presents research which will contribute to the existing knowledge of quantifying blast effects on structures and demonstrates the development of an engineering tool for rapidly blast damage prediction. It is the hope of this author that the research findings will be able to supplement existing predictive methodologies and assist designers make better-informed responses to risks originating from blast threats.

[i] Regulations used for blast design such as American Society of Civil Engineers (ASCE) 59-11: This code provides guidelines for designing buildings to resist explosive loads, including those caused by vapor explosions and chemical explosions; Unified Facilities Criteria (UFC) 3-340-02: This document, published by the US Department of Defense, provides design requirements and procedures for buildings that are exposed to blast loads, including those caused by accidental explosions. It covers structural design, materials selection, and detailing requirements for reinforced concrete, masonry, and steel structures; International Building Code (IBC): The IBC includes provisions for designing buildings to withstand various types of hazards, including those caused by explosions. It provides minimum requirements for structural design, as well as guidelines for material selection and detailing

Date	Target	Delivery method	F[a]	I[b]	Details
3/7/2016	Karada Shopping Centre, Baghdad, Iraq	Suicide truck bombing	342	246	Suicide bombers detonated a refrigerator van packed with explosives at a shopping centre. Several buildings were badly damaged.
31/5/2017	German Embassy, Kabul, Afghanistan	Truck bombing	150	413+	A truck bomb filled with about 1,500 kilograms of explosives exploded in a crowded intersection in Kabul near the German embassy during rush hour, damaging several buildings in the embassy.
27/1/2018	Kabul's and European Union Embassies, Kabul, Afghanistan	Vehicle-borne improvised explosive device	104	235	A suicide bomber detonated an explosives-laden truck outside the Safari Hotel which is near Kabul's embassies and the European Union embassies. The shock was felt around the capital, collapsing buildings and destroying façades in the immediate area
7/8/2019	Police Stations, Kabul, Afghanistan	Suicide vest	14	145	Suicide car bombs exploded outside a police station and a nearby military training school, destroying all windows in a radius of a mile
26/8/2021	Kabul International Airport, Kabul, Afghanistan	Suicide vest	170	150+	A suicide bomber detonated a vest with 11.3 kilograms of explosives at Kabul International Airport.

[a] Fatalities
[b] Injuries

Table 1.1: Examples of recent terrorist attacks on critical infrastructures and buildings using high explosives (Micallef et al. 2014; Wang et al. 2022; Zhang et al. 2013; Li and Meng 2002; Chen et al. 2017)

1.2 Scope and Objectives of the Thesis

This thesis aims to develop an analytical method for predicting the damage pattern of plates arising from a high explosive blast and its dependence on the magnitude and distribution of loading. A breakdown of the objectives that will be implemented to achieve this aim is described as follows:

1. Review the existing literature on predictive approaches for failure response of blast-loaded plates and discuss the limitations of existing approaches.

2. Develop an analytical model to predict fracture patterns of brittle plates subjected to impulsive loadings and their dependence on the magnitude and distribution of load. The quantitative relationship between loading and the failure behaviour will be explored.

3. Evaluate the performance of the newly developed analytical method through finite element modelling. Analytical predictions will be compared with simulation results in terms of fracture time, fracture initiation location and fracture pattern.

4. Further investigate the effect of loading distribution and magnitude on the failure response of blast-loaded plates to generalize the predictive method for predicting failure behaviour of plates under arbitrary loading.

5. Conduct a parametric study to investigate the influence of boundary conditions and plate geometry on the failure behaviour of plates subjected to blast loadings with various distributions and intensity.

1.3 Thesis Outline

The remainder of the thesis is organised into the following chapters:

Chapter 2 – Literature Review and Theoretical Background

This chapter provides background information for explosive blast loading and blast loadings effects on structures. Current literature relating to the evaluation of plate theories and deformation and failure response of blast-loaded plates is reviewed, as well as a discussion on the limitations of the existing predictive methods. This chapter will meet objective 1 in section 1.2.

Chapter 3 – Analytical Method for Failure Prediction

This chapter describes the development of an analytical solution that can be used to predict the failure behaviour of brittle plates under impulsive loadings with a certain form. Quantification of the effect of both loading distribution and magnitude on the failure modes are studied. This chapter will meet objective 2 in section 1.2.

Chapter 4 – Verification of Analytical Method

This chapter provides a preliminary validation of the method developed in Chapter 3 against available experimental data from the literature review. Additionally, further verification is performed by using the chosen finite element software to generate numerical data for response of blast-loaded plates and is compared against predicted results from the analytical method. This chapter will meet objective 3 in section 1.2.

Chapter 5 – Failure Response of Impulsively Loaded Plates

The failure response of brittle plates subjected to blast loads with a variety of distribution and magnitude is evaluated for a range of loading forms in an attempt to both understand and quantify the influence of distribution and intensity, and also to develop and provide detailed guidance on the likely failure pattern a given plate will sustain for a blast load with given form and magnitude. This chapter will meet objective 4 in section 1.2.

Chapter 6 – Summary and Conclusions

This chapter summarises the current research and makes suggestions for future work.

Chapter 2

Literature Review and Theoretical Background

THIS chapter gives background information for explosive blast loading and blast effects on structures, as well as reviewing current literature pertinent to the subjects covered in this thesis. The predominant focus of this chapter is to provide theoretical knowledge in assessing the behaviour of a blast-loaded structure, with a particular focus on existing theories and methods for predicting deformation and failure of plates when subjected to blast loads. Some key concepts and theories are presented as well in order to define a knowledge framework from which to start the current study and identify the gaps in current understanding.

2.1 Explosive Blast Loading

2.1.1 Overview

Explosive loading is generated when energy is suddenly released to the surrounding environment leading to the development of transient pressures on structures or buildings. The features of explosive blast loading are:

- Extremely high magnitude [i]
- Transient loading applied and removed quickly [ii]
- Usually only applied to localised parts of a structure
- Loading decays rapidly with distance [iii]
- Low predictability and low likelihood

Generally, the sources of blast loading can be classified into four categories: terrorist devices, unexploded ordinance, industrial accidents and nuclear energy. Among these sources, the first three result from chemical energy release as intermolecular bonds are broken during oxidation (Tyas 2014). Nuclear events are different to chemical events in that they can be assumed to release all their energy as a point source. In a nuclear explosion, the energy released arises from the formation of different atomic nuclei by the redistribution of the protons and neutrons within the interacting nuclei (Cormie et al. 2009). Nuclear explosions are not typically considered within the remit for civilian blast protective engineering and therefore, outside the scope of this thesis.

2.1.2 Detonation and Air Shock Formation

Figure 2.1 shows a basic schematic of the detonation process in a spherical charge. A high velocity detonation wave is set up and moving through the explosive away from the point of detonation as a result of the vaporisation of the detonator that used to initiate the parent explosive charge. This detonation wave compresses the surrounding material, breaking the chemical bonds in an extremely exothermic reaction which increases the density, temperature and pressure behind the wave front. The wave front is continually reinforced by the reaction energy from material just ahead of it until the boundary between explosive and surrounding medium is reached. Typically the reaction front

[i] The pressure of explosive loading can range from a few hundred to hundreds of thousands of kilopascals, depending on on several factors such as the type of explosive, the amount of explosive, and the intended application

[ii] The duration of blast loading is relatively short, typically ranging from a few milliseconds to a few seconds. This is because the blast wave generated by an explosion travels at high speed and dissipates rapidly as it moves away from the source

[iii] For example, if the blast loading magnitude at a distance of 10 meters from the explosion is 100 kPa, then at a distance of 20 meters, it would be only 25 kPa (1/4th of the original value), and at a distance of 30 meters, it would be only 11.1 kPa (1/9th of the original value

travels at several 1000 m/s and the detonation product gases can be at pressures between $10 - 30$ GPa, and at a temperature of $3000 - 4000°C$ (Cormie et al. 2009)

Once the detonation wave reaches the edge of the charge it reflects inwards as a rarefaction wave. The explosive materiel begins to expand into the surrounding air, forcing out the volume it occupies. In air, due to the compressibility of air, wave speed increases with increasing pressure (Cormie et al. 2009). As a result, higher pressures travel quicker and catch up with lower pressures. Eventually, there will be a near-instantaneous rise in pressure from ambient to peak – this is the shock front, as shown in Figure 2.2 (Baker 1973)

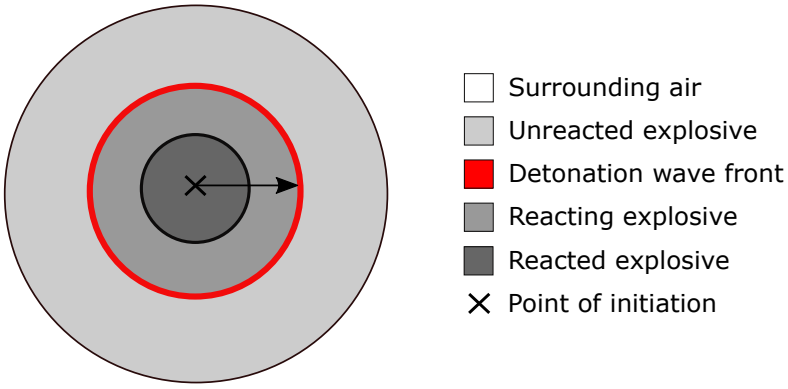

Figure 2.1: Detonation mechanism within the explosive

Increasing expansion results in an increase in blast energy absorption by the surrounding air and this energy loss causes a deceleration of the wave accompanied by a reduction in pressure and density at its front. The increased volume enveloped by the radiating blast wave also results in a pressure decrease behind the wave front as the explosive gases are able to expand, as shown in Figure 2.3.

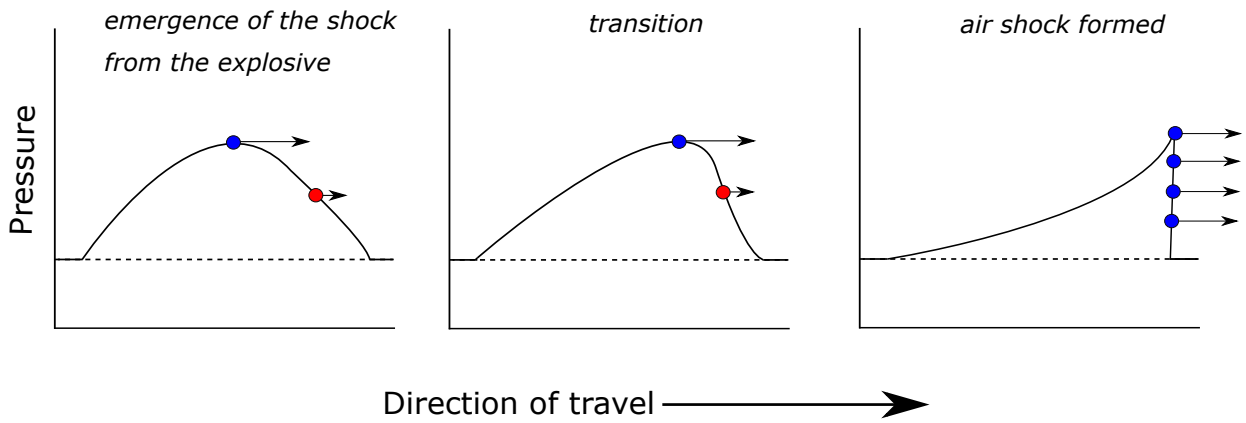

Figure 2.2: Development of explosive shock (arbitrary units) (Kinney and Graham 1985)

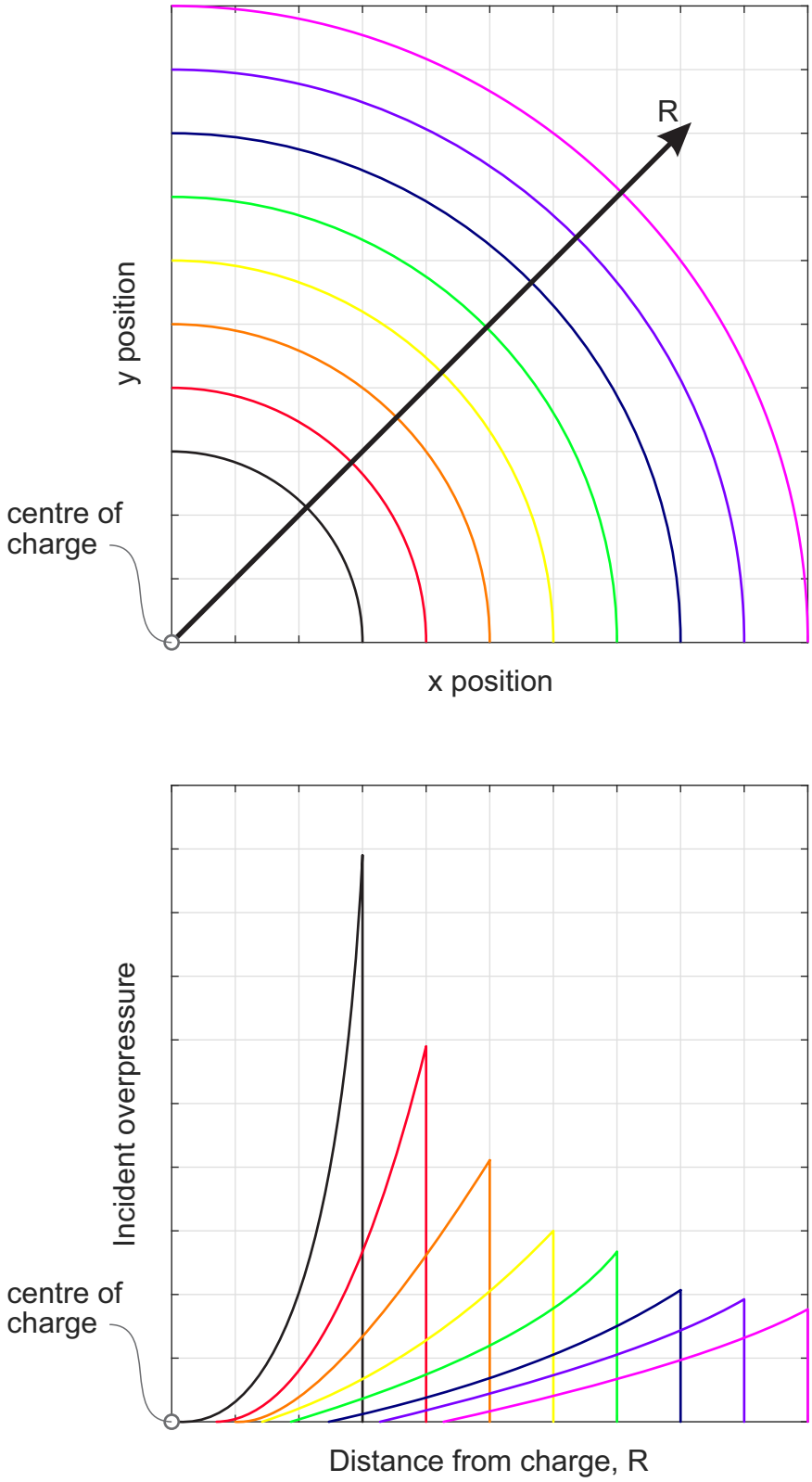

Figure 2.3: Pressure distributions observed along a radial line as a blast wave propagates (arbitrary units) (Rigby and Tyas 2021)

2.1.3 Blast Waves in Free Air

If a condensed high explosive detonates at a fixed distance, there will be an abrupt increase in pressure from ambient air pressure p_0 to peak overpressure, $p_{so,max}$, followed by a temporal decay back down to ambient pressure, the duration of which is known as the positive phase duration, t_{d^+} (Cormie et al. 2009). The subscript 'so' indicates incident pressure values, i.e. the pressure measured by a transducer that offers no resistance to flow behind the shock front, or by a shock wave propagating parallel, or 'side-on', to a reflecting surface. The term 'overpressure' refers to the pressure increase above normal atmospheric conditions (a pressure of 101 kPa).

Following the positive phase comes a period of negative (below atmospheric) pressure caused by over expansion of the air following the shock front, known as the negative phase, which has peak amplitude $p_{so,min}$ and duration t_{d^-}. The negative pressure cannot be greater than one atmosphere (101 kPa) but can often have a relatively long duration relative to the positive phase of the blast. After the negative phase, ambient pressure is restored. The impulse, i, is defined as the integral of the pressure with respect to time, i.e. the area under the pressure-time curve. Figure 2.4 presents a typical pressure-time profile for blast wave in free air.

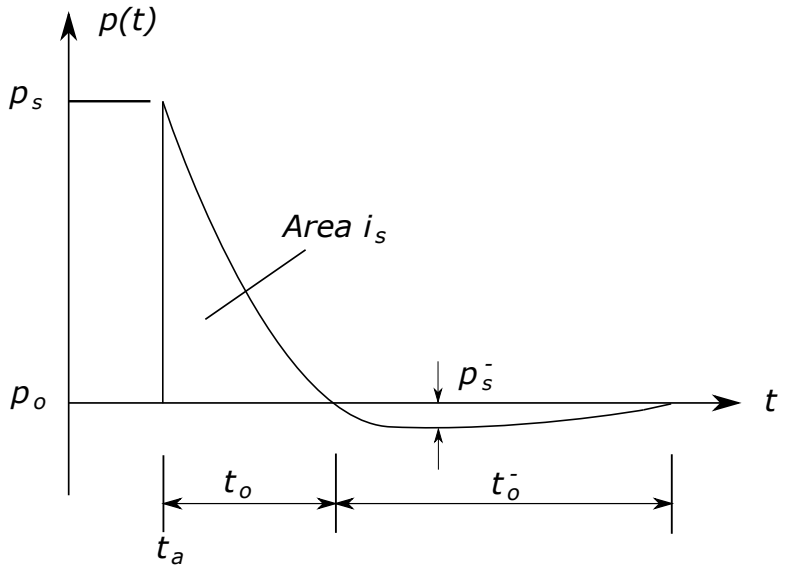

Figure 2.4: Typical pressure-time profile for blast wave in free air (arbitrary units), p_0 is the ambient air pressure (Hetherington and Smith 1994)

2.2 Effects of Blast Loading on Structures

2.2.1 Influence of Spatial Distribution

The rapid application and sudden high pressures associated with blast loading induces structural behaviour which is different to that observed under static loading. In addition, modes of structural response are influenced by the spatial distribution of the blast loading applied on the surface of the target structure. Typically, when distance from explosive to target is large compared to span of the panel, loading is approximately uniformly distributed across the span due to the low interaction curvature – this is termed as far-field loading. On the contrary, if distance from explosive to target is relative small compared to span of the panel, loading is highly concentrated near epicentre because of the resultant high interaction curvature – we call it near-field loading. Figure 2.6 shows the effect of blast interaction curvature on load distribution. A typical example shown in Figure 2.5 compares the distribution of blast loading parameters associated with far-field and near field loading.

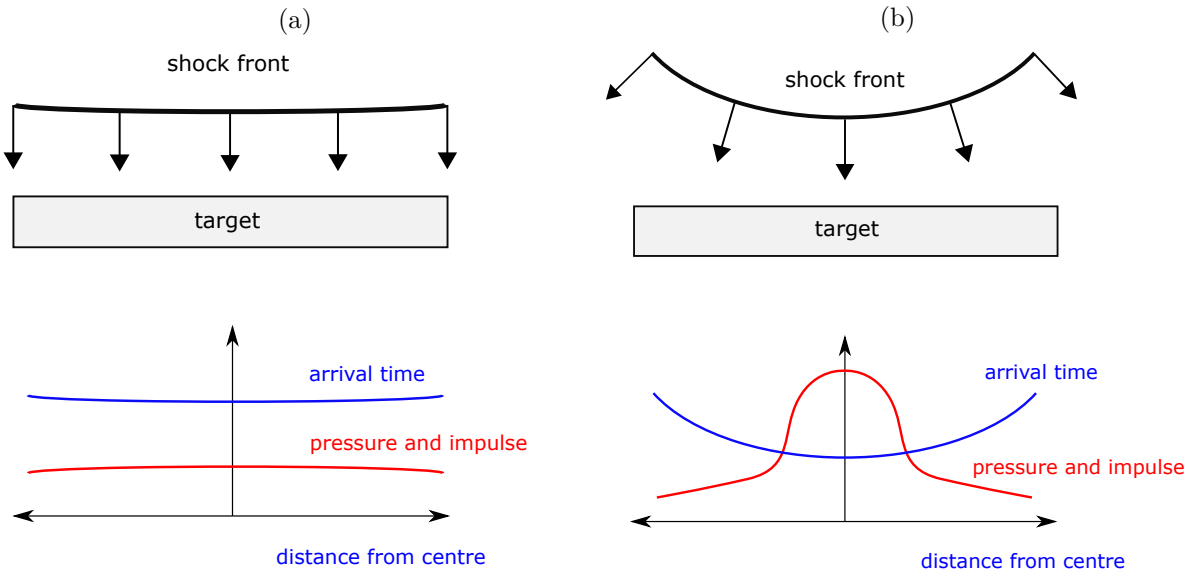

Figure 2.5: Blast interaction diagram and loading parameters associated with far-field (a) and near-field (b) blast loading (arbitrary units)

2.2.2 Modes of Deformation

Figure 2.6 shows the evolving deformation of a thin steel plate when exposed to a rapid far-field loading. If the plate was loaded gradually (statically) time would be available for the stiffness of the plate to transfer the stresses induced by the load so that an equilibrium could form between the load and the supports and the plate is able to deform in a single global mode. As the loading becomes more rapid, there is increasingly insufficient time for the development of global equilibrium and a transient deformation mechanism will evolve. In Figure 2.6a the loading is distributed evenly so that momentum is imparted uniformly across the span of the plate and all locations on the plate are initially mobilized with the same velocity. Motion is locally restricted in the region of the supports prompting the development of a hinge. As the centre of the plate continues to deflect the hinge migrates inward until, eventually, the familiar 'triangular' deflected shape associated with uniform static loading is formed (Rigby and Tyas 2021). Although the residual shape of the blast loaded plate may be similar to that produced by static loading, the mechanism for its development may be very different.

As illustrated by the reinforced concrete panel shown in Figure 2.6b, if the stresses developed at the supports exceed the shear strength of the structure during deformation, the main body of the panel will be punched through.

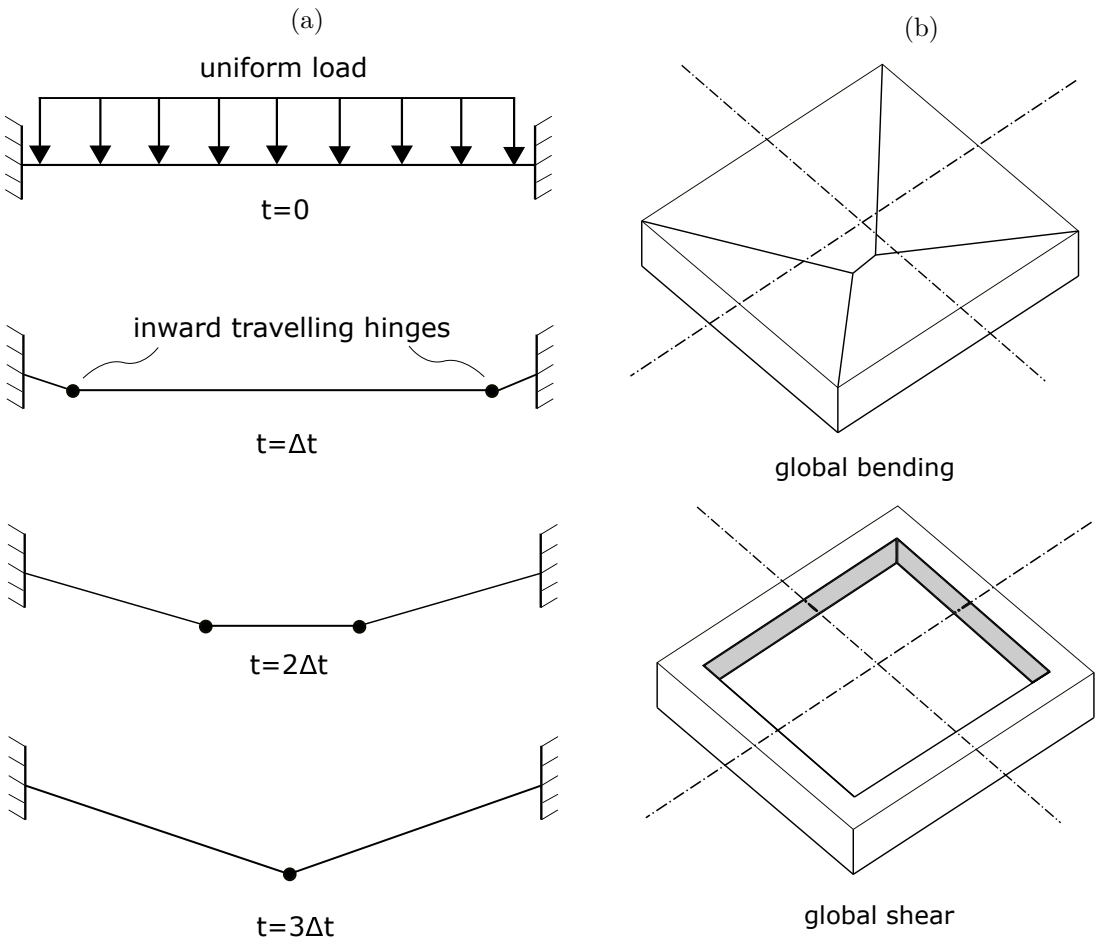

Figure 2.6: Evolving deformation of a steel plate exposed to far-field loading (a). Idealized far-field deformation modes in a reinforced concrete panel (b)

Figure 2.7 shows the evolving deformation of a thin steel plate when exposed to a near-field loading. The high interaction curvature of the loading, Figure 2.7a , means that the vast majority of the momentum is imparted directly under the blast causing epicentral region of the plate to be mobilized. Initially there is not enough time for the stress caused by this movement to be transferred to the supports and so a local dish forms bounded by an inertial support or hinge. If the plate is ductile, the hinge may subsequently travel outward toward the supports as the epicentrally-applied momentum exerts a pull on the plate to its exterior. The plate may eventually adopt a peak 'triangular' deformation shape similar to the observed in far-field loading as shown in Figure 2.6a but this is greatly dependent on its ability to 'spread' the momentum to the supports. In more brittle structures such as reinforced concrete panels, the in-plane velocity gradients generated by the localized momentum may cause local shear cracks through the thickness of the concrete. These effectively isolate the central concrete from the rest of the panel so that the final (or residual) deformation mode is a local dish or shear plug failure as illustrated by Figure 2.7b.

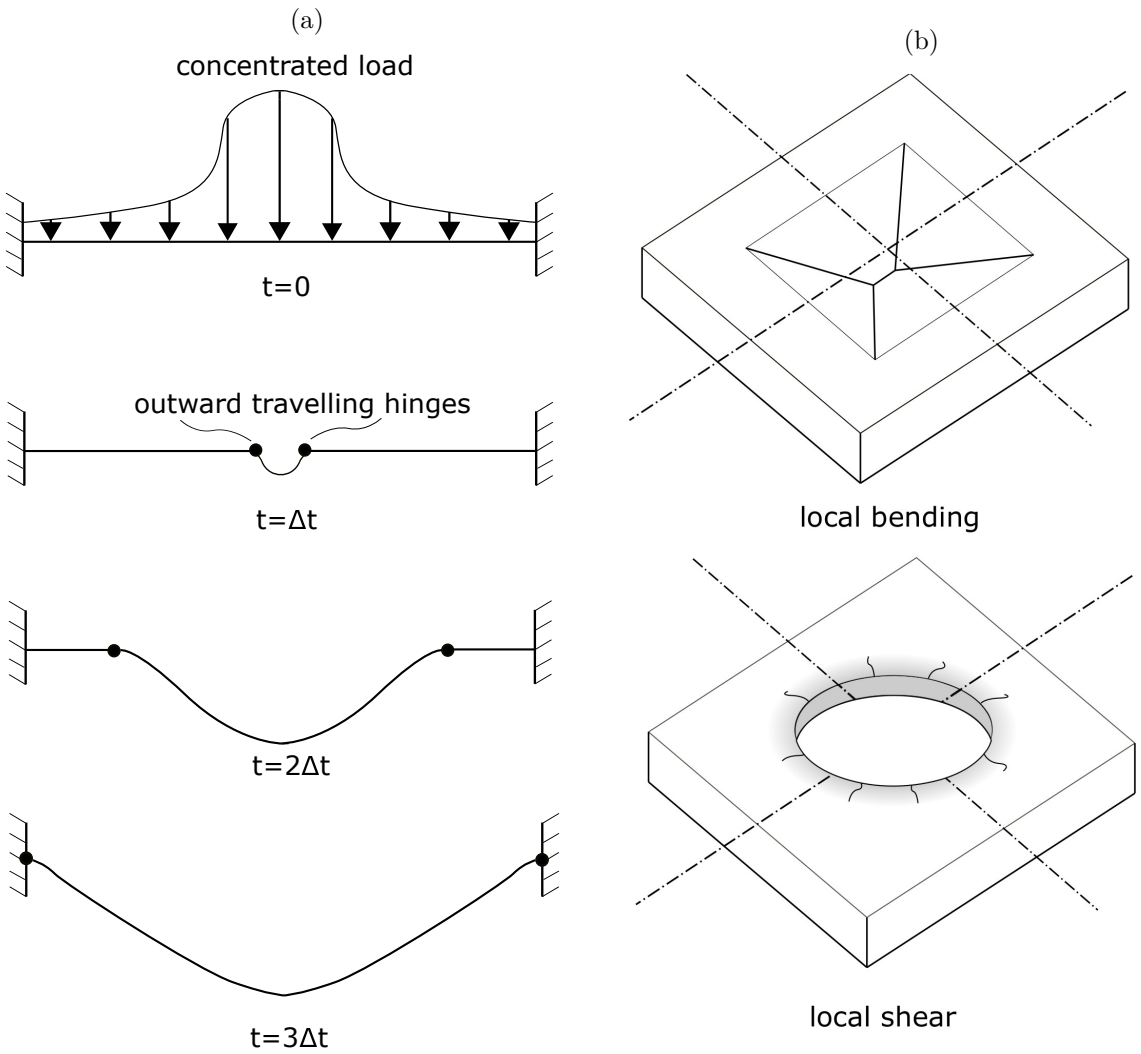

Figure 2.7: Evolving deformation of a steel plate exposed to near-field loading (a). Typical near-field deformation modes in a reinforced concrete panel (b)

2.2.3 Loading Realms

Depending on the duration of the applied load relative to the natural period of the target structure, structural response to blast loading can be defined as 'impulsive', 'dynamic' or 'quasi-static'. Knowing which of these loading realms we are in can be useful in helping us evaluate and predict the structural response.

Roughly speaking, consider a structure that is to be subjected to a blast load, we usually say it is an impulsive loading if the positive phase duration of the load t_{d^+} is less than tenth of the natural period of the structure T [iv]. Similarly, these three regimes can be summarized in terms of the ratio of t_{d^+} to T (Rigby and Tyas 2021):

- $\frac{t_{d^+}}{T}$ <0.1 Impulsive
- 0.1 < $\frac{t_{d^+}}{T}$ <10 Dynamic [v].
- $\frac{t_{d^+}}{T}$ >10 Quasi-static [vi].

[iv] More strictly speaking, if t_{d^+} is much shorter than T in which case there is no significant movement of the structure before the blast loading ends – we call it impulsive loading

[v] In this case, t_{d^+} is comparable to T, e.g., blast loading from gas explosions or confined high explosive charges is usually dynamic

[vi] Blast loading from high explosive detonations in free air air rarely quasi-static – the duration of the loading is usually only a few hundred microseconds to a few 10s of milliseconds

2.2.4 Current Best Practice

2.2.4.1 Equivalent System

Available techniques for predicting the response characteristics of a structure subjected to a blast load fall into three distinct categories; simplified numerical analysis, detailed numerical analysis and experimental tests.

Simplified numerical analysis, though the most limited-application methods, still have the popularity in some scenarios [vii]. as it is often the case that the calculation of final states is the principal requirement for an engineer instead of the full analytical description of the structural response. The principle of this analysis is to replace the real structure (e.g., a beam or slab) with a highly simplified equivalent mathematical model via an equivalent system. In the simplest form of equivalent system – Single Degree of Freedom (SDOF) model, the three dimensional properties of the real system are approximated as a one-dimensional system as shown in Figure 2.8. In Figure 2.8 a simply supported beam is subjected to a spatially uniform load $F(t)$ along the whole span L. The point of maximum displacement is at midspan, and is termed x_{max}. The structural stiffness of the beam M is replaced by a single massless spring with stiffness k_e, the distributed mass of the beam M by a lumped mass on the end of the spring M_e, and the distributed loading by a single point load applied to the mass $F_e(t)$.

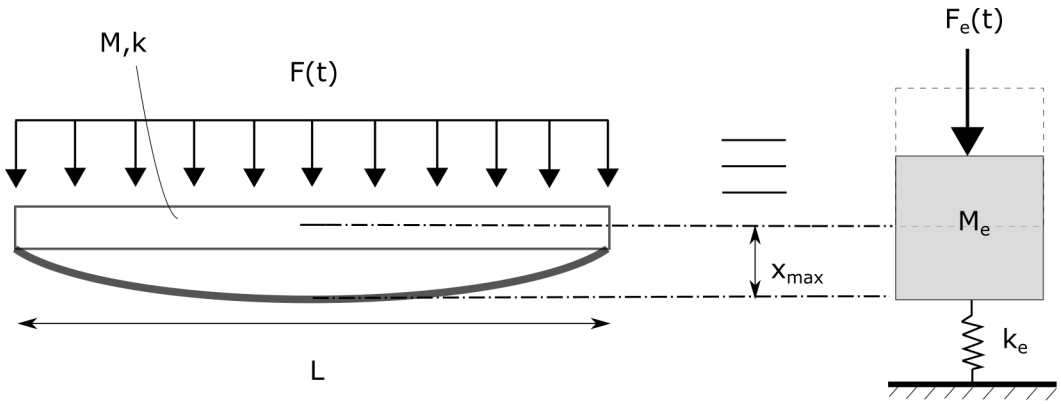

Figure 2.8: Real and equivalent SDOF systems

To make this highly simplified equivalent mathematical model to be a physically valid approximation, we must ensure that the work done by the load and the kinetic and strain

[vii] According to Semantic Scholar, at the time of writing this thesis 'An Introduction to Structural Dynamics' has been cited 1232 times. 274 of these citing articles have been published since 2017

energies generated by the structural response are identical in the real and equivalent systems. Hence, transformation factors are applied to the load, mass and stiffness to obtain the equivalent values which gives:

The equivalent system approach requires the analyst to assume a deflected shape for the structure. Common assumptions are elastic bending or rigid-plastic bending with perfect hinges.

$$F_e = K_L F \tag{2.1a}$$
$$k_e = K_S k \tag{2.1b}$$
$$M_e = K_M M \tag{2.1c}$$

where K_L, K_S and K_M are the load, stiffness, and mass transformation factors.

The transformation factors are found by taking a deflected shape for the deformed structure and integrating the shape function along the length of the structure, using the following equations:

$$K_L = \int_0^L \frac{\phi(x)\ dx}{L} \tag{2.2a}$$
$$K_S = \int_0^L \frac{\phi(x)\ dx}{L} \tag{2.2b}$$
$$K_M = \int_0^L \frac{\phi(x)^2\ dx}{L} \tag{2.2c}$$

where $\phi(x) = x/x_{max}$, defined as the normalised deformed shape profile.

If we consider a structure which has been idealised as an SDOF elastic structure and is to be subjected to a blast load idealised as a triangular pulse delivering a peak force F. This situation is illustrated in Figure 2.9. Here, we use t_d as the positive phase duration.

The load pulse $F(t)$ is described by the equation:

$$F(t) = F(1 - \frac{t}{t_d}) \tag{2.3}$$

This blast load will deliver an impulse I to the target structure given by the equation:

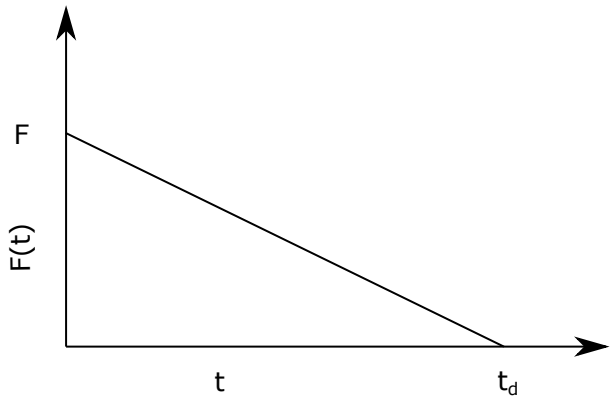

Figure 2.9: Idealised blast pulse

$$I = \frac{1}{2} F t_d \tag{2.4}$$

where I is the area beneath the load function for $0 < t \leq t_d$. In the absence of damping, the equation of motion for this structure is:

$$K_M M\ddot{x}(t) + K_S k x(t) = K_L F(1 - \frac{t}{t_d}) \tag{2.5}$$

If we confine the problem to response for times less than the positive phase duration, the solution can be written as:

$$x(t) = \frac{F}{k}(1 - cos\omega t) + \frac{F}{kt_d}(\frac{sin\omega t}{\omega} - t) \tag{2.6}$$

where $\omega = \sqrt{K_S k / K_M M}$ is the natural frequency of vibration of the structure.

Hence, the maximum dynamic displacement could be calculated by invoking the concept of derivative, i.e. equating the velocity of structure to zero.

2.2.4.2 Biggs Response Charts

Some predictive methods based on the SDOF model have been developed to assist the practising engineers to quickly evaluate the response of blast-loaded structures. One such method found in Introduction to Structural Dynamics (Biggs 1964), which are also available in design guidance (US Department of Defence 2008; Cormie et al. 2009), enable engineers to find the maximum dynamic deflection by simply read off the value from the charts if given the peak applied pressure and duration of the load, and the target material properties (mass, stiffness, yield strength) and span.

Cormie et al. (2009) presents the results from rigorous analysis of elastic-plastic SDOF systems subjected to linearly-decaying blast loads with peak force and load duration denoted by $F_{e,max}$ and $t_{d,lin}$ respectively.

The SDOF equation of motion was solved using explicit numerical time-stepping for various combinations of peak force and load duration. The peak force was varied between $0.5 - 10$ times the maximum spring resistance, R_u (i.e. the 'resistance ratio' of the equivalent SDOF system: $R_u/F_{e,max}$, varied between 0.1 and 2.0), and the load duration was varied between $0.1 - 20$ times the natural period, T (i.e. the 'time ratio', t_d/T, varied between 0.1 and 20). Biggs presented the results graphically in non-dimensional form in what have become known as 'response charts'. These charts are repeated here in Figures 2.10 and 2.11.

In Figure 2.10, the peak dynamic deflection, z_{max}, is divided by the elastic limit, z_E, and plotted against the time ratio. Each curve represents a different value of $R_u/F_{e,max}$, with lower values of $t_{d,lin}/T$ indicating a shorter load duration, and lower values of $R_u/F_{e,max}$ indicating a higher applied load relative to the resistance of the SDOF system. Any value of displacement above 1.00 in this chart indicates that the system has undergone some plastic deformation. Clearly, longer duration, higher magnitude loads result in the largest levels of plastic deformation.

In Figure 2.11, the time taken to reach peak deflection, t_{max}, is divided by the load duration and plotted against the time ratio.

From knowledge of the equivalent properties of an SDOF system, the peak deflection and time taken to reach peak deflection can easily be determined from these two charts. However, the basis of this method lies in the assumption of linear load-time and linear (or piecewise linear) resistance-deflection relationships which does not accurately represent real life blast load shape and structural resistant relations.

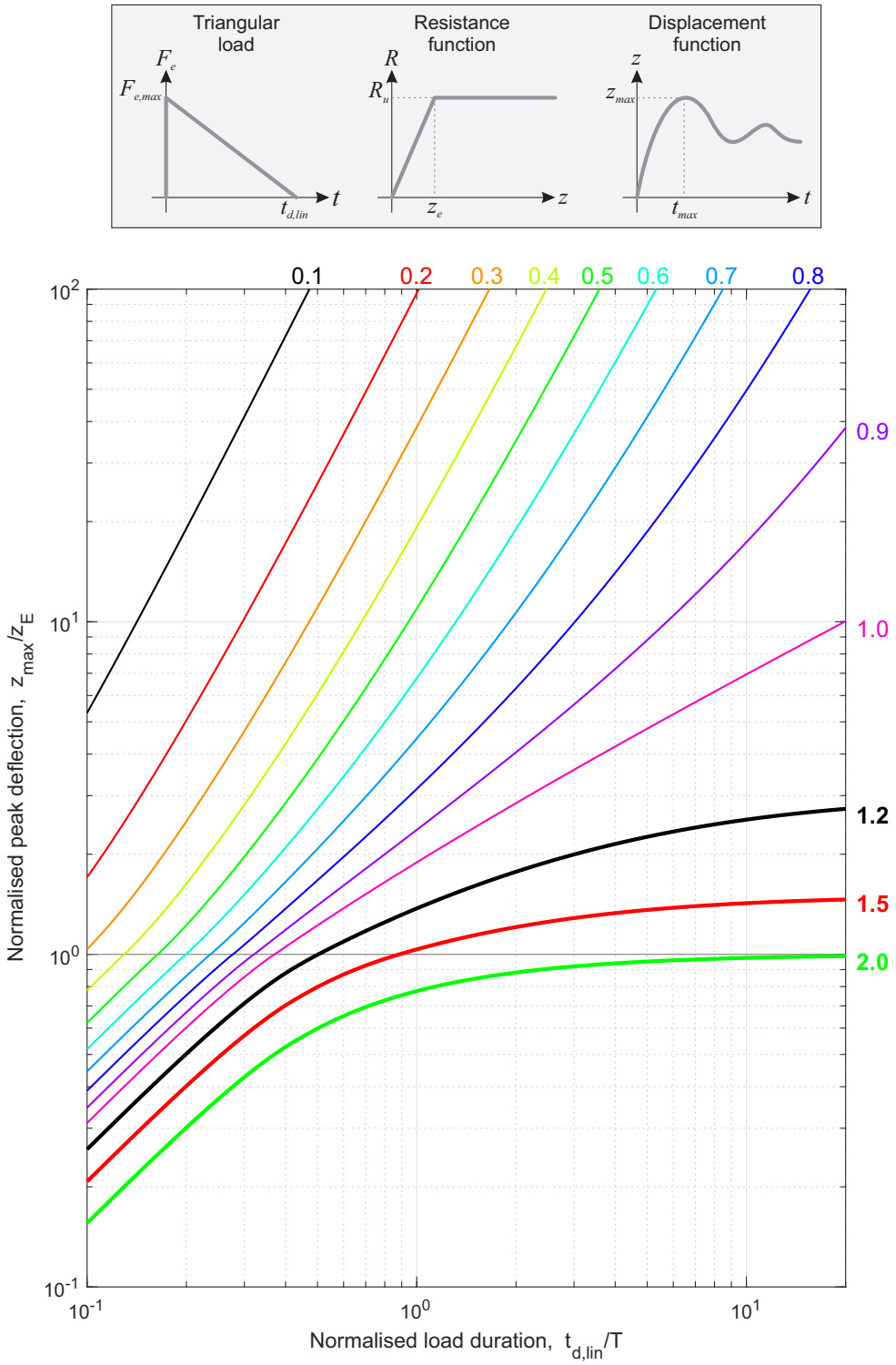

Figure 2.10: SDOF design charts for peak deflection. Numbers next to curves are resistance ratio, $R_u = F_{e,max}$ (Biggs 1964)

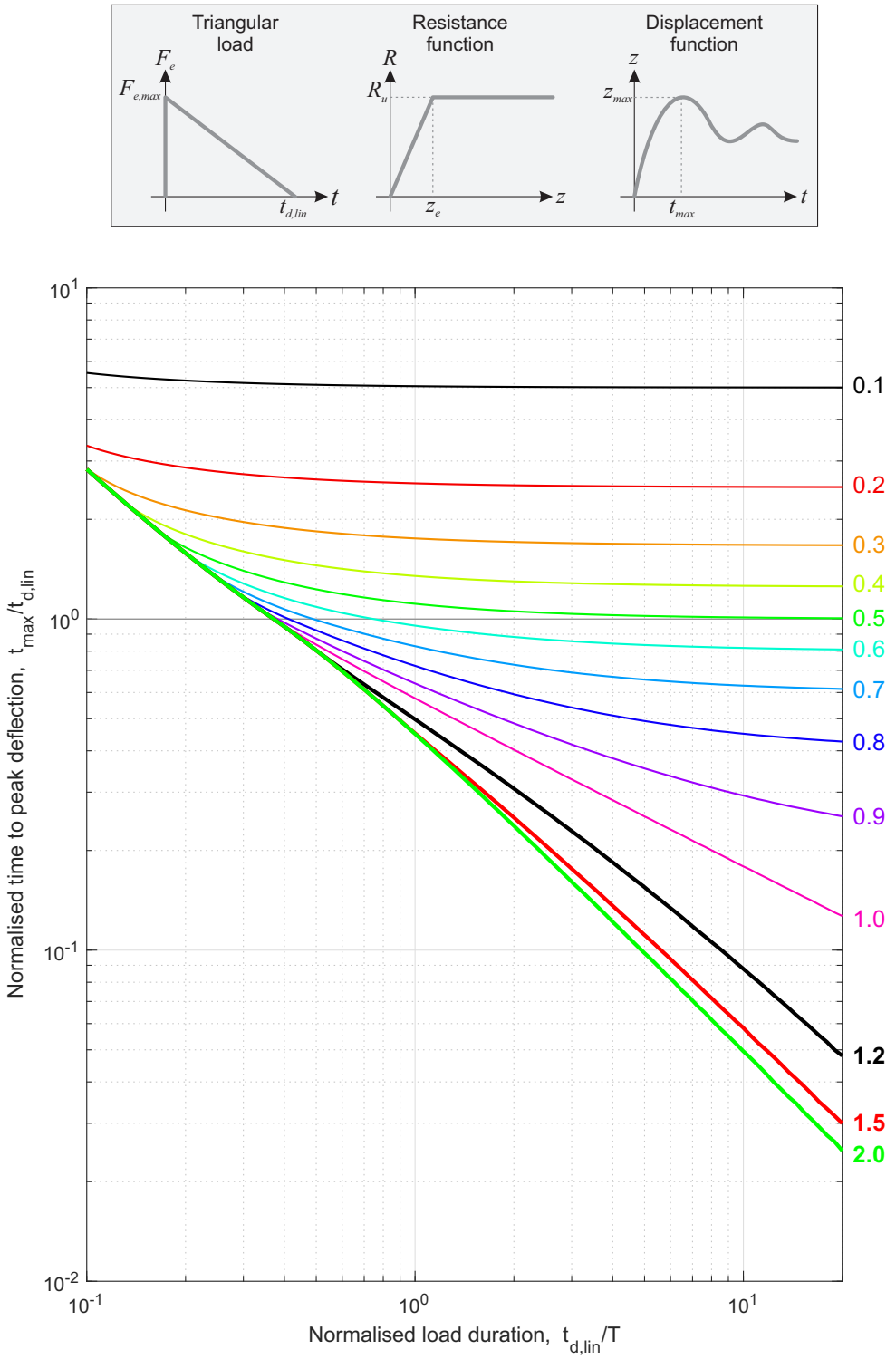

Figure 2.11: SDOF design charts for time to peak deflection. Numbers next to curves are resistance ratio, $R_u = F_{e,max}$ (Biggs 1964)

2.2.5 Pressure-impulse Diagrams

2.2.5.1 Dimensionless P-I Diagram for Elastic Structures

The blast wave from a high explosive damages a structure by causing it to deform, and these deformations may range all the way form the trivial to those corresponding to total destruction (Kinney and Graham 1985). Accordingly, in addition to determining transient dynamic response of SDOF systems as found by the graphic tool introduced in previous sections, it is often pertinent to determine the failure behaviour of structural members and protective systems if suitable and economical blast design required.

By limiting analysis to case of quasi-static loading (one of two limits of response), the load pulse can be idealised as shown in Figure 5.15a while the elastic structure resistance-deflection relationship can be assumed to be linear, as shown in Figure 5.12b.

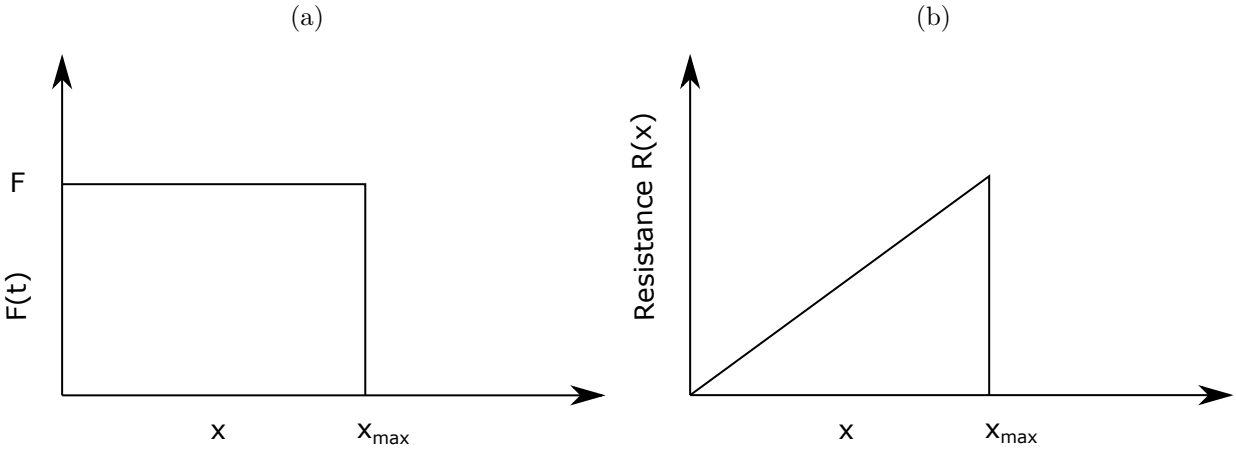

Figure 2.12: Idealised load and resistance-deflection function for quasi-static loading [1]

The maximum work done (WD) occurs when the structure reaches its maximum response:

$$WD = Fx_{max} \tag{2.7}$$

The strain energy generated in the deformed structure, U, is the area beneath the resistance displacement graph given by:

$$U = \frac{1}{2}kx_{max}^2 \tag{2.8}$$

Equating WD and U after some rearrangements results in:

$$\frac{x_{max}}{F/k} = \frac{x_{max}}{x_{st}} = 2 \tag{2.9}$$

where x_{st} is the static displacement that would result if the force F were applied as a static load.

The ratio of the deflection under the applied dynamic load to the deflection which would be produced by a static load of the same magnitude leads to the concept of Dynamic Load Factor (DLF):

$$DLF = \frac{x_t}{F/k} \tag{2.10}$$

Here, Eq.(2.8) gives the upper bound of response and is called the quasi-static asymptote

In case of another limit of response, impulsive loading, the pulse duration tends to zero and an idealised impulsive load is delivered to a structure. This produces an instantaneous velocity change: momentum is acquired and the structure gains kinetic energy which is converted to strain energy. The impulse causes an initially stationary structure to acquire a velocity $\dot{x}_0 (= I/M)$. From this the kinetic energy delivered, KE, is given by:

$$KE = \frac{1}{2} M \dot{x}_0^2 = \frac{I}{2M} \tag{2.11}$$

where $\dot{x}_0$ is the initial velocity.

The structure will acquire the same strain energy U as before because it displaces by $xmax$. Thus if KE and U are equated, after some rearrangement we obtain:

$$\frac{x_{max}}{F/k} = \frac{x_{max}}{x_{st}} = \frac{1}{2}\omega t_d \tag{2.12}$$

which is the equation of the impulsive asymptote of response.

Since there are 2π radians in one angular revolution, the time period of each oscillation, T is given by:

$$T = \frac{2\pi}{\omega} \tag{2.13}$$

If these two asymptotes are drawn on a response curve of t_d/T against $\frac{x_{max}}{F/k}$, the actual response of the structure can then be sketched without recourse to further analysis as

shown in Figure 2.13. The three loading regimes of quasi-static, impulsive and dynamic response are identified on the resulting graph as regions I, II and III, respectively.

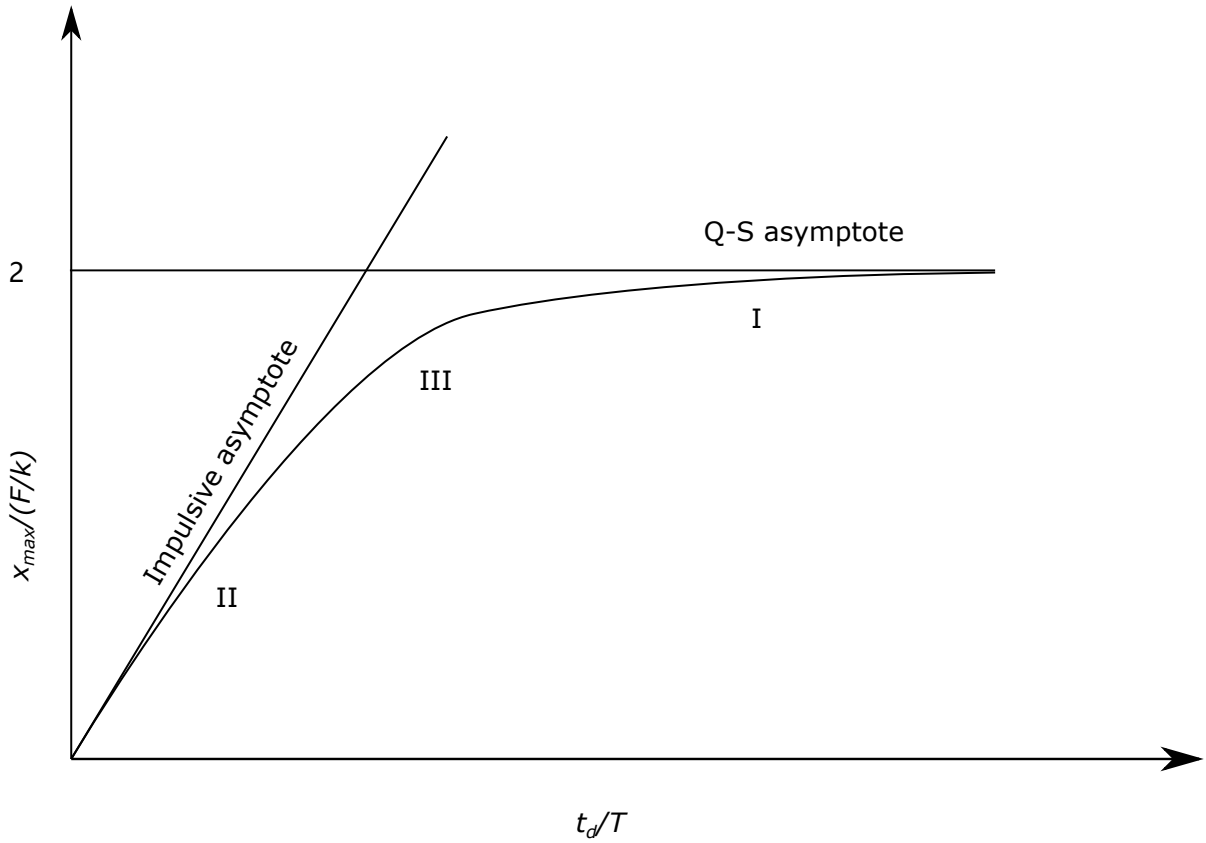

Figure 2.13: Loading realms I, II, and III correspond to the quasi-static asymptote, impulsive asymptote, and static asymptote, respectively

By rearranging the terms which define the x and y axis of Figure 2.13, a failure envelope can be generated on dimensionless axes which relate force F to a total impulse I – we call this failure envelop 'Pressure-Impulse diagram' (hereafter abbreviated as 'P-I diagrams'), as shown in Figure 2.14. With a maximum displacement or damage level defined, the 'P-I diagrams' allows the engineer to quickly determine whether a particular combination of load and impulse will result in failure or a specific damage level of the structure. Combinations of pressure and impulse that fall to the left of and below the curve will not induce failure while those to the right and above the graph will produce damage in excess of the allowable limit.

Based on the max-deflection criterion, Li and Meng (2002) derived the P-I diagram of an elastic-brittle thin plate by employing the linear SDOF method and dimensional analysis. Fallah et al. (2013) developed pulse-shape-independent P-I diagrams for elastic and

elastic-plastic responses of continuous beams. Based on the maximum principal stress criterion, Chen et al. (2017, 2019) built an equivalent linear SDOF system to determine the pressure and the impulse asymptotes of the framed monolithic glass and laminated glass. A theoretical method based on the energy balance approach was developed for determining the iso-damage curves of framed monolithic glass for different damage levels. Zhang et al. (2013) presented empirical formulae based on numerical results to predict the impulse and pressure asymptote of P–I diagrams for PVB laminated float glass panel. The failure of interlayer laminate is used to define the total failure of glazing windows. By constructing the P-I diagram based on empirical formulas and comparing it with those derived from SDOF models, Zhang et al. (2013) arrived at the conclusion that the proposed empirical formulas offer a reliable means of predicting the blast response of PVB laminated panels.

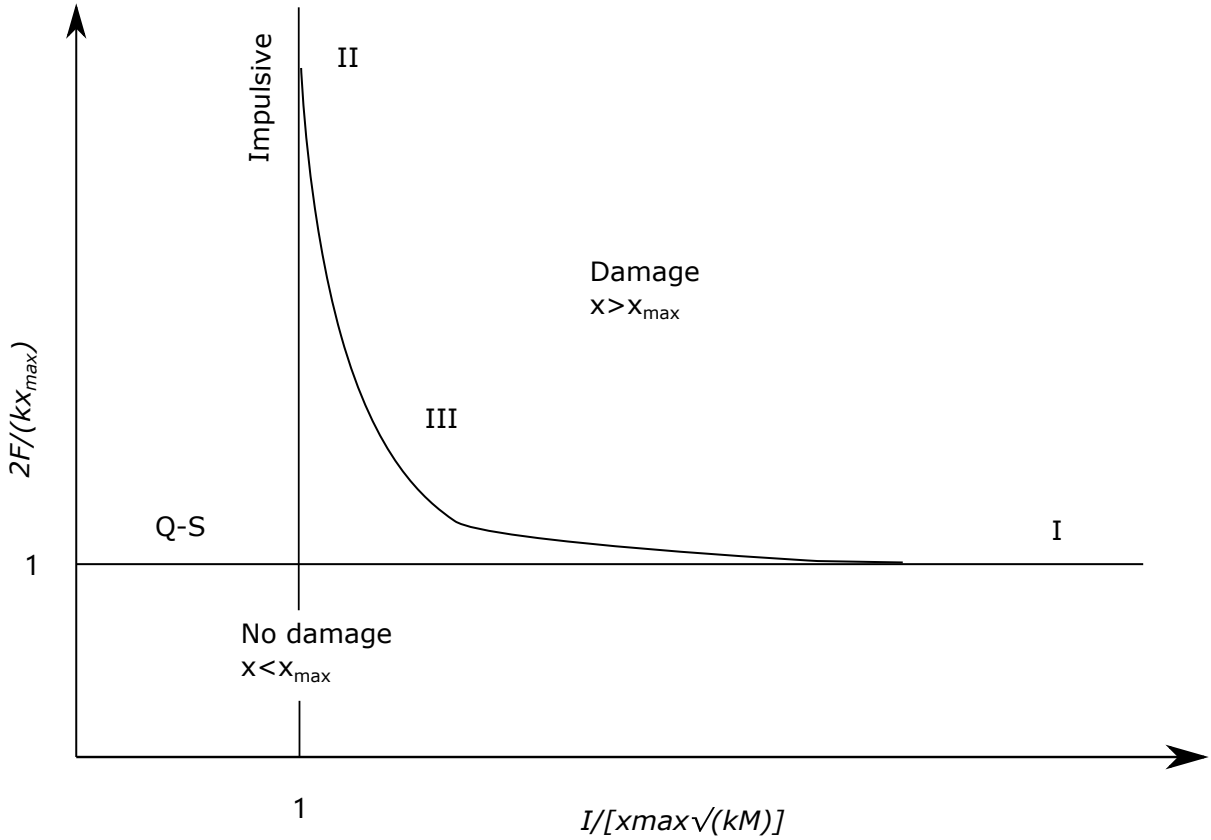

Figure 2.14: Non-dimensionalised pressure—impulse diagram for SDOF elastic system

2.2.5.2 Iso-damage Curves

Once levels of damage are defined, these 'P-I diagrams' can be useful in compiling data from numerical, analytical or experimental studies of structural components. Especially useful for the designer is the use of iso-damage curves on P-I diagrams, where contours of equal damage to components are plotted on the P-I diagram along with curves of the pressures and impulses generated by particular combinations of charge size and stand-off.

For example, Jarrett (1968) compiled a database of damage to typical homes and factory buildings from various sources including records of bombs dropped on the UK during the Second World War, as shown in Table 2.1. It was found that the distance at which various classes of damage were sustained by the "average British dwelling house" could be approximated by the following relation:

$$R = \frac{K_0 W^{1/3}}{\left[1 + (\frac{3175}{W})^2\right]^{1/6}} \tag{2.14}$$

where R is the threshold safe stand-off in metres, W is the charge mass in kg TNT, and K_0 is an empirical constant which differs depending on the specified damage level. The damage was divided into the following classes:

Class	**Damage constant,** K_0	**Description**
A	3.77	almost complete demolition
B	5.55	$50-75\%$ external brickwork destroyed or rendered unsafe and requiring demolition
C_b	9.52	houses uninhabitable: partial or total collapse of roof, partial demolition of one to two external walls, severe damage to load-bearing partitions requiring replacement
C_a	27.8	not exceeding minor structural damage: partitions and joinery wrenched from fixings
D	55.5	remaining inhabitable after repair: some damage to ceilings and tiling, more than 10% window glass broken

Table 2.1: Damage classes for brick-built houses (Jarrett 1968)

Hetherington and Smith (1994) presented Jarrett's equation in P-I space, with peak incident pressure, p_{so}, and peak incident specific impulse, i_{so}, on the horizontal and vertical axes respectively (see Figure 2.15). These iso-damage curves are currently used in the evaluation of safe stand-off distances for explosive storage in the UK, and can also be used with reasonable confidence to predict the damage to other structures such as small office buildings and light-framed factories (Cormie et al. 2009).

The 'iso-damage diagrams' is a useful tool where a full detailed blast design is impractical or prohibitively expensive. However, the basic assumption of idealised loading, simple statistical definitions of damage to components under giving loading limits the application of the iso-damage diagrams.

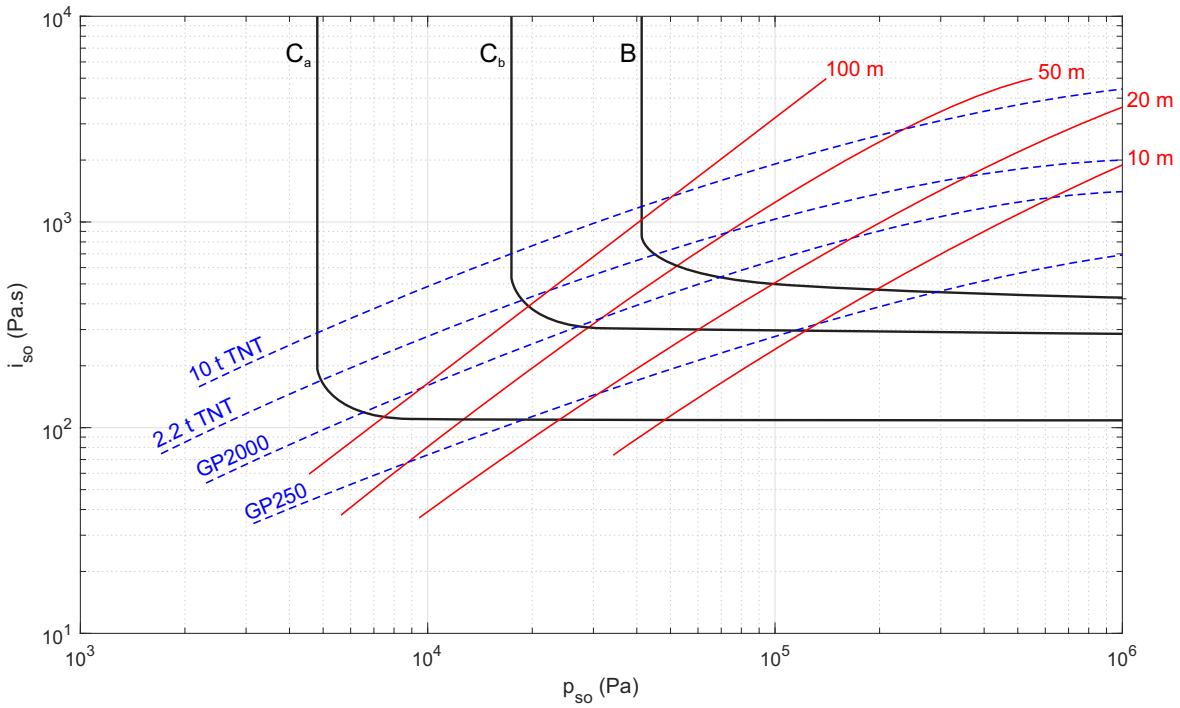

Figure 2.15: Iso-damage curves (classes B–C_a) for brick-built houses, with stand-off and charge mass overlaid (Hetherington and Smith 1994)

2.3 Plate Response to Blast Loading

2.3.1 Overview

A plate is a flat solid body whose thickness is very small compared to its planar dimensions and can be classified into four types :

- Thick plates
  - The analysis of stress within the plate is considered as a three-dimensional elasticity problem. The stress analysis, consequently, becomes more involved and the solution to this problem needs the use of equilibrium, continuum and a material constitutive relationship (Timoshenko and Woinowsky-Krieger 1959).
- Medium-thick plates
  - The lateral load is supported entirely by bending stresses. Also, the deflection of the plate, w are small compared with its thickness, h, (typically, $\frac{w}{h} < \frac{1}{3}$) (ASM 2014).
- Thin plates
  - The thin plate supports the applied load by both bending and direct tension accompanying the stretching of the middle plane.The deflections of the plate are not small compared to the thickness ($\frac{1}{3} < \frac{w}{h} < 10$) (ASM 2014).
- Membranes
  - For membranes, the resistance to lateral load depends exclusively on the stretching of the middle plate and, hence, bending action is not present. Very large deflections would occur in a membrane ($\frac{w}{h} > 10$)

Many common structural forms are composed of individual plated elements, including wing panels and rocket fins, building floors and walls, automotive body panels and disk wheels and other, and thus the investigation of blast loading effects on plates is a prerequisite to understanding the integral behaviour and only then provide robust and effective protective structures to withstand extreme loading.

Broadly speaking the plate theory is concerned mainly with the response of plates under lateral loading whereas plates subjected only to in-plane loading can be solved using two-dimensional 'plane stress theory' (Kelly 2013) [viii]

Consider a typical element of the plate with nine components of the stress tensor acting on it shown in Figure 2.16. Normal stresses and strains are denoted by σ_{ii} and ε_{ii}, respectively, while shear stresses and strains are denoted by τ_{ij} and γ_{ij}, with $i, j = x, y, z$.

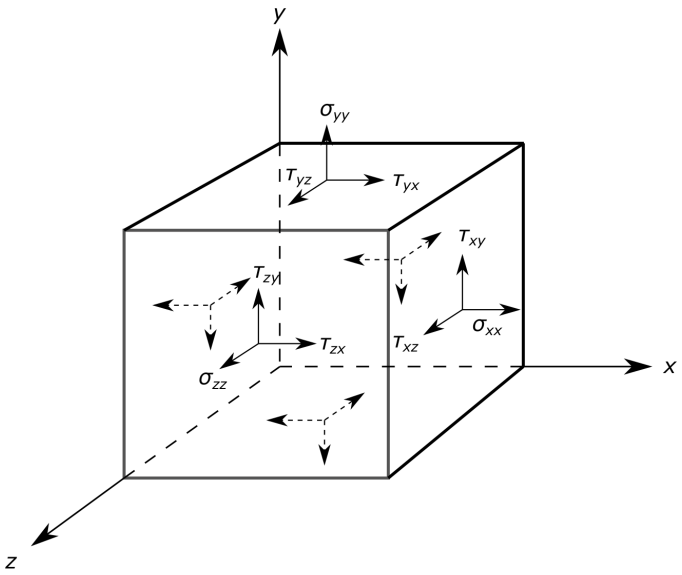

Figure 2.16: Stress acting on a material component

[viii] However, it doesn't work for the case when the in-plane loads are compressive and sufficiently large

For the sake of convenience, the normal stresses and strains are denoted using single subscripts, i.e. σ_i and ε_i instead of σ_{ii} and ε_{ii}. By using the concepts of equilibrium, continuum and a material constitutive relationship, one can obtain following equations:

- Equilibrium equations

$$\begin{aligned} \sigma_{x,x} + \tau_{xy,y} + \tau_{xz,z} &= 0 \\ \tau_{xy,x} + \sigma_{y,y} + \tau_{yz,z} &= 0 \\ \tau_{xz,x} + \tau_{yz,y} + \sigma_{z,z} &= 0 \end{aligned} \tag{2.15}$$

- Strain-displacement relations

$$\begin{aligned} \varepsilon_x &= u_{,x} \quad \gamma_{yz} = v_{,z} + w_{,y} \\ \varepsilon_y &= v_{,y} \quad \gamma_{xz} = u_{,z} + w_{,x} \\ \varepsilon_z &= w_{,z} \quad \gamma_{xy} = u_{,y} + v_{,x} \end{aligned} \tag{2.16}$$

- Stress-strain law

$$\sigma_i = 2G\varepsilon_i + \lambda e \quad \tau_{ij} = G\lambda_{ij} \text{with } i, j = x, y, z \tag{2.17}$$

where u, v, w are the displacements along the x, y, z coordinates, respectively. G and λ are Lamè's constants, e is the volumetric strain given by $\varepsilon_x + \varepsilon_y + \varepsilon_z$, and a subscript comma is used to denote differentiation. In terms of the Young's modulus E and Poisson's ratio μ, Lamè's constants are given by

$$\lambda = \frac{\mu E}{(1+\mu)(1-2\mu)} \quad G = \frac{E}{2(1+\mu)} \tag{2.18}$$

Various aspects of the theory and analysis of plates are found in the articles and books by Timoshenko and Woinowsky-Krieger (1959), Ugural (1999), V. and Krauthammer (2001), Birman (2010), Bhaskar and Varadan (2014). Of these theories, there are two plate theories has the most mass appeal and have been widely used in many fields of engineering; classical plate theory (also known as the Kirchhoff theory of plates) and first-order shear plate theory (also known as Mindlin theory of plates).

2.3.2 Plate Theory

Though, in reality, a plate is a three-dimensional body, it is not essential to use the rigorous approach of the theory of elasticity if the thickness is relatively small. A natural inference from the results of the three-dimensional elastic analysis leads to the classical plate theory. However, this approximation to the three-dimensional problem can be considered acceptable only if it leads to a reasonably good estimate of the strain energy of deformation of the structure, and the contributions of the different stress and strain components to this energy provide a correct estimate of their relative importance.

Bhaskar and Varadan (2014) compared the contribution of bending, transverse shear and thickness stretch/contraction to the strain energy of a simply supported rectangular strip under sinusoidally distributed transverse load. It has been shown that the bending strain energy is predominant for a thin plate while the other two energies tend to be negligibly small. On this basis, the neglect of the transverse shear strain γ_{xz}, γ_{yz}, the transverse normal strain ε_z and the transverse normal stress γ_z, has been identified as the main hypothesis for the development of the classical plate theory.

Classical plate theory has been widely used for the study on the vibrations of plates with various shapes, supports, loading conditions, and complicating effects, as reported in the literature (Micallef et al. 2016; Mindlin 1951; Bhaskar and Varadan 2014; Cormie et al. 2009; Colton 1976; Bimha 1996; Rezasefat et al. 2019; Mehreganian et al. 2018). The final deformation predicted by the Mehreganian et al. (2018) theoretical solution based on the classical plate theory (also known as Kirchhoff-Love theory) has shown that it gives better estimates for dynamic performance as rigid-plastic thin plates than previous rigid-plastic models proposed by Jones (1997) when subjected to close-in low-impulse blast loading.

However, as noted by Leissa (1969); Itao and Crandall (1979), comparison between the values for the first 701 modes of vibration of circular plates and the numerical results obtained by the classical plate theory have shown that classical plate theory overestimates the higher modes' vibration and buckling load and underestimation of bending deflection. This loss of accuracy mainly results from the neglect of transverse shear deformation and rotary inertia in thick plate analysis. To allow for these two effects, Reissner (1945) and Mindlin (1951) proposed the first order shear deformation theory for the motion of thick plates which introduced a shear correction factor κ to compensate the errors resulting from the assumption of uniform shear strain distribution in the thickness direction.

Irie et al. (1980) tabulated the natural frequencies of vibration based upon the Mindlin plate theory for uniform circular plates with free, simply supported, and clamped edges for the first several tens modes. Xing and Liu (2009b,a) developed closed form solutions for free vibrations of rectangular Mindlin plates which can be employed to predict frequencies for any combinations of simply supported and clamped edge conditions.

Consideration of the effect of only bending and membrane or membrane alone, as validated in previous studies, provides a good estimation of the rigid plastic behaviour of the plate under blast load. However, the effect of transverse shear and rotatory inertia cannot be ignored in certain cases, e.g. where the plate was thick enough to ignore the membrane resistance.

Micallef et al. (2014) presented an analytical solution for predicting the transverse displacement of a simply supported circular steel plate due to a generalized form of blast loading. The 'Mindlin plate theory' was incorporated in their studies with the assumption of a sufficiently thick plate such that the overall response is governed by the interaction of bending and transverse shear. The effect of transverse shear on the dynamic performance of the steel plate were investigated. It was pointed out that the influence of transverse shear is only relevant for small values of ν-plate radius-to-thickness ratio and displacements at both midpoint and supports are only noticeably significant for $\nu \leq 5$. Similar conclusions were obtained from their investigation on the thick square plate (Mehreganian et al. 2019b).

2.3.3 Deflection of Plates under Blast Loading

Investigations into the response of plates subjected to blast loading have been carried out for many years. In 1989, Nurick and Martin (1989a,b) presented an overview of previous theoretical and experimental work on the deformation of thin plates under blast loads and introduced a dimensionless parameter for blast loaded plates which has been further employed by many other researchers (Neto et al. 2018; Xu et al. 2019; Jacob et al. 2007; Langdon et al. 2015). The dimensionless number they proposed could work for predicting the deflection of blast-loaded circular plates under both uniform and localized loading as well as quadrangular plates under uniform blast loading.

Jacob et al. (2004) performed an experimental investigation to study the effect of scaling of plate geometries and loading conditions on the deformation of localized blast-loaded

quadrangular plates. They presented a modified dimensionless number for the prediction of quadrangular plate response when subjected to localized blast loading. Later, Jacob et al. (2007) conducted a series of tests to investigate the effect of stand-off distance on the failure of fully clamped circular mild steel plates under blast loads. A new loading parameter was then introduced to incorporate the influence of stand-off into the Nurick's damage number. Also, an analytical solution including strain-rate sensitivity of steel was proposed for predicting the mid-point deflection.

Most of the above experimental and analytical efforts were mainly concerned with the structural response under small magnitude of blast loading whose behaviour were governed by bending or shear resistance without any fracture occurring. Dynamic response of thin plates under intense loading is quite different from that of small deflection problem as it is dominated by the membrane stretching [ix] resistance where bending resistance could be ignored. Hence, internal energy was dissipated mainly through by the action of membrane with negligible flexural work.

Several approximate techniques were proposed in the theoretical formulation of large deflection problem of membrane under blast loading.

Symonds and Wierzbicki (2019) developed a simplified mode approximate method with only membrane action considered to predict the response of clamped circular plates to uniform impulsive loading. Results were compared with experimental data of Bodner and Symonds (1979). It was observed that the suggested membrane mode solution could predict the large deflection of impulsively loaded plate with great confidence.

An approximate closed-form solution for large deformation prediction of clamped plates under localised blast load was developed by by Wierzbičk and J. (1983), where the analytical solution was constructed by combining wave form solution and mode solution for early and late motion, respectively. The plate was assumed to be a rigid-plastic membrane in their theoretical development and it was pointed out that precise determination of deflected shape is necessary for the prediction of the onset of tensile necking and failure of plates. Recent experimental measurements from Rigby et al. (2019b), has shown that the initial deflected shape was dependent on the impulse distribution. Fuller (2018) reported that the failure onset area was believed at the location of maximum slope on the kinetic energy distribution across the target, which would help to advance the work done by Wierzbičk and J. (1983) for failure onset prediction.

[ix] Membrane stretching refers to the deformation of a thin, flexible membrane when it is subjected to external forces or pressure that cause it to elongate or expand

Babaei and Darvizeh (2012) simplified the wave solution by using a zero-order Bessel function of the first kind to describe the deflection profile of a circular plate subjected to localized impulsive loading. An analytical model was proposed which accounts for the energy dissipation through plastic work by equating the strain energy stored in plastically deformed membrane to the initial kinetic energy imparted to the target plate.

Among the above analytical solutions, only transverse deflection was considered and all authors assumed a fixed mode shape for the deformation of plates subjected to impulsive loading. However, experimental work from Rigby et al. (2019b) has shown that transient displacement profile of a blast loaded plate is dependent on the spatial variations in loading. Hence, it is necessary to take the influence of loading distribution into consideration for predicting the deflection of blast loaded plates and prediction only based on a fixed mode shape would result in inaccurate results.

Lomazzi et al. (2021) made a detailed comparison of performance of the main analytical methods for assessing the structural response of quadrangular metal plates due to blast loads. The estimated values from the Jones' method (Jones 1971) and the Nurick and Martin's methods (Xu et al. 2019) were compared with those obtained from numerical models, i.e., Eulerian-Lagrangian and Analytical-Lagrangian, and from experimental observations. Based on the results, it was noted that, for the case when free-field explosion was considered, greater permanent deflections were observed from the prediction of both Jones' method and the Nurick and Martin's theory than the estimates from the numerical models

Curry and Langdon (2017) performed several experiments at the Blast Impact and Survivability Research Unit (BISRU) on the fully clamped square steel plates due to close-in explosion loading to investigate the deformation and strain evolution of the plate and the influence of stand-off distance on the transient response and permanent deformation of think steel plates subjected to air-blast loading. The blast load was produced by the detonation of PE4 explosive placed at different stand-off distances. High speed imaging and digital image correlation (DIC) techniques were used to measure the transient deformation profiles of the plates. It was pointed out that the measured transient profile was not consistent with the final deformation profile and the difference in the midpoint deformation of these two profiles decrease with an increase in charge mass and an increase in global deformation. Also, the permanent deformation was found to increase linearly with increasing impulse and decreased with increasing stand-off distance. Later on, Curry and Langdon (2021) performed another experimental investigation on assessing the influence of explosive charge backing on the deformation of fully clamped

steel plates. The '3D-DIC' technique [x] was applied for capturing the dynamic response of specimens. Based on experimental results, the charge backing was recognized as an effective factor on the impulse transfer. Also, results demonstrated that in comparison to air-backed condition, the transient deflection was slightly larger but not to the same degree as the impulse increases.

Shuaib et al. (2016) numerically studied the response of carbon fibre reinforced polymer (CFRP) retrofitted steel plates under uniform blast load by using finite element software, LS-DYNA (Corporation 2021; LSTC 2021). Simulation results showed a satisfactory correlation with the experiments for the damage features that occurred in CFRP retrofitted steel plates.

2.4 Failure of Plates under Blast Loadings

2.4.1 Overview

When a high explosive detonates at some distance from the structure, the generated hot gas with extremely high magnitude pressure and temperature expand rapidly and force the surrounding air out of the volume it occupies (Cormie et al. 2009). As a consequence, the transient air pressure wave namely blast wave is produced. The magnitude of the pressure at the blast wavefront decreases as the shock wave travel further from the explosion source. The imparted blast loading becomes more 'uniform' as the distance between the explosion source and the structure increases so that more 'global' deformation and failure modes occur (far-field events). Conversely, more 'local' structural responses are observed if the applied loading is highly spatially non-uniform over the face of the target in scenarios where close-in detonation occur (near-field events). Hence, intimate knowledge of how the structure will deform and fail when subjected to blast loading as well as the how the potential failure modes vary as the applied blast loading changes are vital in designing the protective systems.

[x] 3D-DIC stands for three-dimensional digital image correlation. It is a non-destructive experimental technique used to measure the full-field 3D deformation of a surface or structure under load

2.4.2 Failure Modes

A large explosion may inflict widespread damage and represent major disaster. To minimize such effects some knowledge of the mechanisms of explosion damage becomes essential. Only then it is possible to provide the best available planning, designing and construction for needed disaster resistant facilities.

One objective of this thesis is to investigate the initiation and progression of failure of the plate structure under an impulsive loading and to this end a thorough understanding of the failure mechanism of structure subjected to blast loading is crucial.

2.4.2.1 Influence of Loading Intensity on Failure modes

The failure modes of structural steel subjected to localised blast loading have been extensively studied. Nurick and Radford (1997) examined the rupture of mild steel plates under localized blast loading and identified several distinct failure modes with increasing intensity of blast loading. A central bulge superimposed onto a larger global dome caused by large inelastic deformation is defined as the first failure mode (Mode I). With increased intensity of blast loading, large inelastic deformation with thinning and strain localisation due to tensile instability was identified at the inflection point of the central bulge (Mode Itc). At higher impulses, partial (Mode II*c) and complete tearing (Mode IIc) in the central portion was observed leading to the ejection of a circular fragment. Further increases in the blast loading result in the propagation of a radial crack outward from the initial hole producing several petals which curl back as the cracks continue to propagate (Petalling failure). Figure 2.17 shows three typical failure modes of thin clamped circular plates subjected tot localized explosive loading.

Early experimental work of Nurick and Shave (1996), Teeling-Smith and Nurick (1991b) and Mendes and Opat (1973) on the failure modes of structures (beams and plates) under uniformly distributed impulsive loadings, classified three different modes as large inelastic deformation (Mode I), partial tearing (Mode II) or complete tearing and shear failure (Mode III). Following that, a series of experiments were carried out by Nurick and his co-workers (Nurick and Shave 1996; Nurick and Radford 1997; Nurick et al. 1996; Yuen and Nurick 2000) on the failure modes of plates with different shapes, namely square and circular, under various intensity of loading applied uniformly or localized, further subdividing the mode II into three phases: mode II* – partial tearing; mode IIa –

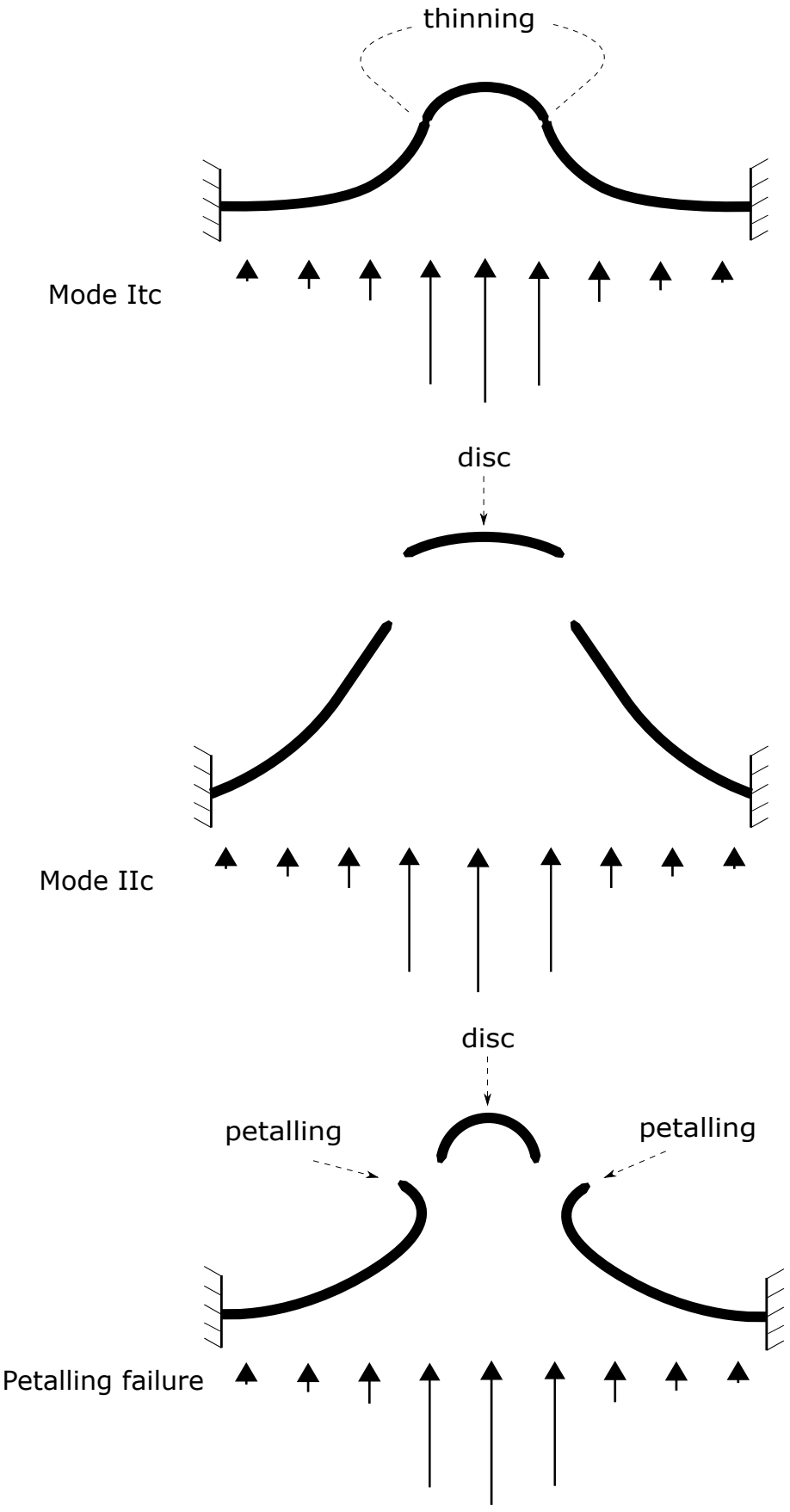

Figure 2.17: Failure modes with increasing intensity of applied loading

complete tearing with increasing mid-point deformation; mode IIb – complete tearing with decreasing mid-point deformation. A summary of the modes of failure, contrasting locally and uniformly loaded metal plates, is listed in Table 2.2 (Jacob et al. 2007).

Modes of failure	Description	Uniform loading	Localized loading
Mode I	Large inelastic deformation	✓	✓
Mode Ia	Large inelastic deformation with necking around part of the boundary	✓	
Mode Ib	Large inelastic deformation with necking around the entire boundary	✓	✓
Mode Itc	Large inelastic deformation with thinning in the central area		✓
Mode II*	Large inelastic deformation with partial tearing around part of the boundary	✓	
Mode II*c	Partial tearing in the central area		✓
Mode II	Tensile tearing at the boundary	✓	✓
Mode IIa	Tearing with increasing midpoint deflection with increasing impulse with complete tearing at the boundary	✓	
Mode IIb	Tearing with decreasing midpoint deflection with increasing impulse with complete tearing at the boundary	✓	
Mode IIc	Complete tearing in the central area – capping		✓
Mode III	Transverse shear failure at the boundary	✓	
Petalling	Tearing at centre with 'petals' of material folded away from blast location		✓

Table 2.2: Summary of modes of failure defined for plates subjected to uniform and localized blast loads

2.4.2.2 Shear Fracture Mode

While the tensile failure mode has been observed in many other studies (Teeling-Smith and Nurick 1991b; Saeed Ahmad et al. 2018), other research suggests that it may not be applicable to all steels or loading conditions.

Langdon et al. (2015) experimentally examined the response of five different materials subjected to localized air-blast loading and identified a monotonically increasing relationship between specific energy to tensile fracture (SETF) of the materials and non-dimensional rupture impulse. Later on, the SETF was also found to be a good indicator for predicting the deflection of five plates when subjected to blast loading according to Xu et al. (2019). They used SETF to calculate the non-dimensional impulse developed by Nurick and Martin (1989b) instead of the quasi-static yield stress and the predicted deflection based on non-dimensional impulse with SETF fit the experimental data well. Nevertheless, experimental work of McDonald et al. (2017) has shown that blast rupture threshold of the amour grade steels were poorly captured by the correlation identified by Langdon et al. (2015). Following that, McDonald et al. (2018) conducted a detailed fractographic investigations into the rupture failure mode of 4 high strength steels subject to localised blast loading and further confirmed that high strength steel initiated rupture via a ductile shear fracture mode which is different from tensile tearing commonly observed in lower-strength steels e.g. mild steel.

Although the detailed classification of failure modes of metal plates when subjected to uniformly or localized blast loading has been given, there still remains an research question that is the quantification of the influence of distribution and intensity of the blast loading on the failure behaviour. Hence, the research will focus on studying the failure performance of brittle plates under arbitrary impulsive loadings. The load concerned will be assumed to be in a generalised form which can model both localized and uniform blast loading, making the presented model a highly adaptable solution which is adequate for a variety of loading scenarios.

2.4.3 Influence of Loading on Failure Response

Intense loading arising from malicious or accidental explosions can cause significant damage to structures and structural elements, prediction of the likely amount of damage caused by such loadings have been a challenging research topic. One vein through which this goal is achievable is the accurate quantification of the effects of the imparted explosion loading on structures, i.e. the resulting deformation and failure behaviour. While deformation and failure modes of structures involved in such extreme loading scenarios could differ significantly according to various factors, e.g. charge size (Jacob et al. 2004), stand-off (Jacob et al. 2007) and material type (Nurick and Martin 1989a,b; Xu et al. 2019; Langdon et al. 2015) and much efforts have been made to investigate the effect of these factors on the explosion-resistant behaviour of the structure. However, distribution and magnitude of the imparted loading even the two of most important factors in a structural analysis (Jacob et al. 2004, 2007; Yuen et al. 2017), whose influence on the failure response of the target structure have not yet clearly understood.

There has been a considerable body of literature existing on the structural response of single and double steel (Jacob et al. 2007; Saeed Ahmad et al. 2018; McDonald et al. 2017, 2018; Mohammadzadeh and Noh 2019), aluminium (Xu et al. 2019; Aune et al. 2015) and composite plates (Langdon et al. 2014) with a variety shapes, namely square (Li et al. 2020; Nurick and Shave 1996), rectangular (Mohammadzadeh and Noh 2019), circular (Symonds and Wierzbicki 2019; Bodner and Symonds 1979; Nurick and Radford 1997; Teeling-Smith and Nurick 1991b) and V-Shape (Yuen et al. 2012) under various boundary conditions (Nurick et al. 1996; Moriello et al. 2020) subjected to uniformly (Teeling-Smith and Nurick 1991b; Moriello et al. 2020), or localized blast loading (Jacob et al. 2004; Wierzbičk and J. 1983; Nurick and Radford 1997; Saeed Ahmad et al. 2018), investigated numerically, experimentally (Rigby et al. 2019b; Fuller 2018) and theoretically (Babaei and Darvizeh 2012; Mohammadzadeh and Noh 2019).

Many of aforementioned studies, however, have focused on the transient or permanent deflection prediction of plates in the absence of failure, and far too little attention has been paid to the failure response due to blast loadings.

Wang et al. (2022) presented an equivalent method for assessing the state of a brittle-elastic panel under arbitrary pulse loading and the average splash speed of glass fragments after failure. The method was obtained based on Youngdahl Equivalent Method (Y-EM)

and saturation analysis to determine the equivalent valid pulse of an arbitrary pulse by a 3D-Pressure-Duration diagram.

Nagesh and Gupta (2022) developed numerical models to estimate the large deformations and failure of clamped circular steel plates under uniform impulsive loads. The models were obtained based on the hybrid damage model which incorporates the 'Maximum Shear Stress (MSS)' failure criteria and 'Fracture Forming Limit Diagram (FFLD)' failure criteria. The effectiveness of the hybrid damage model was validated by comparing the predicted response and failure modes of plates under different intensity of uniform impulsive loads with observed experiments. It was found that the model provided satisfactory predictions for the response of clamped plates subjected to a broad range of uniform blast loads in the 'Mode I failure zones', 'Mode II failure zones' and 'Mode III failure zones'.

Micallef et al. (2012, 2014) presented a series of studies predicting the response of simply supported steel plates under blast loadings. In the first attempt, the dynamic performance of thick plates were investigated with only bending effects considered. The localized loading was assumed to be in a general form of function with a spatial variation having a central radial zone with constant pressure and exponentially decaying profile outside the zone. This assumption makes it adaptable to model the loading induced from both distal and proximal explosions. Permanent transverse displacements of plates predicted by the analytical formulation under various pulse shapes, e.g. rectangular, linear and exponentially decaying, are compared with those obtained from ABAQUS. In the second study, an analytical solution for predicting the transverse displacement of a simply supported circular steel plate due to a generalized form of blast loading was developed. The 'Mindlin plate theory' was incorporated in their studies with the assumption of a sufficiently thick plate such that the overall response is governed by the interaction of bending and transverse shear. The effect of transverse shear on the dynamic performance of the steel plate were investigated. It was pointed out that the influence of transverse shear is only relevant for small values of ν-plate radius-to-thickness ratio and displacements at both midpoint and supports are only noticeably significant for $\nu \leq 5$. Similar conclusions were obtained from their colleagues' investigation on the effect of transverse shear on the plastic dynamic response of thick square plate (Mehreganian et al. 2019b). In addition to investigating the effect of transverse shear on central and endpoint displacement, the influence of loading parameters and plate thickness on the permanent deformation was conducted by implementing a parametric study.

2.4.4 Predictive Methods

Existing prediction methods have been demonstrated to accurately predict the failure behaviour of the plate under blast loadings. Rezasefat et al. (2019) developed a numerical model for predicting the dynamic plastic response of double-layered circular metallic plates under localized impulsive loading and validated numerical results against the available experimental results. They performed a parametric study on fully clamped circular double-layered metallic plates under the impulse range of $10 - 110 N.s$ and proposed an empirical formulas for predicting the maximum mid-span deflection of back and front layers based on the dimensionless analysis. However, other than central location of the plate, failure could also initiate at other location, e.g. failure initiates at the boundary for the case when a plate under uniform blast loading. The loading model they used idealizes the blast loading as a constant pressure value acting over a charge diameter and an exponentially decaying pressure distribution on the remainder of the structure in the radial direction. Similar spatial distribution was employed by Mehreganian et al. (2018) who proposed a theoretical model to estimate the dynamic response of simply supported rigid-plastic square plates under localized blast loading. However, their solution could only work for thin plates which neglects the effect of transverse shear and rotary inertia.

Lee and Wierzbicki (2005b,c) numerically and analytically studied the transient response of fully clamped thin plates subjected to a localized pulse loading. They developed a ductile fracture criterion to predict the initiation site and extent of fracture based on the accumulated equivalent plastic strain with the stress triaxiality as a weighting function. They concluded that, both crack length and final deformed shape are strongly influenced by the spatial distribution and intensity of impulsive loading. However, the loading model they used is an uniform transversal pressure applied over a central region of the plate which is unrealistic for most cases, e.g., recent work from Pannell et al. (2021) has shown that the spatial distribution of blast loading from the cylindrical explosive is a Gaussian function.

Teeling-Smith and Nurick (1991b) experimentally examined the deformation and tearing of fully clamped circular mild steel plates under impulsive loadings. They proposed threshold velocities for prediction of the onset of failure modes II (tensile-tearing and deformation) and mode III (transverse shear) based on energy analysis. In their experiments, the blast loading is assumed to be uniform along the whole span of the plate. However, for

the case when the close-in explosion is considered, blast loading is much more localized instead of uniformly distributed.

The essence of above models is to identify the location of the point at which the maximum central deflection, material strength or critical velocity is reached but they are unable to predict the post-failure behaviour of plates under blast loading conditions. Additionally, blast loading distributions could differ greatly due to the various environment (buried (Rigby et al. 2018) or confined (Dennis et al. 2020)), charge shape (spherical or non-spherical (Langran-Wheeler et al. 2021; Rigby et al. 2021)) and scaled distance (far-field (Aune et al. 2015) or near field (Langran-Wheeler et al. 2021)) which not only limit the generalisability of existing predictive methods but also the comparison of those various experimental data presented by different researchers in the literature. Hence, there is a pressing need for the development of a generalized approach that could give rapid and accurate prediction of the failure response of plates subjected to the blast load with arbitrary magnitude and distribution.

Experimental investigations, despite require dedicated infrastructures and techniques to be efficiently and safely performed, are necessary to assess in detail the failure modes of plates when subjected to blast loadings. Teeling-Smith and Nurick (1991b) conducted a series of experiments to examine the failure of circular plates subjected to impulsive velocities. In this regard, an energy analysis based on test results was carried out to obtain an energy balance equation relating input, deformation, tearing and disc energies. Later on, the threshold velocities for the onset of failure Model II and III for circular plates were given. In the subsequent work of Nurick and Shave (1996), similar experimental work were reported, which studied the tearing of the clamped square plates under uniform impulsive loading and presented the threshold for the onset of failure Mode II and III as well. However, obtained conclusions only work for the behaviour of plates under uniformly distributed blast loading, that are not capable of predicting plate behaviour subjected to other loading conditions, such as localized blast loading. A series of experiments were implemented by S Chung Kim Yuen and his colleagues (Langdon et al. 2002; Yuen and Nurick 2005; Langdon et al. 2005) for the investigations on the deformation and tearing of built-in quadrangular stiffened plates subjected to uniform and localised blast loads. The experimental focus was on assessing the effect of different stiffener configurations (unstiffened, single, double, cross and double cross) on the failure modes and deformation of the plates. The blast load produced by the detonation of the plastic explosive was measured by a ballistic pendulum – a small, rigid metal plug embedded within a larger target surface which is a classical approach for close-in blast

parameters measurements. In recent times, this experimental approach was employed by the research team to investigate the transient response and failure of medium density fibreboard panels subjected to close proximity explosion loading (Langdon et al. 2021). Fuller (2018) conducted a detailed experimental investigation into shallow buried blast events and their effect on protective materials. By analysing the deflection profiles with different loading conditions, the plastic hinge was found to form at the centre of the target and travels towards the support under a highly concentrated impulsive loading. It was suggested that the failure onset area coincided with the location of maximum slope on the kinetic energy distribution across the target plate, which provides an insight to investigate the relationship between loading distribution and fracture onset location. Beside, an interesting conclusion drawn from Fuller was that non-uniform distributions of impulse impart more total kinetic energy to a target than uniformly distributed impulses of the same magnitude. Later on, this conclusion was well explained by the impulse enhancement parameter proposed by Rigby et al. (2019a) which was derived based on an energy balance concept.

Within the class of numerical approaches, extensive novel finite element models have been developed to study the failure response of blast-loaded plates. For instance, Rudrapatna et al. (1999) numerically studied the post-failure phase of clamped, thin square steel plates subjected to blast loading and proposed a failure criterion taking in to account bending, tension and transverse shear to predict the various failure modes. More recently, Moriello et al. (2020) used an finite element model that incorporates two competing mechanisms of damage due to ductile and shear failure to predict the failure and detachment path of impulsively loaded plates. It was shown that both the failure modes and the crack propagation path in the clamped plates under uniform impulsive loading could be predicted for a wide range of impulse intensity. They also performed the parametric study to investigate the influence of plate topology and boundary conditions on the failure response of plates and presented dimensionless failure maps for both square and rectangular plates. Again, the predictive ability of the output was hampered by a lack of consideration of the applied loading conditions.

Among the published analytical methods, it is worth citing the one based on the work by Mihailescu and Wierzbicki (2002). They presented a closed form wave solution to estimate the transverse deflection of a rigid-perfectly plastic circular membrane subjected to localised loading. The membrane was expected to fracture when the strain reaches a critical velocity. The threshold load for the membrane to fracture was developed based on the maximum slope of the final deflected shape. Later, the final deflected shape

predicted by the wave-type solution was supported by the numerical results by Lee and Wierzbicki (2005b,c). They presented a comparative study on the propagation of the radial cracks and proposed a ductile fracture criterion based on the equivalent plastic strain with the stress triaxiality for the initiation fracture site and extent of fracture prediction. Their work for the steel plates was complicated making it difficult to use, especially, for the intermediate engineers. Besides, their study was limited to a specific loading configuration considering only the response of plates under a rectangular shape distribution i.e. the form of the imparted load which is one of the main factors needed to be considered in a structural analysis was not investigated. Colton (1976) investigated the fracture pattern produced by localized impulsive loading on thick plates based on the Mindlin theory and qualitatively described their dependence on the magnitude and area of the load. A drawback of this work is that the conclusion only works for the loading arising from the explosive sheet which is assumed to be bi-linear while in real explosion scenarios, loading distribution could be more complicated.

It is a well known fact that the shape of a pressure pulse has a large influence on the dynamic plastic structural response when impact or blast loadings are considered. These loads are difficult to record and to reproduce in laboratory and practical conditions. Many authors have proposed procedures to characterize these loadings by overall representative parameters. Symonds and Wierzbicki (2019) proposed the use of peak load and loading impulse to represent an impact or blast loading pulse, whereas Abrahamson and Lindberg (1976) used these parameters to define a critical curve for structural failure.

Having looked at the studies available in the literature, it could be inferred that conduction of laboratory or field test involving blast loads is limited due to high cost and low practicality. Additionally, even for the available experimental results existing in the literature, comparison work among these are difficult and not always feasible due to the various test conditions and experimental techniques, such as different explosive material, explosive mass or different geometrical shapes. Furthermore, the high computational time required for the delivery of reasonable predictions also limits the numerical work substantially. Accordingly, employing the analytical approach could be a potential alternative for the experiments and numerical simulations. All aforementioned concerns motivated this study to develop a fast-running analytical approach capable of giving high confidence evaluation of the likely damage of plates will sustain under impulsive loadings with arbitrary known magnitude and distribution, to supplement existing predictive methodologies.

2.5 Summary

This chapter has focussed on the theoretical knowledge behind the shock formation of blast waves and current predictive methods used in blast protection engineering to predict effects of blast loadings on the dynamic response of structures, with a particular focus on the response of plated structures. Though some of the current predictive approaches, particularly the SDOF model, Biggs response charts and the P-I diagrams, are useful in assessing the response of the structure under blast loads, their application is limited to the either idealised loading or simple statistical definitions of damage under given loadings.

Existing plate theories on the analysis of response of plates has been reviewed, with a particular focus on the Mindlin plate of which the effect of transverse shear and rotatory inertia is of interest.

Failure modes of plates subjected to blast loads has been discussed, and current methods for predicting deformation and the failure behaviour of plates are introduced, as well as the emphasis of the effect of loading parameters on the failure response, which forms the main question that aiming to be solved in this thesis.

Knowledge of the effect of loading intensity and distribution on the failure behaviour of plates is an important aspect that leads to understanding the integral behaviour of the structure. Without it, we are unable to provide adequate and efficient protection systems such that reduce the loss of life and injuries to occupants, however, the level of scientific understand within this field remains limited. There is therefore a clear need for accurate, fast-running predictive tool to assist engineers to assess the likely damage a plated structure will sustain in the event of an accidental or malicious explosion.

Chapter 3

Analytical Method for Failure Prediction

THE purpose of this chapter is to develop an analytical solution for predicting failure behaviour of brittle plates subjected to blast loadings and quantify the effect of loading distribution and magnitude on the failure behaviour. The transient stress in the plate was firstly described by a system of hyperbolic partial differential equations. To solve the equations, characteristic method were employed to transform the original partial differential equations into ordinary differential equations along characteristic lines. The values of the state variable at the interior, origin and boundary points on the network constructed by the characteristic lines were later determined by employing the finite difference scheme. The impulse enhancement factor was invoked to measure the uniformity of the distribution of the load. Detailed calculation examples could be found in the Chapter 4, 5 and 6.

3.1 Introduction

Although classical plate theory is the most commonly employed theory for practical analysis, one of its key assumptions -the normals to the mid-plane of the undeformed plate remain normal to the deformed mid-plane is not always the case in real-life events and could not give good results for sharp transient or higher modes' vibration especially for intense loading. Conversely, Mindlin plate theory (Mindlin 1951) is less restrictive

and more realistic in which the normals to the mid-plane of the undeformed plate not necessarily normal to the deformed mid-plane so that both effects of traverse shear deformation and rotary inertia could be taken into consideration. Therefore, our analysis starts from the Mindlin plate theory which is a two-dimensional theory of flexural motion of elastic plates deduced from the three-dimensional equations of equations.

3.2 Problem Definition

3.2.1 Assumptions and Plate Geometry

The plates examined in the current study are assumed to be linearly-elastic, homogeneous, isotropic of uniform thickness and undergoing small deformations due to impulsive loading alone in the absence of in-plane forces.

A schematic of a Mindlin circular plate of radius R and uniform thickness h, oriented with reference to polar coordinate system (r,θ,z) is illustrated in Figure 3.1. Three field variables are used to express the displacements along r, θ and z, which are

$$u_r \approx -z * \psi_r(r,\theta,t), u_\theta \approx -z * \psi_\theta(r,\theta,t), w \approx w(r,\theta,t) \tag{3.1}$$

where t is the time, w the transverse displacement, and ψ_r and ψ_θ are the angular rotations of the normal to the neutral surface (the mid-plane which remains free of in-plane stress/strain) in radial and circumferential directions due the plate bending, respectively.

3.2.2 Governing Equations

The resultant moments M_r, M_θ and $M_{r\theta}$, and the shearing forces Q_r and Q_θ, as shown in the Figure 3.2, can be obtained by integrating the stresses and the moment of stresses through the thickness of the plate, represented by Eq.(3.2). Both moments and shearing forces change as one moves through a distance dr or $d\theta$. For the sake of brevity, the

incremented quantities in the r-direction and the θ-direction are denoted by using a single star and a double star, respectively.

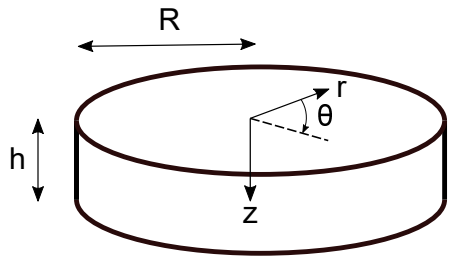

Figure 3.1: Schematic of plate

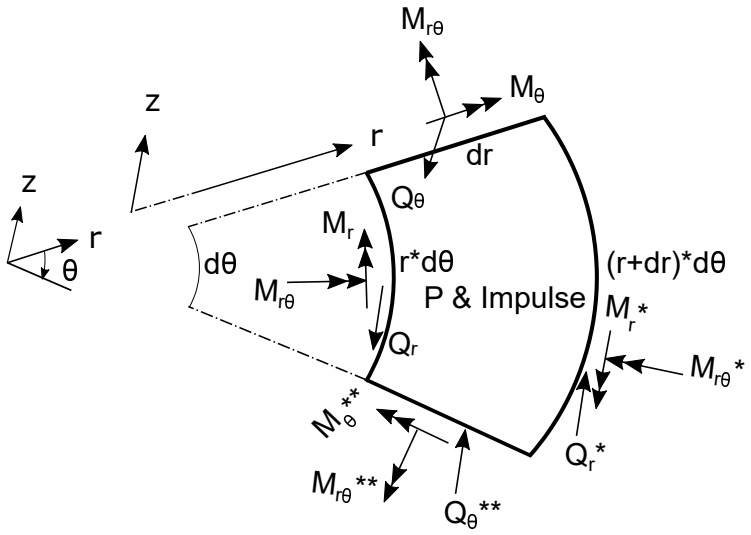

Figure 3.2: Equilibrium of a plate element

$$
\begin{aligned}
M_r &= -D\{\frac{\partial \psi_r}{\partial r} + \frac{\nu}{r}(\psi_r + \frac{\partial \psi_\theta}{\partial \theta})\} = 0 \\
M_\theta &= -D\{\frac{1}{r}(\psi_r + \frac{\partial \psi_\theta}{\partial \theta}) + \nu\frac{\partial \psi_r}{\partial r}\} = 0 \\
M_{r\theta} &= -\frac{D}{2}(1-\nu)\{\frac{1}{r}(\frac{\partial \psi_r}{\partial \theta} - \psi_\theta) + \frac{\psi_\theta}{\partial r}\} = 0 \\
Q_r &= kGh(-\psi_r + \frac{\partial w}{\partial r}) \\
Q_\theta &= kGh(-\psi_\theta + \frac{1}{r}\frac{\partial w}{\partial \theta})
\end{aligned}
\tag{3.2}
$$

where E, $D = Eh^3/12(1-\nu^2)$, G, ν are Young's modulus, the flexural rigidity, the shear modulus, Poison's ratio respectively. Here k is the shear correction factor and for isotropic homogeneous plates, the most commonly used values for k are taken as $k = 0.76 + 0.3 * \nu$ (Bhaskar and Varadan 2014) which allows the prediction for plates with various Poison's ratio.

The equations of motion for rotation and for translation are given by

$$
\begin{aligned}
\frac{\partial M_r}{\partial r} + \frac{1}{r}\frac{\partial M_{r\theta}}{\partial \theta} + \frac{M_r - M_\theta}{r} - Q_r + \frac{\rho h^3 \partial^2 \psi_r}{12\partial t^2} &= 0 \\
\frac{\partial M_{r\theta}}{\partial r} + \frac{1}{r}\frac{\partial M_\theta}{\partial \theta} + 2\frac{M_{r\theta}}{r} - Q_\theta + \frac{\rho h^3 \partial^2 \psi_\theta}{12\partial t^2} &= 0 \\
\frac{\partial Q_r}{\partial r} + \frac{1}{r}\frac{\partial Q_\theta}{\partial \theta} + \frac{Q_r}{r} + P - \rho h\frac{\partial^2 w}{\partial t^2} &= 0
\end{aligned}
\tag{3.3}
$$

where P is the applied transverse pressure P of which the general form will be discussed later in section 3.6. ρ is the density and h is the thickness of the plate.

3.2.3 Simplification of the Governing Equations

For the special case of axisymmetric loading and axisymmetric boundary conditions, the governing equations get simplified with $\frac{\partial(...)}{\partial \theta} = 0$, the Eq.(3.2) and Eq.(3.3) are grouped below

$$\begin{cases} \dfrac{\partial M_r}{\partial r} + \dfrac{M_r - M_\theta}{r} - Q_r + \dfrac{\rho h^3 \partial^2 \psi_r}{12 \partial t^2} = 0 & \text{(3.4a)} \\ \dfrac{\partial Q_r}{\partial r} + \dfrac{Q_r}{r} + P - \rho h \dfrac{\partial^2 w}{\partial t^2} = 0 & \text{(3.4b)} \\ M_r + D\{\dfrac{\partial \psi_r}{\partial r} + \dfrac{\nu}{r}\psi_r\} = 0 & \text{(3.4c)} \\ M_\theta + D\{\dfrac{1}{r}\psi_r + \nu \dfrac{\partial \psi_r}{\partial r}\} = 0 & \text{(3.4d)} \\ Q_r = kGh(-\psi_r + \dfrac{\partial w}{\partial r}) & \text{(3.4e)} \end{cases}$$

Then Eq.(3.4c)-(3.4e) are differentiated with respect to time, and two new variables are introduced

$$W = \frac{\partial \psi_r}{\partial t}, V = \frac{\partial w}{\partial t} \tag{3.5}$$

where, W and V are angular rotation velocity and transverse velocity.

Substituting Eq.(3.5) into the Eq.(3.4), the governing equations can be written in the following matrix form

$$\begin{aligned} &\begin{bmatrix} 0 & 0 & D & 0 & 0 \\ 0 & 0 & 0 & -kGh & 0 \\ \frac{12}{\rho h^3} & 0 & 0 & 0 & 0 \\ 0 & -\frac{1}{\rho h} & 0 & 0 & 0 \\ 0 & 0 & \nu D & 0 & 0 \end{bmatrix} \begin{bmatrix} M_r \\ Q_r \\ W \\ V \\ M_\theta \end{bmatrix}_r + \begin{bmatrix} M_r \\ Q_r \\ W \\ V \\ M_\theta \end{bmatrix}_t \\ &= \begin{bmatrix} -\frac{\nu D}{r} W \\ -kGhW \\ -\frac{12}{\rho r h^3}(M_r - Q_r r - M_\theta) \\ \frac{1}{\rho r h}(Q_r + Pr) \\ -\frac{D}{r} W \end{bmatrix} \end{aligned} \tag{3.6}$$

When written in its abbreviated form, it reads

$$AU_r + U_t = B \tag{3.7}$$

3.3 Characteristic Method

An outstanding challenge for the numerical example given in this study is to solve a system of hyperbolic partial differential equations(PDEs) that describe the transient stress in the plate, where the exact or near-to-exact solution to this system, however, can be impossible to reach without the help of mathematical tool. Hence, instead of solving 5 dependent variables differentiated with respect to both space and time, it would be advantageous to replace them by equivalent equations each involving only a total derivative in a particular direction in the $r-t$ plane. The method of characteristics(MOC) offers the potential to transform the original PDEs into ordinary differential equations(ODEs) along the special curves that called characteristic lines. These ODEs are subsequently transformed into a set of difference equations which enables the solution be readily obtained through numerical integration and interpolation scheme. This method can be applied to linear, semi-linear, or quasilinear PDEs and has been widely used for transient analysis of Timoshenko's beam (Leonard and Budiansky 1955), shells (Spillers 1965) and other elastic wave problems (Chou and Mortimer 1967).

3.3.1 Eigenvalues and Eigenvectors

Characteristic lines are defined as these particular curves $r = r(t)$ in the $r-t$ plane, along which the PDEs become ODEs. Consider $r = r(t)$ and regard 5 dependent variables as the function of t only. The relation governing the variation of 5 dependent variables along these characteristic lines will be called characteristic equations.

When using the MOC, the governing equations Eq.(3.7) in its differential form are firstly replaced by the finite-difference Eq.(3.8) along the characteristic lines.

$$d[L^i U] = L^i B dt \tag{3.8}$$

where L^i is the left eigenvector of the matrix A corresponding to the eigenvalue λ_i of the matrix A such that

$$L^i A = \lambda_i L^i \tag{3.9}$$

Physically, eigenvalues represent speeds of propagation of information which is equivalent to the slope of the curve $r = r(t)$ in the $r - t$ plane.

For the Eq.(3.8), the slopes of the characteristic lines in the $r - t$ plane are

$$\lambda_i = \frac{dr}{dt} = \begin{cases} \lambda_1 = \sqrt{\frac{12D}{\rho h^3}} & along\, I^+ \\ -\lambda_2 = -\sqrt{\frac{12D}{\rho h^3}} & along\, I^- \\ \lambda_3 = \frac{\sqrt{Gk}}{\rho} & along\, II^+ \\ -\lambda_4 = -\frac{\sqrt{Gk}}{\rho} & along\, II^- \\ \lambda_5 = 0 & along\, III \end{cases} \tag{3.10}$$

where $I^{\pm}, II^{\pm}$ and III are the five characteristic lines that construct the whole network.

The corresponding eigenvectors are

$$\begin{aligned} L^1 = \begin{bmatrix} \sqrt{\frac{12}{D\rho h^3}} \\ 0 \\ 1 \\ 0 \\ 0 \end{bmatrix}, L^2 = \begin{bmatrix} -\sqrt{\frac{12}{D\rho h^3}} \\ 0 \\ 1 \\ 0 \\ 0 \end{bmatrix}, L^3 = \begin{bmatrix} 0 \\ \sqrt{\frac{1}{Gk\rho h^2}} \\ 0 \\ 1 \\ 0 \end{bmatrix}, \\ L^4 = \begin{bmatrix} 0 \\ -\sqrt{\frac{1}{Gk\rho h^2}} \\ 0 \\ 1 \\ 0 \end{bmatrix}, L^5 = \begin{bmatrix} -\nu \\ 0 \\ 0 \\ 0 \\ 1 \end{bmatrix} \end{aligned} \tag{3.11}$$

3.3.2 Characteristic Equations

By substituting the corresponding eigenvectors into Eq.(3.10), the five characteristic differential forms of the governing equations are grouped below

$$Along\, I^+ : dM_r + \frac{\rho h^3 c_p dW}{12} = -\frac{\nu\rho h^3 c_p^2}{12r} W dt - \frac{c_p}{r}(M_r - Q_r r - M_\theta)dt \tag{3.12a}$$

$$Along\, I^- : dM_r - \frac{\rho h^3 c_p dW}{12} = -\frac{\nu\rho h^3 c_p^2}{12r} W dt + \frac{c_p}{r}(M_r - Q_r r - M_\theta)dt \tag{3.12b}$$

$$Along\, II^+ : dQ_r - \rho h c_s dV = -\rho h c_s^2 W dt - \frac{c_s}{r}(Q_r + Pr)dt \tag{3.12c}$$

$$Along\, II^- : dQ_r + \rho h c_s dV = -\rho h c_s^2 W dt + \frac{c_s}{r}(Q_r + Pr)dt \tag{3.12d}$$

$$Along\, III : dM_r - \frac{1}{\nu} dM_\theta = \frac{\rho h^3 c_p^2}{12r}(\frac{1-\nu^2}{\nu})W dt \tag{3.12e}$$

It is convenient to introduce the following dimensionless quantities:

$$\begin{aligned} &\xi = \frac{r\sqrt{12}}{h}, \tau = \frac{t c_p \sqrt{12}}{h}, \beta = \frac{c_p}{c_s}, \overline{M} = \frac{M_r h}{D}, \overline{W} = \frac{W h}{c_p}, \\ &\overline{Q} = \frac{Q_r h^2}{D\sqrt{12}}, \overline{N} = \frac{M_\theta h}{\nu D}, \overline{V} = \frac{V\sqrt{12}}{\beta c_p}, \alpha = \frac{1-\nu^2}{\nu}, \overline{P} = \frac{P h^3}{12D} \end{aligned} \tag{3.13}$$

With above quantities, Eq.(3.12a) to Eq.(3.12e) take the form

$$Along\, I^+ : d\overline{M} + d\overline{W} = -\left[\frac{\nu}{\xi}\overline{W} + \frac{1}{\xi}(\overline{M} - \overline{Q}\xi - \nu\overline{N})\right] d\tau \tag{3.14a}$$

$$Along\, I^- : d\overline{M} - d\overline{W} = -\left[\frac{\nu}{\xi}\overline{W} - \frac{1}{\xi}(\overline{M} - \overline{Q}\xi - \nu\overline{N})\right] d\tau \tag{3.14b}$$

$$Along\, II^+ : d\overline{Q} - d\overline{V} = \left[-\frac{1}{\beta^2}\overline{W} - \frac{1}{\xi\beta}(\overline{Q} + \overline{P}\xi)\right] d\tau \tag{3.14c}$$

$$Along\, II^- : d\overline{Q} + d\overline{V} = \left[-\frac{1}{\beta^2}\overline{w} + \frac{1}{\xi\beta}(\overline{Q} + \overline{P}\xi)\right] d\tau \tag{3.14d}$$

$$Along\, III : d\overline{M} - d\overline{N} = \alpha\frac{\overline{W}}{\xi} d\tau \tag{3.14e}$$

3.3.3 Discontinuity Propagation

When using characteristic method, discontinuities in state variables may exist across the characteristic lines, i.e. possible second derivatives of state variables may be discontinuous.

The equations governing the propagation of these discontinuities will be derived following the general procedure given by Leonard and Budiansky (1955) and Jahsman (1958).

Let a and b are two points on a I^- characteristic line on either side of a particular I^+ characteristic line as shown in Figure 3.3.

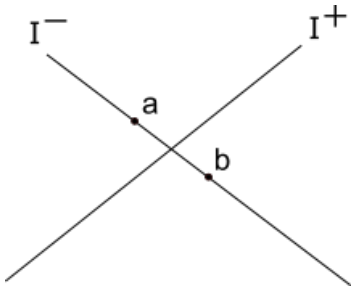

Figure 3.3: Propagation of discontinuities across I^-

If a discontinuity of any state variable exists across the I^+ characteristic line, then its value can not be governed by Eq.(3.14). Instead, this discontinuity is determined by integrating the characteristic equitations along all characteristic lines which across the I^+ characteristic line. For instance, if M is discontinuous across the I^+ characteristic lines, then $M_b - M_a$ retains a finite value δM as a and b are allowed to approach the I^+ characteristic line from either side. Consequently, integration of the other 4 equations in Eq.(3.14) gives

$$across\ I^+ \begin{cases} \delta\overline{M} = \delta\overline{W} \\ \delta\overline{N} = \delta\overline{M} \\ \delta\overline{Q} = \delta\overline{V} = 0 \end{cases} \tag{3.15}$$

Similarly, discontinuities across the other characteristic lines can be readily shown to satisfy:

$$across\ I^- \begin{cases} \delta\overline{M} = -\delta\overline{W} \\ \delta\overline{N} = \delta\overline{M} \end{cases} \tag{3.16}$$

$$across\ II^+\ \ \delta\overline{Q} = -\delta\overline{V} = 0 \tag{3.17}$$

$$across\ II^-\ \ \delta\overline{Q} = \delta\overline{V} = 0 \tag{3.18}$$

$$across\ III\ \ \delta\overline{N} = k_1 \tag{3.19}$$

where k_1 can be any value.

The variations in the magnitude of a discontinuity as one proceeds along a characteristic line could be determined in the following manner. For example, to determine how δM and δW vary along the I^+, Eq.(3.15) is written for both the upper side and the lower side of the I^+ characteristic line, and the difference of the two equations yields

$$Along\, I^+ : d(\delta\overline{M}) + d(\delta\overline{W}) = -\left[\tfrac{\nu}{\xi}\delta\overline{W} + \tfrac{1}{\xi}(\delta\overline{M})\right] d\tau \tag{3.20}$$

Eliminating $\delta\overline{W}$ by using Eq.(3.14) gives

$$Along\, I^+ : \tfrac{2d(\delta\overline{M})}{\delta\overline{M}} = -(\tfrac{\nu+1}{\xi})d\xi \tag{3.21}$$

By carrying out the basic integral operation, solution of this equations gives

$$Along\, I^+ : \delta\overline{M} = k_2\ \xi^{-1/2} \tag{3.22}$$

where k_2 can be arbitrary constant. It can be shown that the identical relationship holds for other 3 discontinuities $\delta\overline{W}, \delta\overline{Q}, \delta\overline{V}$, i.e. these discontinuities also vary as $\xi^{-1/2}$. While discontinuities in $\overline{N}$ are constant along the III characteristic line.

3.3.4 Fracture Criterion

The fracture criterion used in the analysis is that of maximum normal stress. Hence, brittle fracture under tensile stresses due to bending occurs whenever the principal stress reaches σ_{max}, the fracture stress in uniaxial loading. Furthermore, the fracture line is perpendicular to the direction of this principal stress. In terms of stress resultants the maximum normal stress criterion for brittle fracture is

$$M_r = \pm\frac{h^2\sigma_{max}}{6}, M_\theta = \pm\frac{h^2\sigma_{max}}{6} \tag{3.23}$$

3.4 Solution toward Stress Resultants

3.4.1 Typical Interior Point

In this study, there are five families of characteristic lines in the $\xi - \tau$ plane, with each characteristic intersecting every one of the other four characteristic families, as shown in Figure 3.4. Numerical calculation based on the network constructed by these five characteristic lines is not practical due to the redundant irregular mesh points. Therefore, for simplicity, only I^+ and I^- characteristic lines are used as the main network.

The basic approach for solving differential equations numerically is to transform the continuous equations into discrete equations, which can be solved using a computational algorithm to obtain an approximate solution of the original differential equations. Finite Difference Method (FDM) is one of the available numerical method which can easily be applied to solve these differential equations and has been widely used (Langtangen and Linge 2017; Sun 1996; Savović et al. 2022; Özişik et al. 2017).

Making use of this approximation to replace partial derivatives, the partial differential equations are converted into difference equations and the resultant system of algebraic equations are solved using the iterative method. The script for the solution toward stress resultants is given in the Appendix A.1. The values of the state variables at a typical interior point A, shown in Figure 3.4, are determined by their values at points B, C, G, E, F by solving the finite difference form of all five characteristic equations.

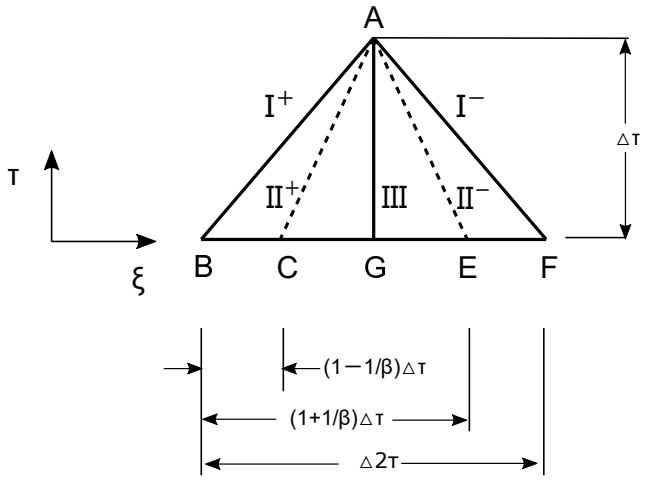

Figure 3.4: Typical interior point

Let the differential equations Eq.(3.14) be replaced by the finite difference equations

$$
\begin{aligned}
Along\, I^{+} : (\overline{M}_A - \overline{M}_B) + (\overline{W}_A - \overline{W}_B) &= -\left[\nu(\frac{\overline{W}_A}{\xi_A} + \frac{\overline{W}_B}{\xi_B}) + (\frac{\overline{M}_A - \nu\overline{N}_A}{\xi_A} + \frac{\overline{M}_B - \nu\overline{N}_B}{\xi_B})\right. \\
&\quad \left. - (\overline{Q}_A + \overline{Q}_B)\right]\frac{\Delta\tau}{2} \\
Along\, I^{-} : (\overline{M}_A - \overline{M}_F) - (\overline{W}_A - \overline{W}_F) &= -\left[\nu(\frac{\overline{W}_A}{\xi_A} + \frac{\overline{W}_F}{\xi_F}) - (\frac{\overline{M}_A - \nu\overline{N}_A}{\xi_A} + \frac{\overline{M}_F - \nu\overline{N}_F}{\xi_F})\right. \\
&\quad \left. + (\overline{Q}_A + \overline{Q}_F)\right]\frac{\Delta\tau}{2} \\
Along\, II^{+} : (\overline{Q}_A - \overline{Q}_C) - (\overline{V}_A - \overline{V}_C) &= \left[-\frac{1}{\beta^2}(\overline{W}_A + \overline{W}_c) - \frac{1}{\beta}(\frac{\overline{Q}_A}{\xi_A} + \frac{\overline{Q}_C}{\xi_C})\right. \\
&\quad \left. - \frac{1}{\beta}(\overline{P}_A + \overline{P}_C)\right]\frac{\Delta\tau}{2} \\
Along\, II^{-} : (\overline{Q}_A - \overline{Q}_E) + (\overline{V}_A - \overline{V}_E) &= \left[-\frac{1}{\beta^2}(\overline{W}_A + \overline{W}_E) + \frac{1}{\beta}(\frac{\overline{Q}_A}{\xi_A} + \frac{\overline{Q}_E}{\xi_E})\right. \\
&\quad \left. + \frac{1}{\beta}(\overline{P}_A + \overline{P}_E)\right]\frac{\Delta\tau}{2} \\
Along\, III : (\overline{M}_A - \overline{M}_G) - (\overline{N}_A - \overline{N}_G) &= (\frac{\overline{W}_A}{\xi_A} + \frac{\overline{W}_G}{\xi_G})\frac{\alpha\Delta\tau}{2}
\end{aligned}
\tag{3.24}
$$

The quantities at points C, G, and E are expressed in terms of those at points B and F by linear interpolation. Thus, the resulting system of linear algebraic equations in the unknown quantities at point A expressed in the matrix form can be written as

$$
\begin{bmatrix}
0 & 2 & \frac{\nu\Delta\tau}{\xi_A} & 0 & 0 \\
0 & 0 & -1 - \frac{\Delta^2}{4}[\frac{1}{\beta^2} - \frac{\nu-1}{\xi_A^2}] & 0 & 0 \\
2 & 0 & \frac{\Delta\tau}{\beta^2} & 0 & 0 \\
-\frac{\Delta\tau}{2\beta\xi_A} & 0 & 0 & 1 & 0 \\
0 & 1+\frac{\alpha}{\nu} & 0 & 0 & -1
\end{bmatrix}
\begin{bmatrix}
\overline{Q}_A \\ \overline{M}_A \\ \overline{W}_A \\ \overline{V}_A \\ \overline{N}_A
\end{bmatrix}
=
\begin{bmatrix}
B1 \\ B2 \\ B3 \\ B4 \\ B5
\end{bmatrix}
\tag{3.25}
$$

where

$$
\begin{aligned}
B1 &= A1 + A2 \\
B2 &= A2 - \frac{1}{2}(A1 + A2) + \frac{\nu\Delta\tau}{2\xi_A}\left[A5 + \frac{\alpha}{2\nu}(A1 + A2)\right] - \frac{\Delta\tau}{4}(A3 + A4) \\
&\quad + \frac{\nu - 1}{\nu}\frac{\Delta\tau}{4\xi_A}(A1 + A2) \\
B3 &= A3 + A4 \\
B4 &= A4 - \frac{1}{2}(A3 + A4) \\
B5 &= A5 + \frac{\alpha}{2\nu}(A1 + A2)
\end{aligned}
\tag{3.26}
$$

and

$$
\begin{aligned}
A1 &= \overline{M}_B + \overline{W}_B - \frac{1}{2}\Delta\tau\left(\frac{\overline{M}_B - \nu\overline{N}_B}{\xi_B} - \overline{Q}_B + \frac{\nu\overline{W}_B}{\xi_B}\right) \\
A2 &= \overline{M}_F - \overline{W}_F - \frac{1}{2}\Delta\tau\left(-\frac{\overline{M}_F - \nu\overline{N}_F}{\xi_F} + \overline{Q}_F + \frac{\nu\overline{W}_F}{\xi_F}\right) \\
A3 &= \overline{Q}_B - \overline{V}_B - \Delta\tau\left[\frac{\overline{W}_B - \frac{(\overline{W}_B - \overline{W}_F)(\beta-1)}{2\beta}}{\beta^2} + \frac{\frac{\overline{Q}_B}{\xi_B} - \frac{(\frac{\overline{Q}_B}{\xi_B} - \frac{\overline{Q}_F}{\xi_F})(\beta-1)}{2\beta}}{\beta})\right] \\
&\quad - \frac{(\overline{Q}_B - \overline{Q}_F)(\beta - 1)}{2\beta} + \frac{(\overline{V}_B - \overline{V}_F)(\beta - 1)}{2\beta} \\
A4 &= \overline{Q}_B + \overline{V}_B - \Delta\tau\left[\frac{\overline{W}_B - \frac{(\overline{W}_B - \overline{W}_F)(\beta+1)}{2\beta}}{\beta^2} - \frac{\frac{\overline{Q}_B}{\xi_B} - \frac{(\frac{\overline{Q}_B}{\xi_B} - \frac{\overline{Q}_F}{\xi_F})(\beta+1)}{2\beta}}{\beta}\right] \\
&\quad - \frac{(\overline{Q}_B - \overline{Q}_F)(\beta + 1)}{2\beta} - \frac{(\overline{V}_B - \overline{V}_F)(\beta + 1)}{2\beta} \\
A5 &= \frac{1}{2}\overline{M}_B + \frac{1}{2}\overline{M}_F - \frac{1}{2}\overline{N}_B - \frac{1}{2}\overline{N}_F + \frac{1}{4}\alpha\Delta\tau\left(\frac{\overline{W}_B}{\xi_B} + \frac{\overline{W}_F}{\xi_F}\right)
\end{aligned}
\tag{3.27}
$$

Then the unknown quantities at point A are found from Eq.(3.25) by expanding the matrix notation into five algebraic equations and successively solving for $\overline{M}, \overline{Q}, \overline{W}, \overline{V}$ and $\overline{N}$. The solution is

$$\begin{aligned}
\overline{W}_A &= -\frac{B_2}{1+\frac{\Delta\tau^2}{4}(\frac{1}{\beta^2}-\frac{\nu-1}{\xi_A^2})} \\
\overline{M}_A &= \frac{1}{2}(B_1 - \frac{\nu\Delta\tau}{\xi_A}\overline{W}_A) \\
\overline{Q}_A &= \frac{1}{2}(B3 - \frac{\Delta\tau}{\beta^2}\overline{W}_A) \\
\overline{V}_A &= B_4 + \frac{\Delta\tau}{2\beta\xi_A}\overline{Q}_A \\
\overline{N}_A &= -B_5 + (1+\frac{\alpha}{\nu})\overline{M}_A
\end{aligned} \tag{3.28}$$

3.4.2 Origin Point

In contrast to interior points, specific treatments are required for both origin and boundary points. For mesh points at the origin and boundary, from axial symmetry, two of the five state variables are absent leaving the three remaining state variables as unknowns. The three unknown state variables are then determined by the finite difference form of three characteristic equations represented by Eq.(3.24) associated with the three remaining characteristic lines.

Furthermore, from the Eq.(3.24), one should consider the limits of $\frac{\overline{Q}}{\xi}$, $\frac{\overline{W}}{\xi}$ and $\frac{\overline{M}-\nu\overline{N}}{\xi}$ as $\xi \to 0$ for the origin points. From axisymmetry and through the Taylor's theorem, three limits in the non-dimensional form can be written as represented in Eq.(3.29):

$$\frac{\overline{W}}{\xi} = -\frac{\overline{M}_\tau}{(1+\nu)} \qquad as\ \xi \to 0 \tag{3.29a}$$

$$\frac{\overline{Q}}{\xi} = \frac{1}{2}(\beta\overline{V}_\tau - \overline{P}) \qquad as\ \xi \to 0 \tag{3.29b}$$

$$\frac{\overline{M}-\nu\overline{N}}{\xi} = 0 \qquad as\ \xi \to 0 \tag{3.29c}$$

where $\overline{M}_\tau$ and $\overline{V}_\tau$ are the slopes of the target points,

Again, from axial symmetry, two of the five state variables $\overline{W}$ and $\overline{Q}$ vanish written as

$$\overline{W}_A = 0, \overline{Q}_A = 0 \tag{3.30}$$

The three characteristic equations used for the calculation of the three unknown state variables at the origin point A are those associated with the I^-, II^-, III characteristic lines, as shown in Figure 3.5.

By substituting Eq.(3.29) and Eq.(3.30) into second of Eq.(3.24), three remaining unknown variables are calculated as shown in Eq.(3.31)

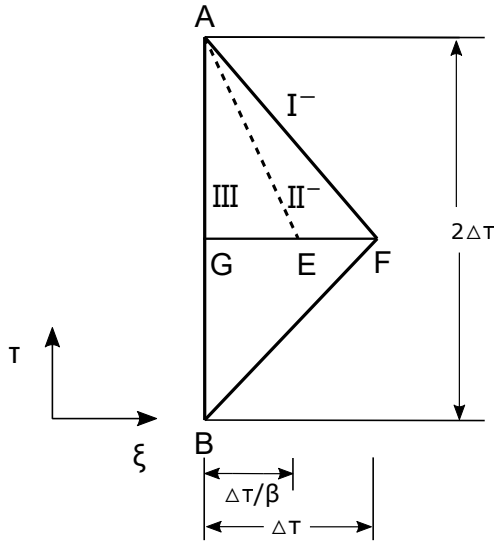

Figure 3.5: The origin point

$$
\begin{aligned}
\overline{M}_A &= \frac{(1+\frac{\Delta\tau}{2\xi_A})\overline{M}_F - \frac{\Delta\tau\nu}{2\xi_F}\overline{N}_F - (1+\frac{\Delta\tau\nu}{2\xi_F})\overline{W}_F - \frac{1}{2}\Delta\tau\overline{Q}_F - \frac{\nu}{4(1+\nu)}\overline{M}_D}{\frac{4+3\nu}{4+4\nu}} \\
\overline{V}_A &= \frac{\frac{1}{\beta}\overline{Q}_F + \frac{3\beta-4}{8\beta}\overline{V}_D + \frac{1}{\beta}\overline{V}_F - \frac{\Delta\tau}{2\beta^3}\overline{W}_F - \frac{\beta-1}{16\beta}\overline{V}_z + \frac{\Delta\tau}{2\beta^2}\frac{\overline{Q}_F}{\xi_F}}{\frac{5\beta+9}{16\beta}} \\
\overline{N}_A &= \frac{1}{\nu\overline{M}_A}
\end{aligned}
\tag{3.31}
$$

3.4.3 Boundary Point

In this study, the boundary condition for a fully clamped plate can be represented as shown in Eq.(3.32)

$$\overline{W}_A = 0, \overline{V}_A = 0 \tag{3.32}$$

The three characteristic equations used for the calculation of the three unknown state variables at the clamped boundary point A are those associated with the I^+, II^+, III characteristic lines, as shown in Figure 3.6.

By substituting Eq.(3.32) into Eq.(3.24), three remaining unknown variables are calculated as shown in Eq.(3.33)

$$\begin{aligned}
\overline{Q}_A &= \frac{\frac{1}{\beta}\overline{Q}_B - \frac{1}{\beta}\overline{V}_B + \frac{\beta-1}{2\beta}\overline{Q}_D - \frac{\Delta\tau}{2\beta^3}\overline{W}_B - \frac{\Delta\tau}{2\beta^2}\frac{\overline{Q}_B}{\xi_B} - \frac{\beta-1}{4\beta^2}\Delta\tau\frac{\overline{Q}_D}{\xi_D}}{\frac{\beta+1}{2\beta} + \frac{3\beta-1}{4\beta^2}\frac{\Delta\tau}{\xi_A}} \\
\overline{M}_A &= \frac{-\frac{\Delta\tau\nu}{2\xi_A}\overline{M}_D + \frac{\Delta\tau\nu}{2\xi_A}\overline{N}_D + \overline{M}_B + \overline{W}_B - \frac{\Delta\tau\nu}{2\xi_B}\overline{W}_B - \frac{\Delta\tau}{2\xi_B}(\overline{M}_B - \nu\overline{N}_B) + \frac{1}{2}\Delta\tau(\overline{Q}_A + \overline{Q}_B)}{1 + \frac{\Delta\tau}{2\xi_A} - \frac{\Delta\tau\nu}{2\xi_A}} \\
\overline{N}_A &= \overline{M}_A - \overline{M}_D + \overline{N}_D
\end{aligned} \tag{3.33}$$

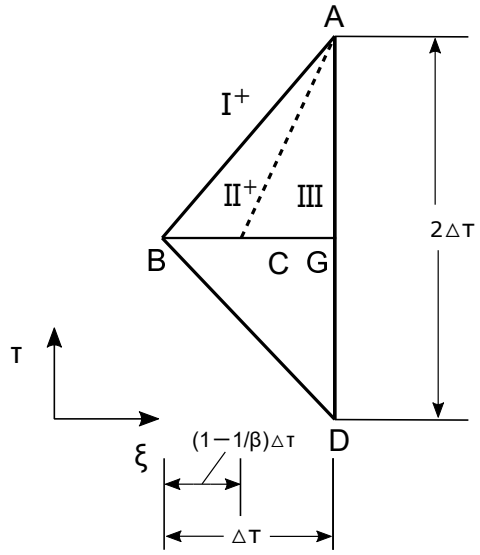

Figure 3.6: The boundary point

3.5 Initial Conditions

According to the characteristic equations Eq.(3.24), the values of the state variables at a mesh point in the $\xi - \tau$ plane are determined by the values of the state variables along all characteristic lines leading to that point. Therefore, starting values of the state variables should be specified if all values of them over the entire $\xi - \tau$ plane are to be determined. That is, the values of all five state variables $\overline{M}, \overline{N}, \overline{Q}, \overline{V}, \overline{W}$, over the entire domain of ξ of interest are specified on the $\tau = 0$ curve (the ξ-axis). Hence, the values of interest, e.g., stress at any location on the front face or back face of the plate at any time could be obtained once the initial applied velocity or impulse is known.

3.6 Blast Loading and Impulse Enhancement Factor

3.6.1 Loading Shapes

In the event that high explosive detonation in contact with a structure, the induced structural behaviour under such intense dynamic loading with sudden application, short duration and extremely high magnitude is different to that observed subjected to static loading. When the loading duration is short enough, typically less than tenth of the structure's natural period, structure itself has no time to deform therefore no significant displacement is observed (Cormie et al. 2009). In these so-called impulsive loading scenarios, the external energy is entirely in the form of kinetic energy since the strain energy is negligible. This causes an initially stationary structure to acquires a instantaneous velocity. In this study, the explosive load was applied to the brittle plate in the form of an impulse loading and the induced structural behaviour was dominated by the kinetic energy.

The shock wave produced from the expansion of the detonation gaseous product is characterised by a sharp rise to peak pressure followed by a exponential decay back to ambient conditions. This shock wave contains the most of the energy released by the explosion and interacts with the structure it encountered via a momentum transfer. The loading distribution applied on the structure is given by a specific impulse distribution

which is the integral of pressure-time history at selected locations. Experimental work in (Rigby et al. 2019b) demonstrated that the initial velocity uptake of a plate is directly proportional to the distributed specific impulse. Thus, conservation of momentum at $t = 0$ implies that

$$v = \frac{i}{\rho h} \tag{3.34}$$

where v is the initial impulsive velocity distributed over the plate and i is the specific impulse.

The distribution of initial velocity resulting from impulsive loading was derived which would be applied on the every node of target directly using a Matlab script given in the Appendix A2.

As one of the most important factors that need to be considered in a structural analysis, the distribution of explosion loadings differ greatly according to a variety of factors as we have discussed in section 2.4.3. From author's knowledge, in almost all the published studies, there are 5 most commonly used blast spatial loading profiles in the literature, as summarised in Figure 3.7.

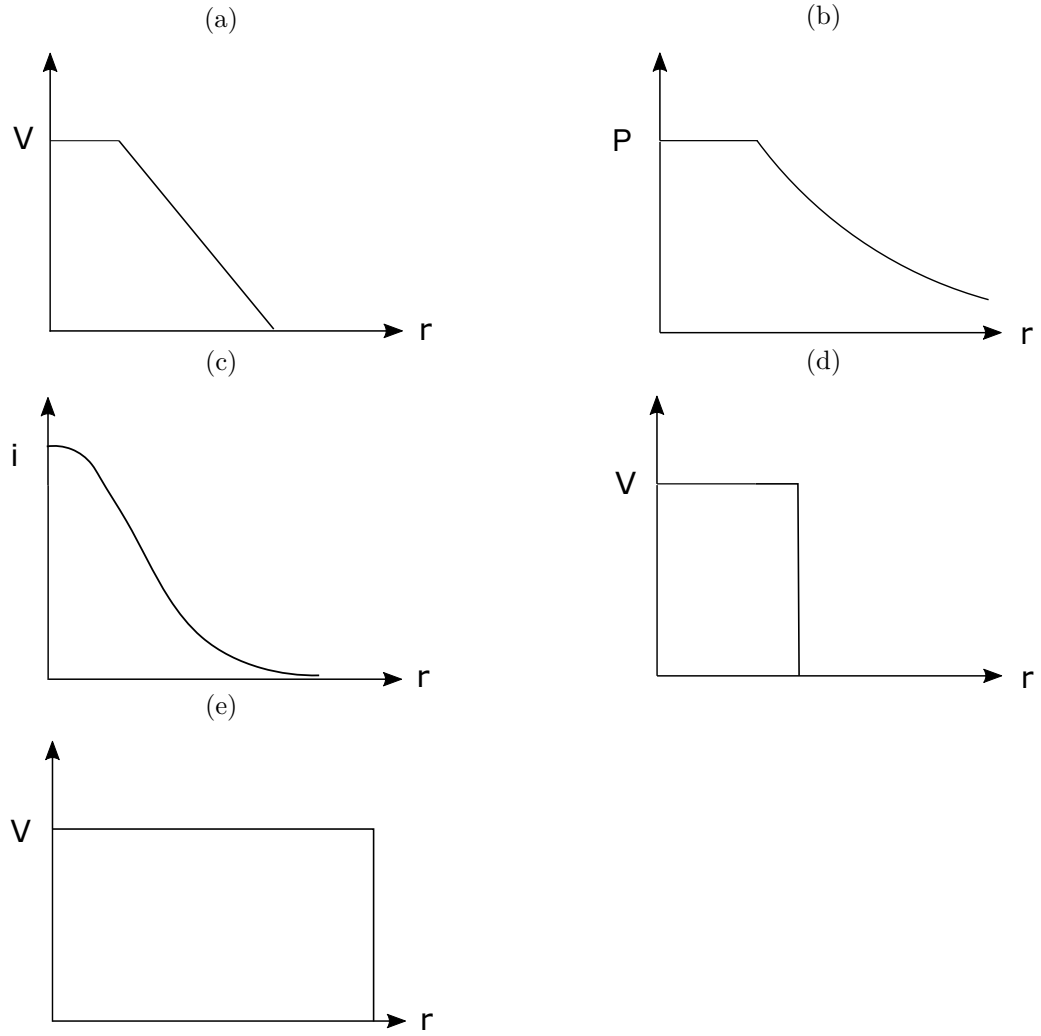

Figure 3.7: Common blast loading distributions: (a) Bi-linear distribution (after Colton (1976), vertical axis is the velocity and horizontal axis is the distance away from the origin); (b) Linear exponentially distribution (after Bimha (1996); Rezasefat et al. (2019); Mehreganian et al. (2019a), vertical axis is the pressure); (c) Gaussian distribution (after Pannell et al. (2021), vertical axis is the specific impulse); (d) Rectangular distribution (after Lee and Wierzbicki (2005a); Wierzbicki and Nurick (1996)); (e) Uniform distribution (after Teeling-Smith and Nurick (1991a); Mostofi et al. (2016))

3.6.2 Impulse Enhancement Factor

In order to explore the dependence of the failure behaviour on the shape and magnitude of the blast loading, thereby generalizing the predictive approach, the impulse enhancement factor which was firstly introduced by Tyas and Pope (2003) was employed. It is effectively a measure of the uniformity of the distributed load which allows the comparison of loading with different spatial profiles.

$$I_k = KI \tag{3.35}$$

Before introducing the impulse enhancement factor, three basic assumptions were made:

- A plate behaves as a series of discrete masses
- Each mass is free to move independently of its neighbour
- Each mass is joined to its neighbour by a spring element, which has an arbitrary resistance to shear deformation

Consider a plate subjected to impulsive loading, the entire energy of system at $t = 0$ is kinetic energy E_k with no work done and zero initial internal energy. The kinetic energy of a plate under uniformly distributed impulsive loading can be expressed as given in Eq.(3.36)

$$E_k = \frac{I^2}{2\rho h A} \tag{3.36}$$

where I is the total impulse: the specific impulse, i, integrated over the area of the plate, A.

When under a non-uniform impulse distribution, as shown in Figure 3.8a, the kinetic energy uptake of a plate is dependent on the shear resistance of the connecting spring elements which accounts for different deformation profiles of the plate. The plate would move as a rigid body if infinite shear resistance is assumed among each element while the velocity profile of the plate would be proportional to the initial impulse distribution if zero shear resistance is assumed. The lower bound kinetic energy uptake of the plate corresponding to the infinite shear resistance is defined as:

$$E_{k,l} = \frac{(\int_A i dA)^2}{2\rho h A} \tag{3.37}$$

While the upper bound kinetic energy uptake of the plate corresponding to the zero shear resistance is defined as:

$$E_{k,u} = \frac{\int_A \frac{(i dA)^2}{dA}}{2\rho h} \tag{3.38}$$

Here, energy equivalent impulse I_{EK} is defined as a fictitious uniform impulse load that, if applied to a plate, would result in the same energy uptake as the upper bound kinetic energy uptake of the distributed specific impulse load.

The impulse enhancement factor K is defined as the square root of the ratio of the upper and lower bound kinetic energy

$$K = \frac{I_{EK}}{I} = \sqrt{\frac{E_{k,u}}{E_{k,l}}} \tag{3.39}$$

For example, for an uniform distributed load, K is equal to 1 while for a non-uniform distributed load, K is large than 1. And the applicability of the impulse enhancement factor is checked in the next chapter by combing it with the analytical method developed in this chapter.

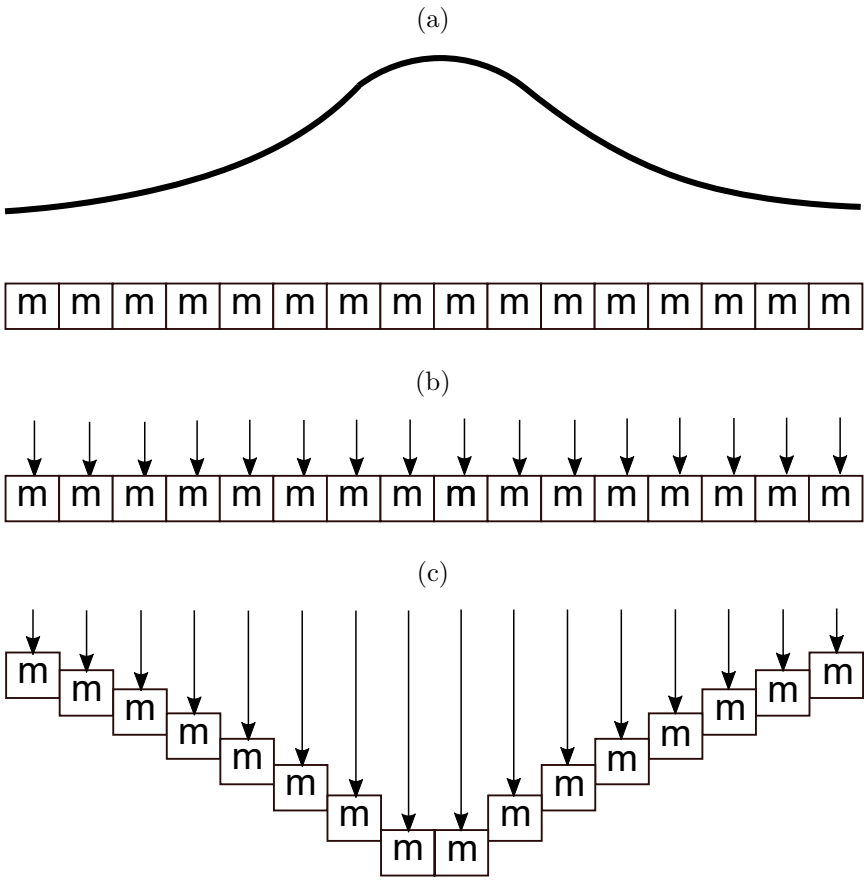

Figure 3.8: Initial deformation modes associated with lower bound (b) and upper bound (c) energy take up (arbitrary element size), based on an initial distribution of specific impulse (a), after Tyas and Pope (2003)

3.7 Summary

This chapter has focussed on the development of analytical solution for predicting response of fully clamped plates subjected to impulsive loadings. Current study deals with the Mindlin plate which allows for effects of transverse shear deformation and rotary inertia. Original governing equations describing the problem investigated are converted to ordinary differential equations along specific directions using characteristic method. Finite difference scheme is later used to replace the derivate with finite difference. This approximation allows the original partial differential equations solvable and variables of interest at any location at any time predicable. Procedures for numerical integration along the characteristic lines are established and the propagation of the discontinuity in moment and shear, as governed by these equations, is discussed.

Most commonly used distributions of blast loading in the literature are summarized and impulse enhancement factor is introduced to generalize the predictive method. Worked example and detailed parametric study using this method can be found in next two chapters.

Chapter 4

Verification of Analytical Method

FOR the aim of accreditation of the analytical method developed in the previous chapter, a preliminary experimental validation and the numerical verification through LS-DYNA are adopted. The spatial distribution generated by small-scale trials from the literature is the first form of blast loading that investigated in this thesis, and serve as the input loading distribution for the verification of the analytical method. The predictive data are in reasonable agreement with test data. Secondly, to eliminate the contingency caused by insufficient experimental data, predicted results are compared with the simulation data to further verify the validity of the analytical method. It has been shown that good agreement between the results of analytical and numerical simulation was obtained.

4.1 Introduction

It has been documented that the finite element method (FEM) was abundantly employed to investigate and to conduct an analysis of the wide variety structures and systems subjected to the both static and dynamic loadings. Some studies used the commercial FEM package, such as the LS-DYNA to analyse the structural response subjected to the blast, and the impact loadings.

It is the purpose of this chapter to verify the accuracy of the analytical method developed in the above section, the dynamic analysis of the brittle plate under impulsive loadings,

which included the time dependent stress, was performed numerically by using FEM explicit solver LS-DYNA . For this aim, the guidelines given in were applied (Zakrisson 2013; Minh Thanh et al. 2016; Shokrieh and Karamnejad 2014; Gao et al. 2018). This chapter presents a two-stage verification for the accuracy of the proposed predictive method when predicting the plate failure behaviour arsing from the impulsive loading:

- A preliminary experimental validation of the quality of the predictive method by comparing the calculated results against the experimental observations from the literature (Colton 1974)
- A more detailed numerical verification between the calculated results and the simulation outputs obtained from LS-DYNA

Whilst it appears that the higher resolution scheme offer the more accurate representations of the structural response, its computational time may increase substantially. The lower resolution scheme may have no computational expense concern, its associated accuracy may be significantly reduced. Hence, in order to determine the optimized mesh size to achieve convergence, a mesh sensitivity study was conducted in this chapter when performing numerical analysis using LS-DYNA.

4.2 Preliminary Validation

4.2.1 Geometry, Material Properties and Set-up of Tests

In this study, to examine the credibility of the analytical method developed in the previous chapter, a comparison was made between analytical predictions and observed experiment results from Colton (1974). The experiments involved thick circular plates of radius 120 mm leaving 108 mm unsupported radius and thickness 6.35 mm, fully clamped around the boundaries. Tested plates were made of two kinds of brittle materials[i]

[i] A brittle material is a material that exhibits little or no plastic deformation before it fractures or breaks when subjected to stress. In other words, brittle materials tend to fail suddenly and catastrophically without any warning signs, unlike ductile materials, which deform plastically before they fail.

linen phenolic (LN) and polymethylmethylmethacrylate (PMMA). Both materials are brittle to fracture at high strain rates and Table 4.1 gives the material properties of LN and PMMA adopted in this study. Material properties were defined based on the study by Babcock et al. (1967), who investigated the uniaxial stress response of LN and PMMA under various strain rates. At high strain rates with temperature at $20°C$ and atmospheric pressure ($P = 101kPa$), both materials exhibited little or no plastic deformation before fracturing, making them brittle when subjected to blast loading. Additionally, PMMA is a transparent material which allows the fracture process to be observed from both the loaded and back faces. The critical input parameters, such as material properties (E, G, ρ, θ_f, and ν as shown in the Table 4.1) and plate geometry (r, h), have been normalized using dimensionless quantities introduced in Eq.3.13. The mathematical relationships among these dimensionless quantities and their quantitative effects on the internal stress resultants, such as $\overline{M}$, $\overline{W}$, $\overline{Q}$, $\overline{N}$, and $\overline{V}$, will be demonstrated in Section 3.4.

Impulsive blast loadings were applied by sheet explosive placed over a neoprene foam attenuator in contact with the target plate and all explosive patterns were 5.08 cm in diameter. Figure 4.1 gives the illustration of explosive loading configuration. The impulse intensity produced by the explosive sheet depends on the thickness of the explosive sheet where the impulse intensity per thickness is constant for the configuration used in the experiment. Hence, varying the thickness h will lead to different loading distribution that applied on the target plate.

The response of the plate under the blast loading such as deformation and cracking sequence was recorded by a high-speed (200000 frame/sec) framing camera, and the strain history at specific locations were measured by the strain gauges. These observed responses show that bending is the mechanism that produces the final fracture pattern and latter served as a baseline against which theoretical predictions can be compared.

Whilst explosive sheets have been widely used in small-scale blast tests and the loads they transmitted on targets are well understood by researchers, deriving an accurate spatial distribution function of pressure due to a proximal blast over a plate is still difficult. Therefore, assumptions have to be made to obtain a load distribution function before it is used in the analyses:

- A typical pressure-time profile which is a sudden rise to a peak pressure followed by an exponential decay was assumed. It is the temporal variation form of the blast that applied on the front surface of the target plate.

- For the configuration used in the study, e.g., a explosive sheet with thickness of 0.38 mm produces the peak pressure of 100 MPa resulting in a characteristic exponential decay time of 5 μs. This decay time is comparable to the time that dilatational waves traverse the plate thickness twice. Therefore, it is reasonable to assume that the impulsive loading can be ideally characterized by the distribution of the initial velocity.

Material	$\boldsymbol{E}$ $\boldsymbol{(GPa)}$	$\boldsymbol{G}$ $\boldsymbol{(GPa)}$	$\boldsymbol{\rho}$ $\boldsymbol{(kg/m^3)}$	**Fracture stress,** $\boldsymbol{\sigma_f(MPa)}$	**Poison Ratio,** $\boldsymbol{\nu}$
LN	6.83	2.73	1350	78	0.25
PMMA	4.78	1.91	1180	84	0.25

Table 4.1: Material properties of LN and PMMA according to Babcock et al. (1967)

In the present experiment the explosive pressure produced by the loading configuration is assumed to be an initial velocity with bi-linear distribution shown in Figure 4.2. This loading model has a constant velocity value V acting over a certain radius R and then followed by a linearly decaying velocity distribution on the remainder of the structure along the radial direction:

$$V(r) = \begin{cases} V, & 0 \leq r \leq R - \frac{d_t}{2} \\ -\frac{V}{d_t} r + \frac{V(2R+d_t)}{2d_t}, & R - \frac{d_t}{2} \leq r \leq R + \frac{d_t}{2} \end{cases} \tag{4.1}$$

where $V(r)$ is the spatial variation of velocity in the radial direction, r is the radial coordinate and d_t is the taper length of the load on the plate which is influenced by the size of the explosive and its stand-off from the target.

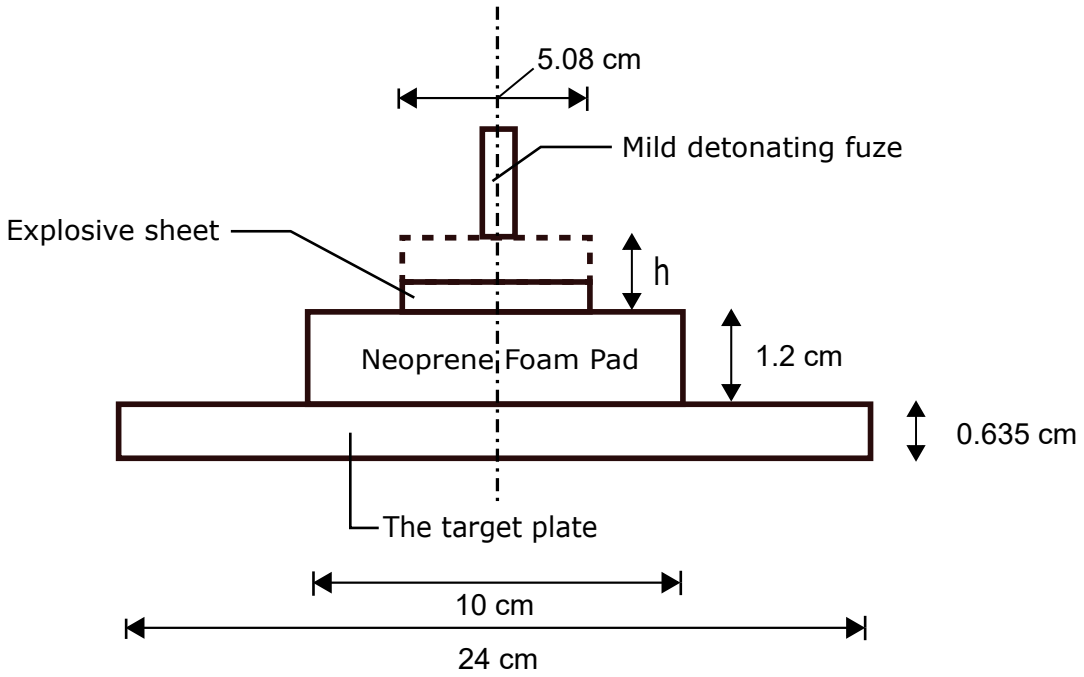

Figure 4.1: Schematic of test plate and explosive

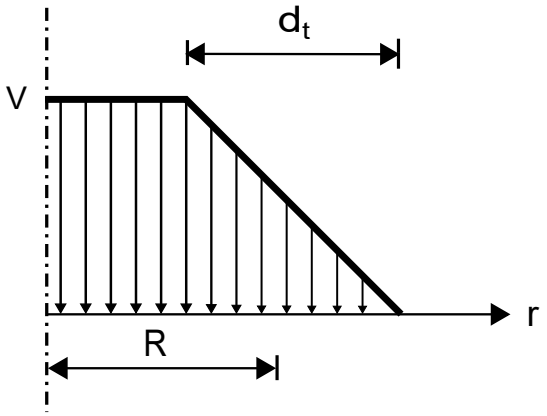

Figure 4.2: A bi-linear loading spatial distribution

4.2.2 Evaluation against Experimental Results

Predicted bending moments from the analytical solution for the brittle plates subjected to impulsive loadings are shown in the Figure 4.3 and Figure 4.4. It should be noted that for the purpose of comparison, the magnitude of the applied blast loading used in the analytical prediction is consistent with those applied in the experiments. While the impulse enhancement factor K is the same for both plates since the same bi-linear distribution of blast loading is adopted. The fracture criterion used in the analysis is that of maximum normal stress. Hence, brittle fracture under tensile stresses due to bending occurs whenever the principal stress reaches σ_f, the fracture stress in uniaxial loading which is available in Table 4.1. In terms of stress resultants, the maximum normal stress criterion for brittle fracture is

$$|M| = |N| = \frac{h^2 \sigma_f}{6} \tag{4.2}$$

Then the normalized fracture criterion is equal to $\overline{M} = \nu\overline{N} = 0.0329$. For fracture under a combined stress where both principal stresses are tensile, as will be shown is the case here, the maximum normal stress criterion is equivalent to the Tresca yield condition [ii] for ductile material.

For LN and PMMA plates subjected to a bi-linear blast loading as shown in Figure 4.2 the corresponding values for K and I could be calculated by using the Matlab script given in the Appendix A.2. Material properties obtained from Table 4.1 are used as input parameters.

For the finite difference solution introduced in Section 3.4, its accuracy depends on the order of the mesh size used. A sensitivity analysis was performed to determine the practical time spacing Δt with reasonable accuracy. One set of experimental results is used as the reference which is the fracture response, such as failure mode and fracture location at $t = 15\ \mu s$ of a PMMA plate subjected to a blast load with $I = 1.44 Ns$ and $K = 3.76$. Analysis results were given in the Appendix B.1. It could be seen that, as the

[ii] According to the Tresca yield criterion (Tresca 1878), yielding will occur in a material when the maximum shear stress on any plane within the material reaches a critical value known as the yield strength (also called the shear strength). The yield strength is assumed to be the same in tension and compression, and is often determined experimentally using uniaxial tensile or compression tests.

time spacing decreases, the normalized bending moment in two peaks increases. However, based on experimental results, circumferential fractures were not observed in predicted results until Δt decreased to 0.2 μs. Hence, a time spacing of $\Delta t = 0.2$ μs was used in the analysis. Otherwise, the failure mode would be significantly different, leading to a large error in predicting the failure response of the target plate by using dimensionless $I - K$ diagrams, which will be discussed later.

For the LN plate, it can be seen that by 4 μs the bending moment distribution which is initially zero, has developed both positive and negative peaks. The locations of these peaks correspond to the discontinuities in slope of the initial velocity distribution. Later on, these two peaks grow in amplitude and move away from each other, The inner peak moves to the centre of the load and combines with its symmetric counterpart to produce a significant increase in amplitude which reaches the critical stress. The outer peak and its symmetric counterpart move outward, however, do not attain the magnitude of the coalesced peak at the load centre.

At $t = 24$ μs, the bending moments in both radial and tangential directions at the origin reach a value of $\overline{M} = \nu\overline{N} = 0.033$ which exceeds the fracture stress of linen phenolic. Therefore, a series of radial fractures emanating from the origin at the back surface of the plate is predicted, as indicated in Figure 4.3d.

For the PMMA plate, the distribution of developed bending moments are similar in the shape shortly after loading applied but have greater amplitude that those for the LN plate. As indicated in Figure 4.4c, the initial inner and outer peaks in bending moment are sufficient to cause fracture before the inner peaks converge at the origin. As a result, two circumferential fractures are predicted at $t = 15$ μs at both loaded and back face of the plate. Then it can be seen that at $t = 20$ μs at $\xi = 7.1$, the tangential bending moment reaches the fracture stress $\overline{N} = 0.033$ so that a series of radial fractures initiated from the back surface of the plate is predicted.

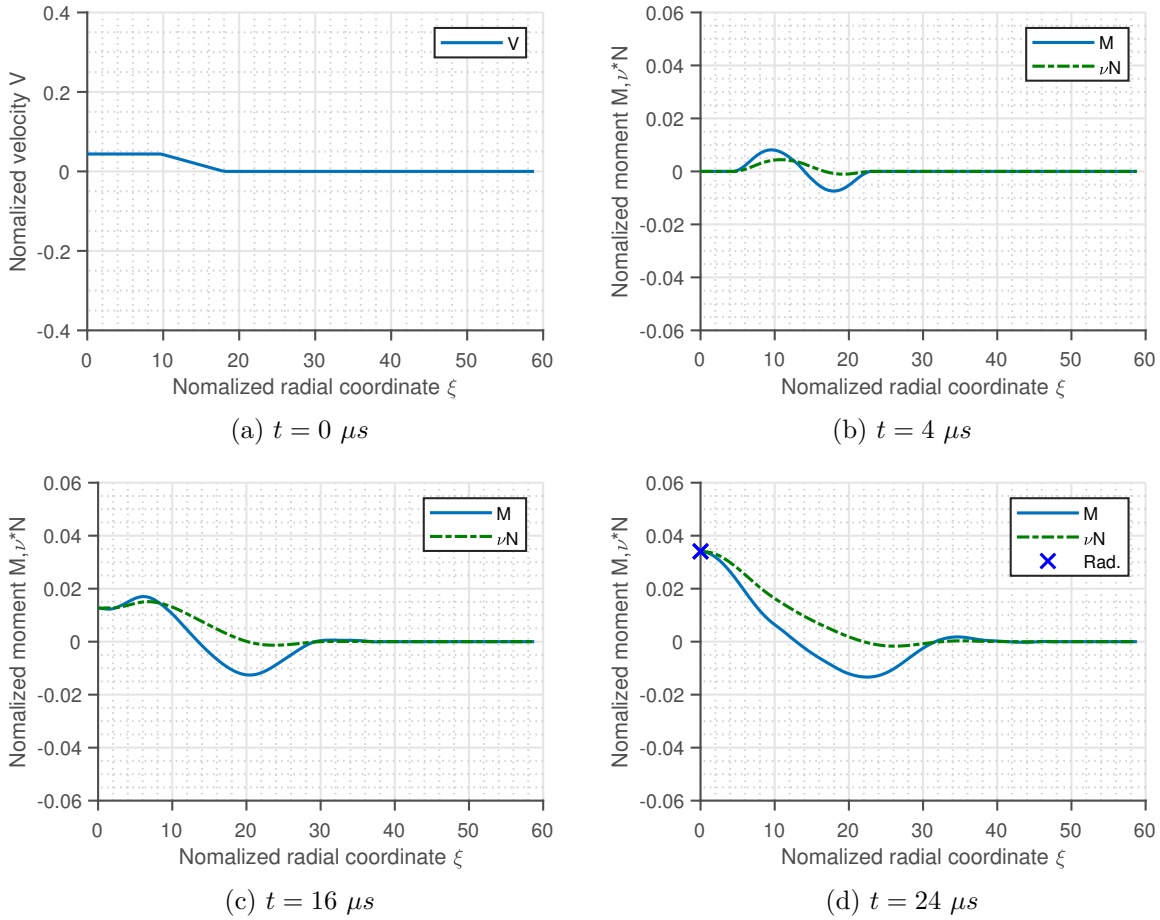

(a) $t = 0\ \mu s$ (b) $t = 4\ \mu s$

(c) $t = 16\ \mu s$ (d) $t = 24\ \mu s$

Figure 4.3: Calculated bending distribution for a LN plate under a bi-linearly initial velocity distribution with $I = 0.94\ Ns$ and $K = 3.76$, "Rad." denotes the radial fracture: (a) $t = 0\ \mu s$, the initial velocity profile; (b) $t = 4\ \mu s$, positive and negative peaks develops corresponding to the discontinuity in slope of the initial velocity distribution; (c) $t = 16\ \mu s$; (d) $t = 24\ \mu s$, radial fracture initiates from the origin at the back face of the plate due to the normalized stress in both radial and tangential directions a the origin exceed the material strength

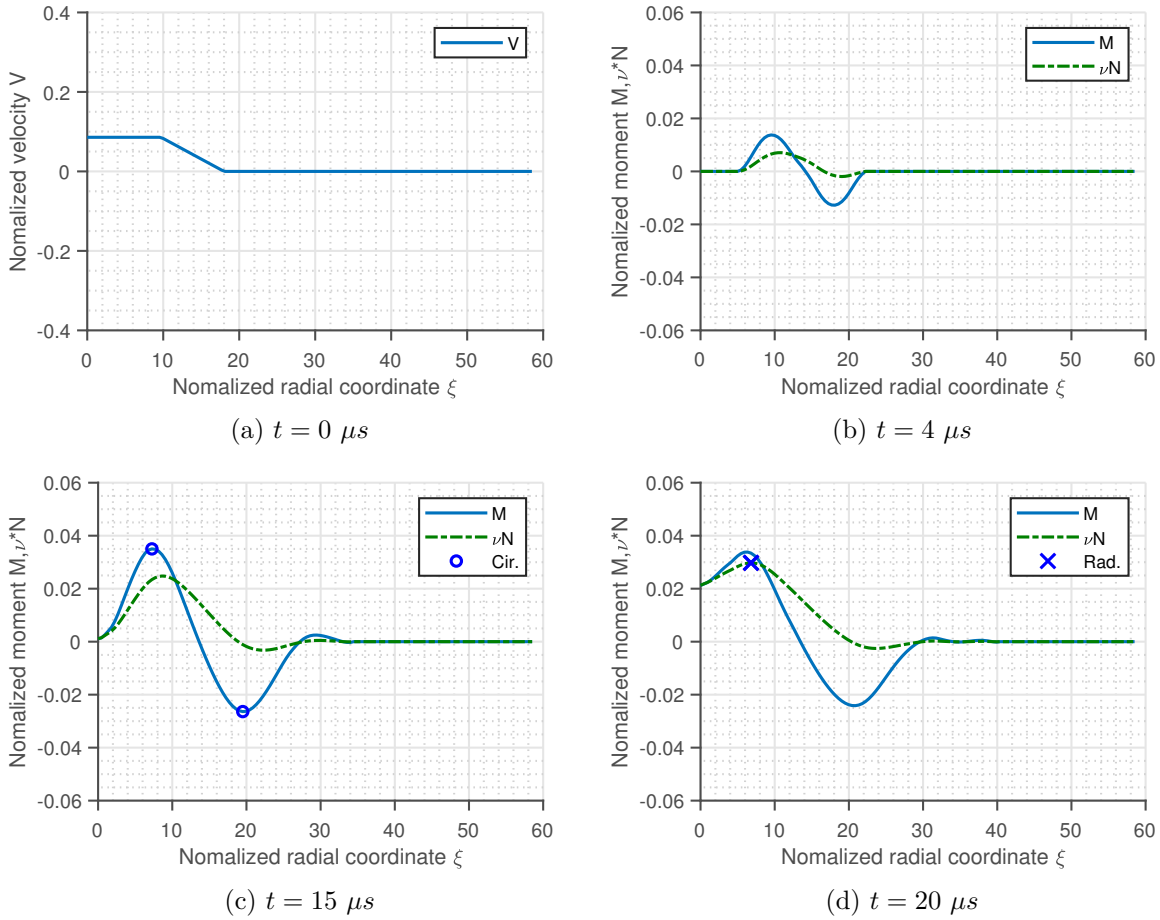

(a) $t = 0\ \mu s$ (b) $t = 4\ \mu s$

(c) $t = 15\ \mu s$ (d) $t = 20\ \mu s$

Figure 4.4: Calculated bending distribution for a PMMA plate under a bi-linearly initial velocity distribution with $I = 1.44\ Ns$ and $K = 3.76$, "Cir." denotes the circumferential fracture: (a) $t = 0\ \mu s$, the initial velocity profile; (b) $t = 4\ \mu s$, positive and negative peaks develops corresponding to the discontinuity in slope of the initial velocity distribution; (c) $t = 15\ \mu s$, two circumferential fractures appear with one at the loaded face and the other at the back face of the plate; (d) $t = 20\ \mu s$, radial fractures initiate at some distance away from the origin because the tangential bending moment reaches the fracture stress

Experimental and predicted fracture behaviours were summarized in Table 4.2. It can be seen that, these predictions agree well with the experimental observations which are all within 6%. In all instances, both fracture location and fracture time as well as fracture modes are predicted which demonstrates the ability of the analytical method to predicting the failure response of the brittle plates subjected to blast loadings.

Material	K	$I(Ns)$	**Fracture time (μs)**			**Fracture location (cm)**			**Fracture**
			Pred.	**Exp.**	**% diff.**	**Pred.**	**Exp.**	**% diff.**	
			15	15	0	+1.33[a]	+1.27	5	cir.
PMMA	3.76	1.44	15	15	0	−3.57[b]	−3.81	6	cir.
			20	20	0	+1.33	+1.27	5	radial
LN	3.76	0.94	24	24	0	0[c]	0	0	radial

[a] Positive values mean distance from the centre at the back face of the plate
[b] Negative values mean distance from the centre at the loaded face of the plate
[c] At the origin

Table 4.2: Failure results from experiments and analysis

4.3 Numerical Study Using LS-DYNA

4.3.1 Modelling Considerations

Experimental work of Rigby et al. (2019b) demonstrated that the initial velocity uptake of a plate is directly proportional to the distributed specific impulse. The suddenly applied pressure is imparted to the plate as an initial velocity which is related to the specific impulse by the momentum conservation equation

$$i(r) = \rho t v(r) \tag{4.3}$$

where ρ is the material density, t is the thickness of plates and $v(r)$ is the initial velocity distribution.

Finally, the distribution of initial velocity resulting from impulsive loading was derived which would be applied on the every node of target directly using a Matlab script. The validity and accuracy of this technique has been demonstrated clearly according to Rigby et al. (2019b) and will be adopted in the current study.

The plates were modelled using the $*MAT\_PLASTIC\_KINEMATIC$ [iii]. Since the investigation only focus on the failure response of brittle plates, no plastic strain were allowed when adopting this kind of material model. A quarter of the plate was modelled to shorten the simulation time due to the symmetric nature of the problem. Any nodes with radial ordinate ≥ 108 mm were constrained against all translations and rotations to match the experimental support conditions. Nodes along the symmetry planes were constrained appropriately. Figure 4.5 gives the 3D quarter-symmetry model of the plate.

[iii] In LS-DYNA, the "plastic kinematic" material keyword is used to define a material model for solid elements that exhibits both plasticity and kinematic hardening; The plastic kinematic material model assumes that the plastic deformation is the result of the combination of a kinematic hardening component and an isotropic hardening component. The kinematic hardening component describes the additional resistance to deformation due to the back-stress, while the isotropic hardening component describes the additional resistance to deformation due to the accumulation of plastic strain.

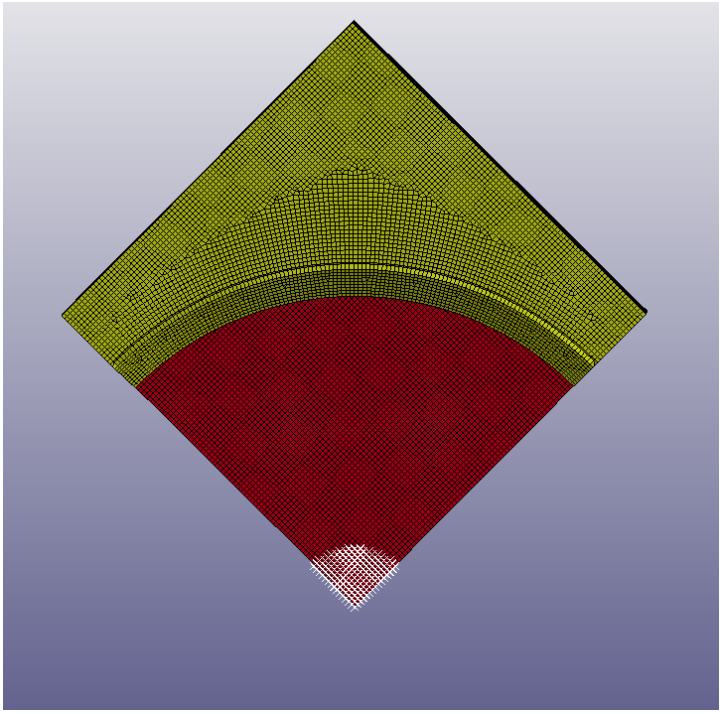

Figure 4.5: Quarter-symmetric representation of the plate model (note: applied blast load is shown in the white area)

4.3.2 Convergence Study

In this study, solid elements were adopted for the modelling of plates in LS-DYNA. A mesh sensitivity study was conducted which was aimed at determining the required element size to achieve convergence. In the developed FE model, a preliminary convergence study was carried out by varying the mesh size along the length and width directions. It was found that the stress time history varies negligibly as element size is any smaller than 2 mm. Further reducing mesh size only has insignificant influence on numerical results but leads to a substantial increase in computational time. Hence, the meshing strategy is to vary the mesh size through the thickness of the plate while mesh size along the radial direction were fixed as $2mm$.

The plate were divided through the thickness ranging from 1 layer to 15 layers. Figure 4.6 shows the fracture time against mesh size. The results suggest that fracture behaviour could be predicted with good accuracy when the plate is divided into 5 layers through its thickness. This fact is further supported as indicated in Figure 4.7 where further

reducing the mesh size could not contribute significantly to the accuracy of predicting the stress time history. It is worth mentioning that the theoretical curve initiates a small distance away from the origin. This 'delay' results from the larger mesh size employed in the theoretical solution (time spacing $\Delta t = 0.2\ \mu s$), which leads to sparse data points compared to the much larger number of data points in the numerical results. Hence, numerical curves 'climb' much faster than the theoretical curve

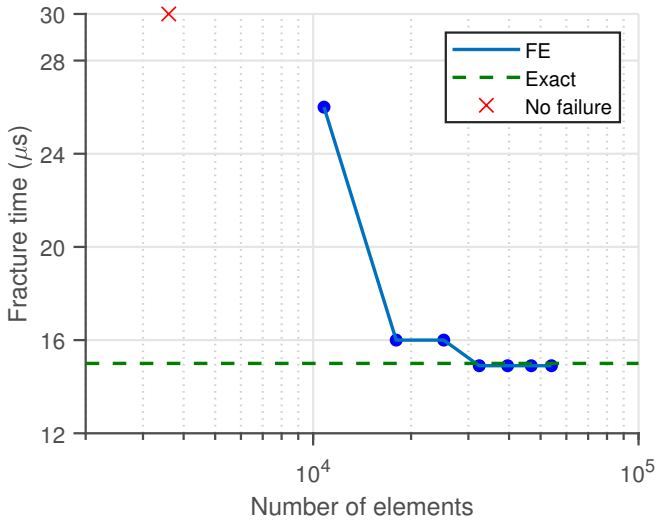

Figure 4.6: Fracture time for different mesh densities at $r = 3\ cm$ from the centre on the loaded face of a PMMA plate ($K = 3.76$)

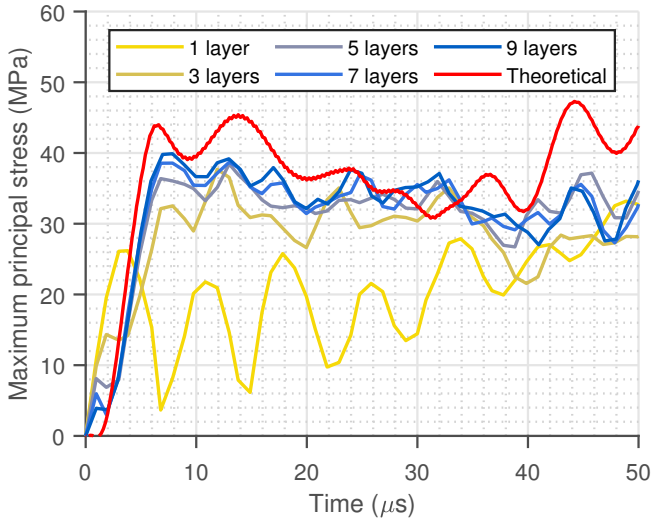

Figure 4.7: Stress time histories for different divisions of plate thickness, a circular plate with thickness equals to $6.35mm$ and subjected to blast loads with $I = 1.44Ns$ and $K = 3.76$

4.4 Numerical Evaluation of the Results

4.4.1 Comparison of Stress Time History

In order to demonstrate the accuracy of the derived analytical method, six verification examples were performed using the following inputs:

i $r = 3\ cm, I = 0.94\ Ns$ for a LN plate

ii $r = 3\ cm, I = 1.44\ Ns$ for a PMMA plate

iii $r = 4\ cm, I = 0.94\ Ns$ for a LN plate

iv $r = 4\ cm, I = 1.44\ Ns$ for a PMMA plate

v $r = 4.5\ cm, I = 0.94\ Ns$ for a LN plate

vi $r = 4.5\ cm, I = 1.44\ Ns$ for a PMMA plate

In all examples, impulse enhancement factor K and loading distribution were set as 3.76 (both K and I are calculated from the Matlab script given in Appendix A.2) and bi-linear respectively. All plates were 120 mm in radius and 6.35 mm in thickness with fully clamped along edges.

Figure 4.8 compares the analytical and numerical stress time-histories of the plate at various radial coordinates for loading intensity of 0.94 Ns and 1.44 Ns. To decrease the computational time in simulation, the time chosen in the analysis ends at $t = 50\ \mu s$. It is shown that the analytical results compare well with that obtained from the numerical analysis for different loading magnitude and locations. This certified the validity of the current approach, thus, the presented method can be reliably used for the practical applications and prediction of the failure response of the blast loaded plates.

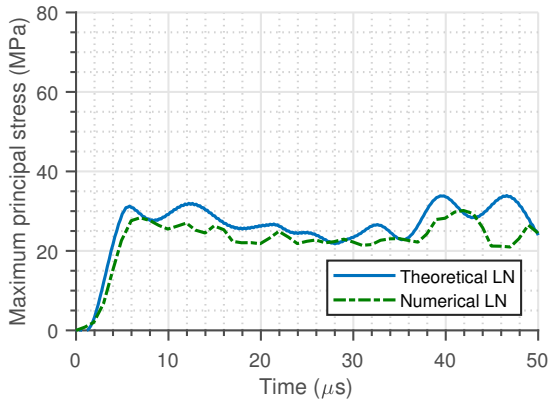

(a) $r = 3\ cm, I = 0.94\ Ns$

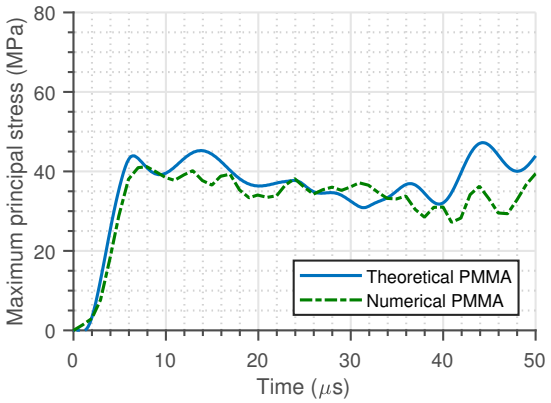

(b) $r = 3\ cm, I = 1.44\ Ns$

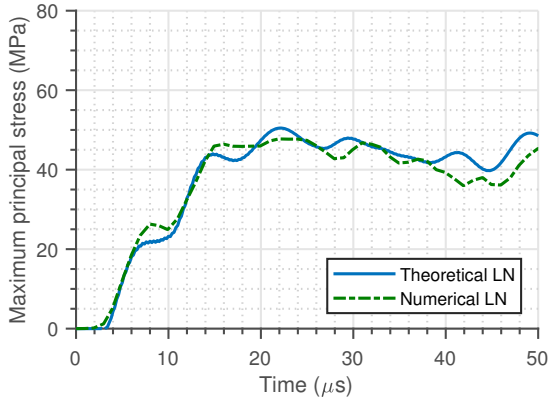

(c) $r = 4\ cm, I = 0.94\ Ns$

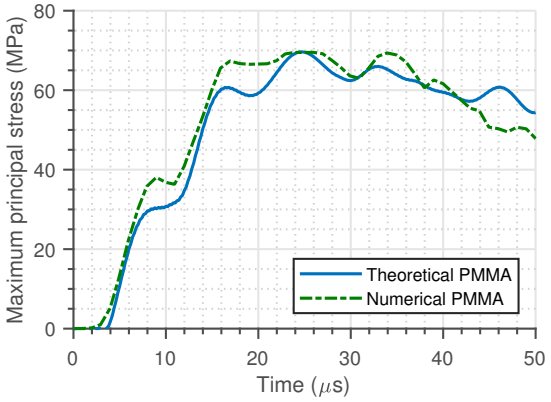

(d) $r = 4\ cm, I = 1.44\ Ns$

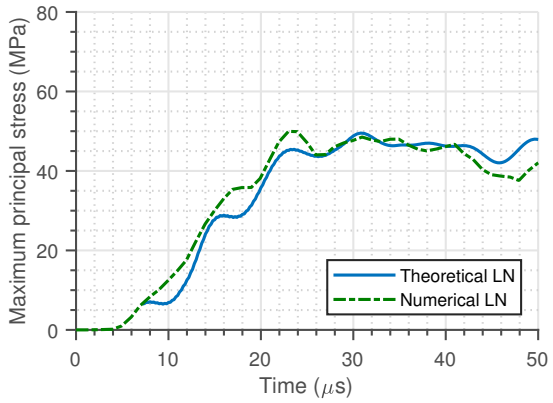

(e) $r = 4.5\ cm, I = 0.94\ Ns$

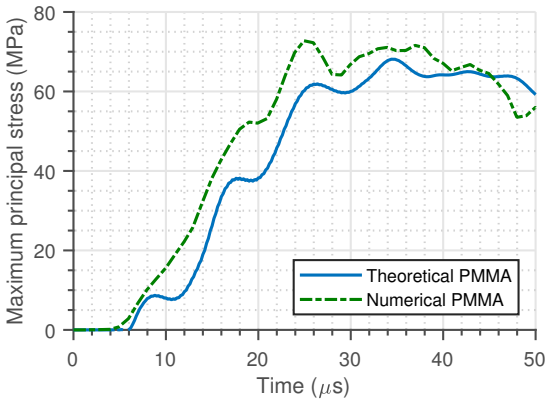

(f) $r = 4.5\ cm, I = 1.44\ Ns$

Figure 4.8: Theoretical and numerical stress-time histories on the loaded face of LN and PMMA plates under blast loadings ($K = 3.76$)

4.4.2 Comparison of Fracture Time and Fracture Location

Figure 4.9 shows a comparison between the numerical results and analytical predictions using the method for the PMMA plate example, evaluated on the impulse enhancement factor of 3.76. It can be seen that, a high level of qualitative agreement is attained, which demonstrates the suitability of the method detailed herein for predicting the failure response.

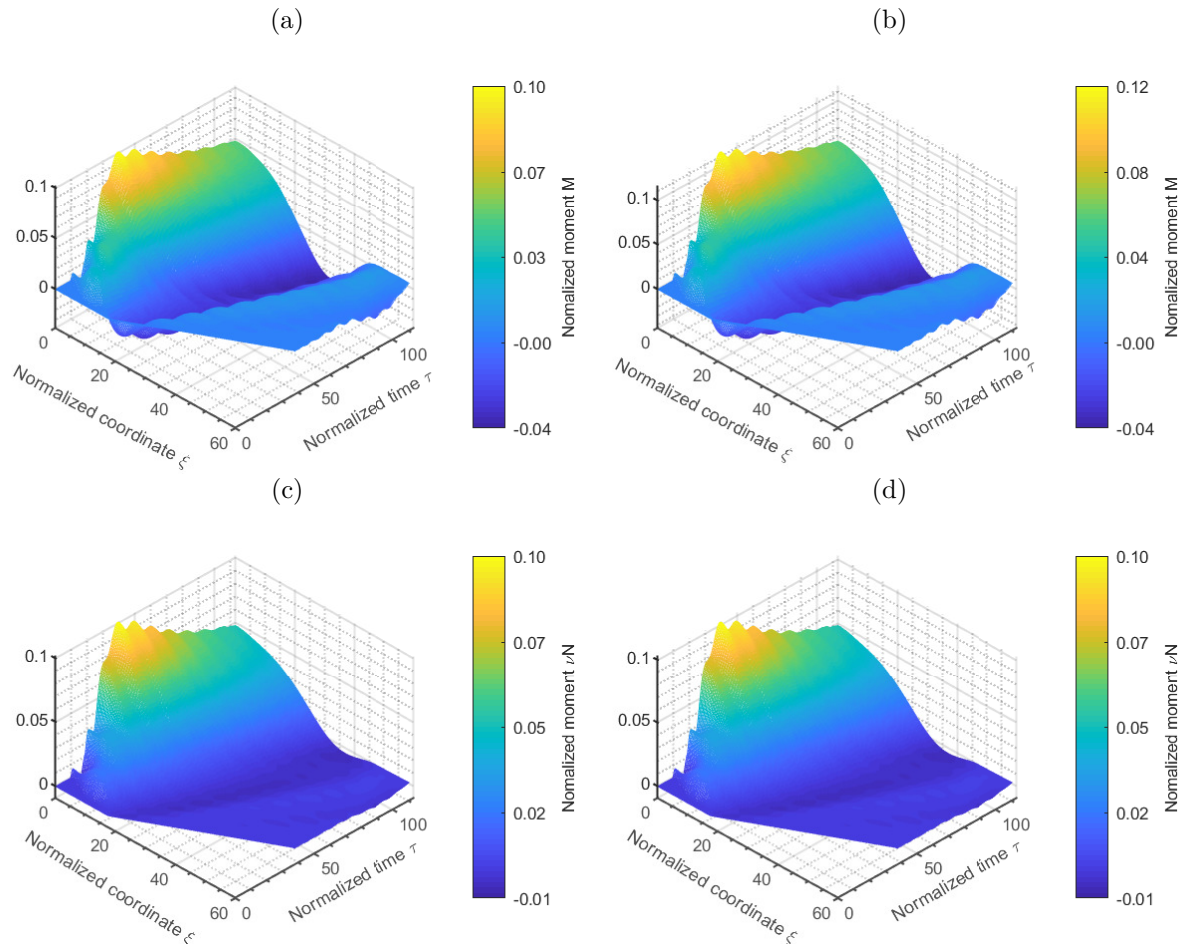

Figure 4.9: Radial and circumferential bending moment distribution in the $\xi - \tau$ plane for PMMA plate under $K = 3.76$ and $I = 1.65$: (a) numerical radial bending moment (b) predicted radial bending moment (c) numerical circumferential bending moment (d) predicted circumferential bending moment

A direct comparison of predicted and numerical results is provided in Table 4.3. It can be seen that, the predictions are all within 2% of the predicted fracture time, fracture location and fracture mode. Both circumferential and radial fracture occurred at different time were predicted with good accuracy. Prediction of failure response of brittle plates subjected to different combination of K and I with different loading shapes will be investigated in the next chapter though a parametric study.

Material	K	$I(Ns)$	Fracture time (μs)				Fracture location (cm)				Fracture
			Pred.	DYNA	Exp.	% diff. [a]	Pred.	DYNA	Exp.	% diff.	
			15	15	15	0	+1.33[b]	+1.31	+1.27	2	cir.
PMMA	3.76	1.44	15	15	15	0	−3.57[c]	−3.62	−3.81	1.4	cir.
			20	20	20	0	+1.33	+1.31	+1.27	1.5	radial
LN	3.76	0.94	24	24	24	0	0[d]	0	0	0	radial

[a] Difference between predicted and LS-DYNA results
[b] Positive values mean distance from the centre at the back face of the plate
[c] Negative values mean distance from the centre at the loaded face of the plate
[d] At the origin

Table 4.3: Failure results from experiments and analysis

4.5 Summary

In this chapter, the accreditation of the proposed analytical method was examined in terms of the fracture time, fracture location as well as stress time history. Predicted failure responses of LN and PMMA plates were firstly validated in comparison with experimental observations. It was found that the failure behaviours of LN and PMMA plates were reproduced successfully with all within 6% variation between the proposed method and the experiments.

Prior to a further verification of the credibility of the analytical method, a convergence study was performed. It was found that division of 5 layers through thickness resulted in acceptable prediction accuracy of failure time as well as achieving the purpose of predicting the stress time history.

The small variation between calculated stress time history using the presented method and numerical analysis through LS-DYNA proved the reliability and validity of the presented analytical method for blast loaded plates.

Following on from this, radial and circumferential bending moment distribution in the $\xi - \tau$ plane obtained from LS-DYNA model and predictive method were compared. The result shows that a high level of qualitative agreement is attained, which further demonstrates the validity of the method.

Chapter 5

Failure Response of Impulsively Loaded Plates

THIS chapter contains the results and and discussion from a detailed parametric study aimed at investigating the dependence of the failure response on the distribution and intensity of the applied blast loading. The response of brittle plates subjected to blast loads will be evaluated for 5 most widely used loading distributions in an attempt to understand and quantify the influence of load magnitude and shape; and also to develop and provide detailed failure response predictions and dimensionless $I - K$ diagrams on the likely failure modes a target plate will sustain for a blast load with given distribution and intensity.

5.1 Introduction

Proximal blasts cause particular threats to both human life and civil and military infrastructure. The source of such blasts can be, for example, IEDs (improvised explosive devices) and buried land mines exploding onto the underside of military vehicles. When blasts occur in close proximity to engineering structures, the localised effect of the load causes particular forms of damage to the structure and thus require particular consideration which is different from the case of global (or uniform) blast loading.

Results in section 2.2.2 have shown that the loading distribution and intensity have a significant effect on the failure behaviour of blast loaded. Previous chapter only shows the results for fully clamped brittle plates under a bi-linear distribution with K is limited to 3.76. However, the value of K corresponding to different distribution of blast loading could be different. In this regard, this chapter investigated the variation of the failure modes of plates for a range of blast loadings.

5.2 Uniform Load Distribution

5.2.1 Failure Modes and Failure Response Prediction

In the parametric study, the plate with same geometry and the boundary condition as that studied in section 4.2.1 was investigated throughout the thesis. The effect of boundary conditions and plate geometry on the response will be discussed in the end of this chapter.

In this chapter, the failure behaviour resulting from an uniform load distribution is the first form of blast loading that investigated. A schematic of an uniform distributed blast load is illustrated in Figure 5.1. In Figure 5.1, R_p represents the radius of the plate.

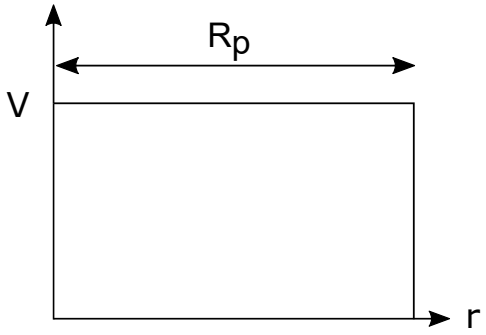

Figure 5.1: Uniformly distributed load distribution

Hence, we have

$$V(r) = V \;\; 0 \leq r \leq R_p \tag{5.1}$$

The results from the parametric study are provided in full in Table 5.1. It can be seen from the table that the K is kept to be 1 as it is an uniform distributed load while varying the magnitude of the load lead to two different kinds of failure modes, classified as Type (a) and Type (b).

Failure initiated at the origin is defined by author as the first failure mode for the plate studied under the uniform load distribution with $K = 1$. With increased intensity of blast loading, circumferential failure is observed at the boundary first and then radial fracture is observed at the origin. Further increases in the blast loading result in the completely tearing of the boundary which occurs so quickly that there is no time for the fracture initiates at the origin. Figure 5.2 shows the propagation of the radial and circumferential crack outward from the origin and boundary, respectively. One should note that the predictive method developed in this thesis could predict the initiation of circumferential fracture pattern by specifying the radius at which the fractures are formed. However, the method could not completely predict the radial fracture because of the full description of the radial fracture needs both the radius and the number of radial fractures while the predictive method in this study could only predict the radius of the radial fractures. Hence, the number of radial fractures shown in the Figure 5.2 is only used for illustration of the fracture process. Detailed discussion of this limitation can be seen in the next chapter.

After examining the time history of both tangential and radial bending moment distributions 2 different failure modes for a brittle plate under an uniform distribution blast loading are as shown in Figure 5.3.

K	$I(Ns)$	Fracture time (μs)	Fracture location	Failure Modes
1	3[a]	364.20	origin	Type (a)
	5	104.94	origin	Type (a)
	5.5	103.18	origin	Type (a)
	5.8	8.00 102.56	boundary origin	Type (b)
	6	6.80 102.56	boundary origin	Type (b)
	7	4.80 101.41	boundary origin	Type (b)
	8	3.60 100.62	boundary origin	Type (b)
	15	2.00	boundary	Type (b)

[a] $I = 3\ Ns$ is the minimum impulse that will causes the fracture.

Table 5.1: Failure response results for uniformly distributed loaded plate

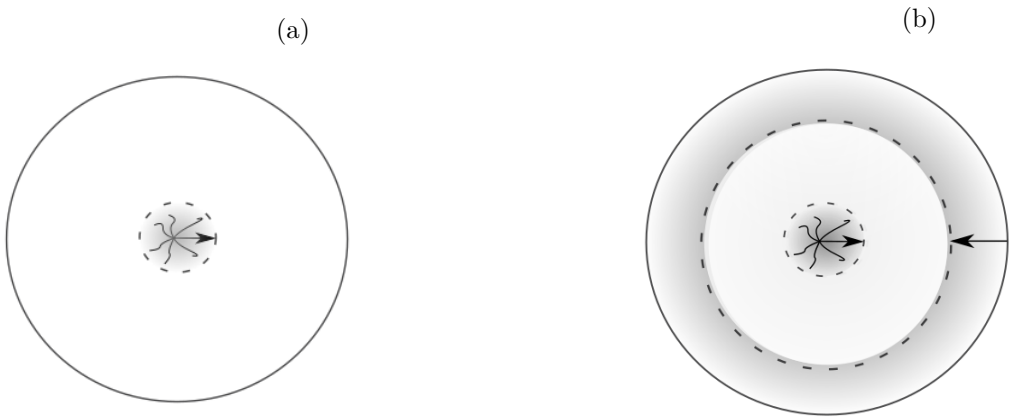

Figure 5.2: Propagation of radial and circumferential crack in the uniformly distributed loaded plate; (a) radial fracture initiated from the centre, (b) circumferential fracture initiated from the boundary and radial fracture initiated from the centre at later times

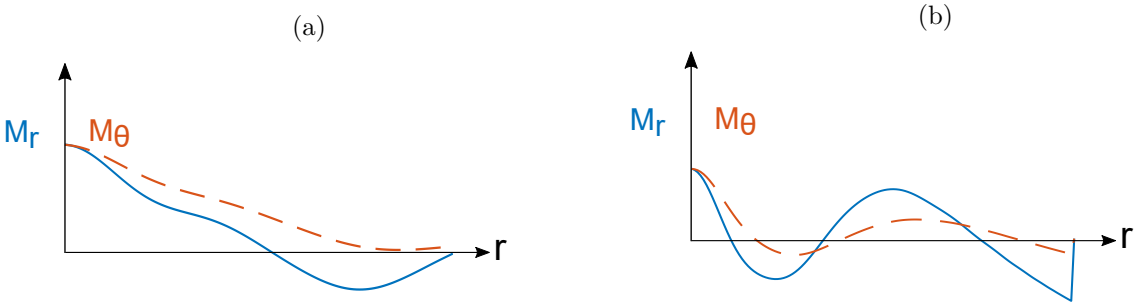

Figure 5.3: Failure modes observed in the uniformly distributed loaded plate, M_r denotes radial bending moment per unit length, M_θ denotes tangential bending moment per unit length

5.3 Bi-linear Load Distribution

5.3.1 Failure Modes

The second blast loading shape that investigated in this chapter is the bi-linear load distribution. The bi-linear blast loading produced by the explosive sheet of diameter D is illustrated in Figure 5.4.

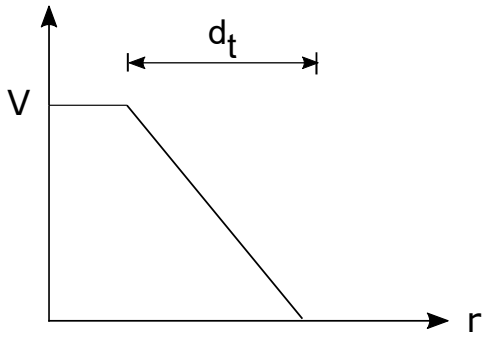

Figure 5.4: Bi-linear load distribution

This loading model has a constant velocity value V acting over a certain radius $R = D/2$ and then followed by a linearly decaying velocity distribution on the remainder of the structure along the radial direction:

$$V(r) = \begin{cases} V, & 0 \leq r \leq R - \frac{d_t}{2} \\ -\frac{V}{d_t} r + \frac{V(2R+d_t)}{2d_t}, & R - \frac{d_t}{2} \leq r \leq R + \frac{d_t}{2} \end{cases} \tag{5.2}$$

where $V(r)$ is the spatial variation of velocity in the radial direction, r is the radial coordinate and d_t is the taper length of the load on the plate which is influenced by the size of the explosive and its stand-off from the target. In this study, we assume the value of d_t is constant so that the number of variables could be decreased and results are consistent with the those obtained in Chapter 4.

After examining the time history of both tangential and radial bending moment distributions 5 different failure modes for a brittle plate under a bi-linear distribution blast

loading are as shown in Figure 5.5, classified as Type (a), Type (b), Type (c), Type (d) and Type (e).

Figure 5.6 shows the propagation of the radial and circumferential crack for various failure modes. It is worthing mentioning that, for the Type (b) failure modes, radial fracture is initiated from the origin and propagates towards the boundary while the circumferential fracture initiated at some radii is propagating inwards. Hence, continue increasing the magnitude will see the smaller radii of the circumferential fracture and longer radial fracture line.

The results from the parametric study are provided in Table 5.2, Table 5.3, Table 5.4 and Table 5.5.

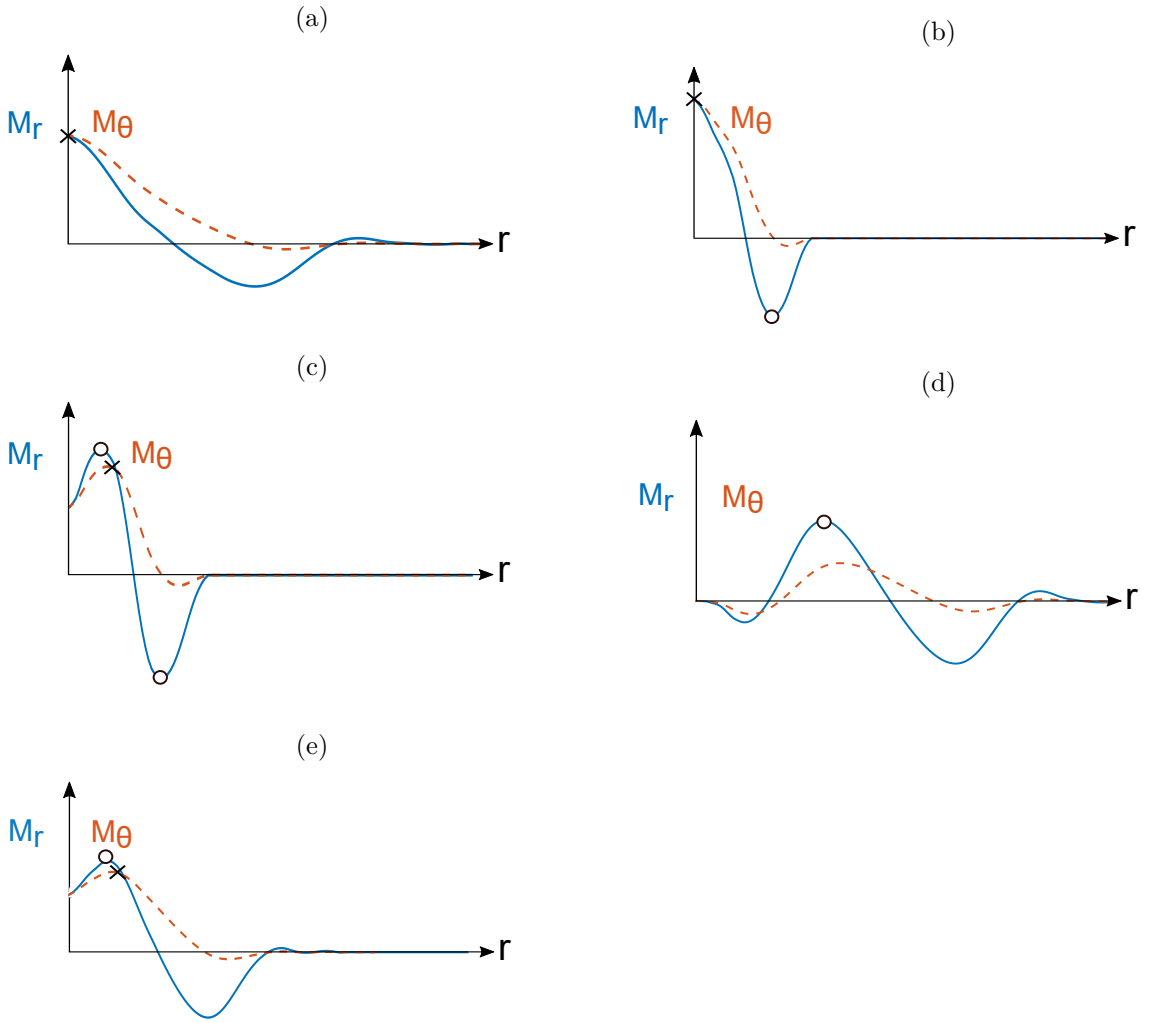

Figure 5.5: Failure modes observed in the bi-linear distributed loaded plate, M_r denotes radial bending moment per unit length, M_θ denotes tangential bending moment per unit length, cro-ss symbol denotes the radial fracture and circle symbol denotes the circumferential fracture: (a) radial fracture initiated from the centre; (b) radial fracture initiated from the centre and circumferential fracture initiated at some distance away from the centre at later times; (c) radial fracture initiated at some distance away from the centre, two circumferential fractures initiated at two different radii; (d) a circumferential fractures initiated at some distance away from the centre; (e) a circumferential fractures initiated at some distance away from the centre and radial fracture initiated at the same radii at the same time

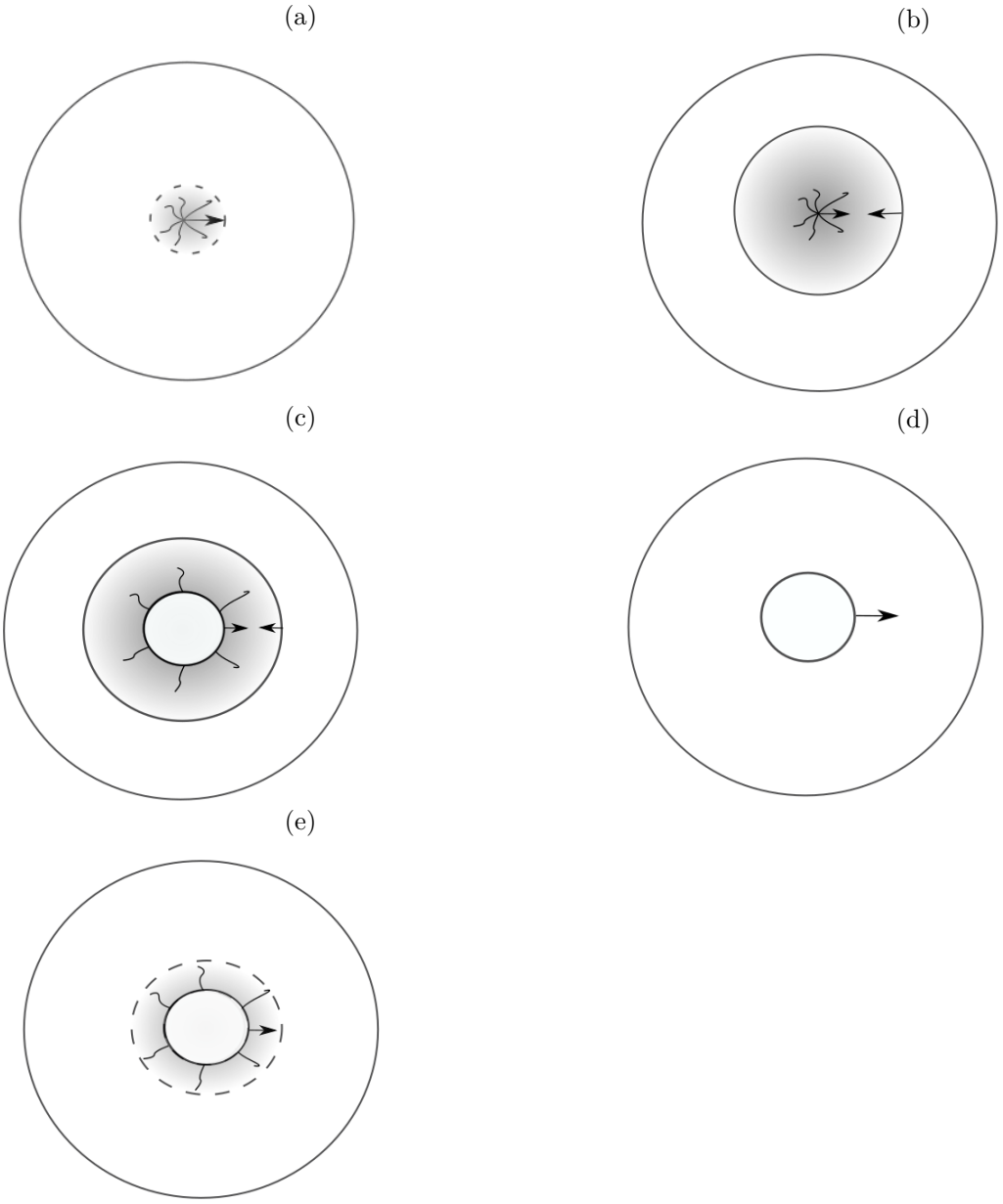

Figure 5.6: Propagation of radial and circumferential crack in the bi-linear distribution loaded plate: (a) radial fracture initiated from the centre; (b) radial fracture initiated from the centre and circumferential fracture initiated at some distance away from the centre at later times; (c) radial fracture initiated at some distance away from the centre, two circumferential fractures initiated at two different radii; (d) a circumferential fractures initiated at some distance away from the centre; (e) a circumferential fractures initiated at some distance away from the centre and radial fracture initiated at the same radii at the same time

K	$I(Ns)$	Failure Modes
2.04	2.06	Type (a)
	2.37	Type (a)
	3.17	Type (a)
	3.96	Type (a)
	4.04	Type (b)
	4.12	Type (b)
	4.75	Type (b)
	5.14	Type (b)
	5.54	Type (b)
	5.94	Type (b)
	6.17	Type (c)
	6.33	Type (c)
	7.12	Type (c)
2.25	1.67	Type (a)
	1.93	Type (a)
	2.57	Type (a)
	3.21	Type (a)
	3.31	Type (b)
	3.34	Type (b)
	3.85	Type (b)
	4.17	Type (b)
	5.01	Type (c)
	5.78	Type (c)
2.51	1.32	Type (a)
	1.53	Type (a)
	2.04	Type (a)
	2.65	Type (a)
	2.67	Type (b)
	2.84	Type (b)
	3.05	Type (b)
	3.56	Type (b)
	3.97	Type (b)
	4.07	Type (c)
	4.58	Type (c)
	5.29	Type (c)

Table 5.2: Failure response results for bi-linear distribution loaded plate when $K = 2.04$, 2.25 and 2.51

K	$I(Ns)$	Failure Modes
2.83	1.02	Type (a)
	1.17	Type (a)
	1.56	Type (a)
	1.95	Type (a)
	2.03	Type (a)
	2.12	Type (b)
	2.35	Type (b)
	2.54	Type (b)
	2.81	Type (d)
	2.95	Type (c)
	3.05	Type (c)
	3.52	Type (c)
3.25	0.75	Type (a)
	0.87	Type (a)
	1.16	Type (a)
	1.44	Type (a)
	1.50	Type (a)
	1.62	Type (b)
	1.73	Type (b)
	1.88	Type (b)
	2.02	Type (b)
	2.08	Type (d)
	2.25	Type (d)
	2.37	Type (c)
	2.60	Type (c)
3.81	0.53	Type (a)
	0.61	Type (a)
	0.81	Type (a)
	1.05	Type (a)
	1.20	Type (d)
	1.21	Type (d)
	1.32	Type (d)
	1.42	Type (d)
	1.58	Type (d)
	1.82	Type (c)

Table 5.3: Failure response results for bi-linear distribution loaded plate when $K = 2.83$, 3.25 and 3.81

K	$I(Ns)$	Failure Modes
	0.36	Type (a)
	0.40	Type (a)
	0.53	Type (a)
	0.66	Type (a)
	0.71	Type (a)
4.59	0.79	Type (a)
	0.89	Type (d)
	0.92	Type (d)
	1.07	Type (d)
	1.19	Type (d)
	1.42	Type (c)
	0.29	Type (a)
	0.31	Type (a)
	0.41	Type (a)
	0.51	Type (a)
	0.61	Type (a)
5.11	0.72	Type (a)
	0.82	Type (d)
	0.87	Type (d)
	0.92	Type (d)
	1.17	Type (d)
	1.23	Type (c)
	0.25	Type (a)
	0.31	Type (a)
	0.38	Type (a)
	0.46	Type (a)
	0.51	Type (a)
5.73	0.61	Type (a)
	0.76	Type (a)
	1.01	Type (e)
	1.15	Type (e)
	1.52	Type (c)

Table 5.4: Failure response results for bi-linear distribution loaded plate when $K = 4.59$, 5.11 and 5.73

K	$I(Ns)$	Failure Modes
6.52	0.19	Type (a)
	0.22	Type (a)
	0.28	Type (a)
	0.33	Type (a)
	0.38	Type (a)
	0.44	Type (a)
	0.46	Type (a)
	0.57	Type (a)
	0.66	Type (a)
	0.76	Type (a)
	0.83	Type (a)
	0.88	Type (e)
	0.95	Type (e)
	3.80	Type (c)
7.49	0.14	Type (a)
	0.19	Type (a)
	0.23	Type (a)
	0.29	Type (a)
	0.34	Type (a)
	0.43	Type (a)
	0.49	Type (a)
	0.53	Type (a)
	0.58	Type (a)
	0.60	Type (a)
	0.64	Type (a)
	0.68	Type (a)
	0.72	Type (a)

Table 5.5: Failure response results for bi-linear distribution loaded plate when $K = 6.52$ and 7.49

5.3.2 Dimensionless I-K diagram

Dimensionless I-K diagrams on the likely failure modes a target plate will sustain for a blast load with bi-linear distribution is obtained from the parametric study. Here, the applied total impulse I is divided by I_0 which is obtained from previous section. I_0 is defined as the minimum intensity of impulse that could cause failure of plate when subjected to uniform distribution load and is equal to 3 Ns in this study.

From the Figure 5.7, it can be concluded that for the sufficiently large impulse magnitude and value of K, the peak radial bending moment at some radii reaches the fracture criterion so a circumferential fracture is produced. At the same time, radial fracture is produced at the same location. The radial fracture is initiated at the radius greater than or equal to that of the circumferential fracture so they will not propagate inwards. For small impulse intensity and small value of K, only the peak bending moment at the centre reaches the fracture stress, so radial fracture is initiated from the centre. With increased intensity of impulse, a circumferential fracture is initiated at some distance away from the centre. Further increasing the intensity will result in the Type (c) failure mode as shown in Figure 5.6c. Type (c) is defined as two circumferential fracture connected by radial fracture within the two circles.

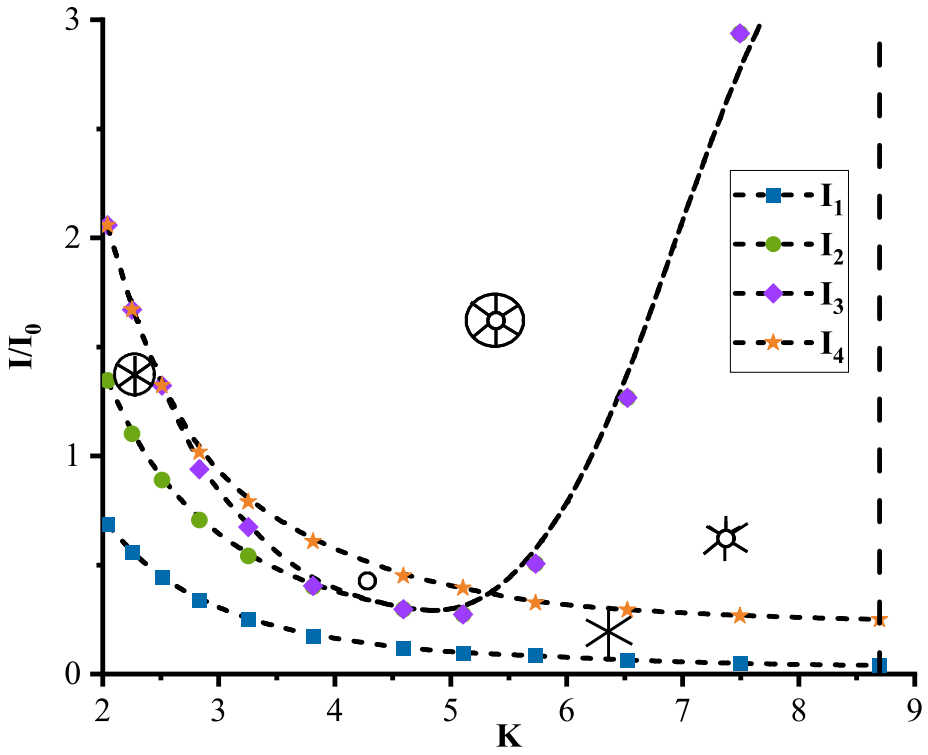

Figure 5.7: Idealised dimensionless $I - K$ diagram for bi-linear distribution loaded plate, K is the impulse enhancement factor defined in Section 3.6.2, I is the applied impulse and I_0 is the minimum intensity of impulse that could cause failure of plate when subjected to uniform distribution load; failure modes (a), (b), (c), (d), (e) defined in Figure 5.6 are expected to occur for points located at the corresponding area which is divided by four critical lines I_1, I_2, I_3, and I_4

5.4 Exponentially Decaying Load Distribution

5.4.1 Failure Modes

The third blast loading shape is that investigated in this chapter is the linear exponentially load distribution. This blast load distribution is illustrated in Figure 5.8.

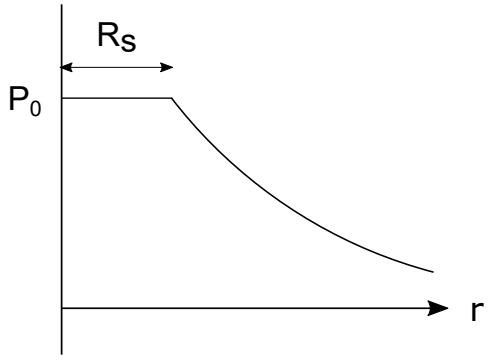

Figure 5.8: Bi-linear load distribution

This loading model has a constant pressure value P acting over a certain radius R_s and then followed by an exponentially decaying velocity distribution on the remainder of the structure along the radial direction:

$$P(r) = \begin{cases} P, & 0 \leq r \leq R_s \\ Pe^{-k(r-R_s)}, & R_s \leq r \leq R_p \end{cases} \tag{5.3}$$

where $P(r)$ is the spatial variation of pressure in the radial direction, r is the radial coordinate and R_s is the charge radius, k is the exponential decay parameter and R_p is the radius of the plate. The value of k is obtained from a combined experimental and numerical approach (Rezasefat et al. 2019):

$$k = 130 - 261(\frac{R_s}{R_p}) + 948(\frac{R_s}{R_p})^2 \;\; 0.15 \leq \frac{R_s}{R_p} \leq 0.6 \tag{5.4}$$

The results from the parametric study are provided in Table 5.6 and 5.7. There are 3 different failure modes may occur for a brittle plate under a linear-exponentially decaying distribution blast loading as shown in Figure 5.9.

K	$I(Ns)$	Fracture time (μs)	Fracture location	Failure Modes
2.70	1.1	54.40	origin	Type (a)
	1.5	34.39	origin	Type (a)
	2	32.20	origin	Type (a)
	2.2	31.40 151.41	origin $\xi = 39.46$	Type (b)
	2.5	30.40 135.98	origin $\xi = 39.92$	Type (b)
	2.6	22.20 131.40	$\xi = 7.257$ $\xi = 39.01$	Type (c)
	3	14.00 91.36	$\xi = 9.979$ $\xi = 29.03$	Type (c)
	4	5.40 14.40	$\xi = 11.79$ $\xi = 22.68$	Type (c)
2.49	1.3	64.40	origin	Type (a)
	1.5	52.40	origin	Type (a)
	2.6	40.60 150.44	origin $\xi = 38.56$	Type (b)
	3	24.80 132.18	$\xi = 9.072$ $\xi = 37.65$	Type (c)
2.31	1.5	84.00	origin	Type (a)
	1.8	62.20	origin	Type (a)
	2	56.00	origin	Type (a)
	2.2	54.00	origin	Type (a)
	3	50.60	origin	Type (a)
	3.1	49.80 150.44	origin $\xi = 36.29$	Type (b)
	3.2	34.004 141.63	$\xi = 10.43$ $\xi = 36.29$	Type (c)

Table 5.6: Failure response results for linear-exponentially decaying distribution loaded plate when $K = 2.70$, 2.49 and 2.31

K	$I(Ns)$	Fracture time (μs)	Fracture location	Failure Modes
2.15	1.7	102.38	origin	Type (a)
	2	75.60	origin	Type (a)
	2.5	65.60	origin	Type (a)
	3	62.60	origin	Type (a)
	3.5	60.80	origin	Type (a)
	3.6	43.60 60.40	$\xi = 11.79$ origin	Type (d)
	3.8	36.20 150.97	$\xi = 11.79$ $\xi = 34.02$	Type (c)
	4	33.60 142.42	$\xi = 13.61$ $\xi = 34.47$	Type (c)
	6	11.80 13.60	$\xi = 18.6$ $\xi = 29.94$	Type (c)
2.01	1.9	201.41	origin	Type (a)
	2.5	83.80	origin	Type (a)
	3	76.40	origin	Type (a)
	3.2	43.20	origin	Type (a)
	3.4	42.40	origin	Type (a)
	4	41.40 51.40	origin $\xi = 11.34$	Type (b)
	4.5	43.60 41.00	$\xi = 12.25$ origin	Type (b)
	4.6	43.20 41.00	$\xi = 12.25$ origin	Type (b)
	4.8	33.20 109.97 40.57	$\xi = 15.88$ $\xi = 41.73$ origin	Type (c)
	5	25.20 40.60 102.38	$\xi = 17.24$ origin $\xi = 42.18$	Type (c)
1.88	2.1	186.95	origin	Type (a)
	3	96.83	origin	Type (a)
	4	50.00	origin	Type (a)
	4.3	61.40 49.40	$\xi = 12.7$ origin	Type (b)
	4.5	60.20 49.00	$\xi = 12.25$ origin	Type (b)
	5	52.40 46.00	$\xi = 12.7$ origin	Type (b)
	5.6	33.00 44.40 88.80	$\xi = 18.14$ origin $\xi = 44.45$	Type (c)
	6	23.20 44.00 80.40	$\xi 20.87$ origin $\xi = 45.81$	Type (c)

Table 5.7: Failure response results for linear-exponentially decaying distribution loaded plate when $K = 2.15$, 2.01 and 1.88

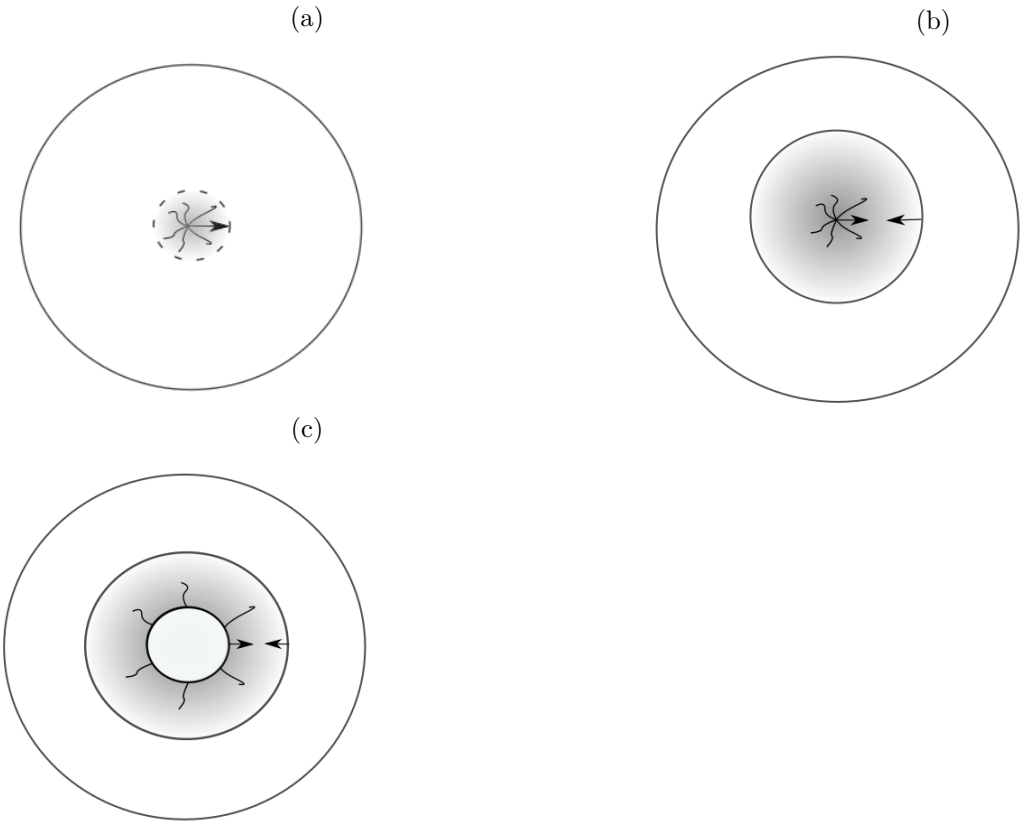

Figure 5.9: Propagation of radial and circumferential crack in the linear-exponentially decaying distribution loaded plate: (a) radial fracture initiated from the centre; (b) radial fracture initiated from the centre and circumferential fracture initiated at some distance away from the centre at later times; (c) radial fracture initiated at some distance away from the centre, two circumferential fractures initiated at two different radii

5.4.2 Dimensionless I-K diagram

Dimensionless I-K diagrams on the likely failure modes a target plate will sustain for a blast load with linear-exponentially decaying distribution is obtained from the parametric study.

It can be seen from the Figure 5.10 that for a small intensity of load, only the peak bending moment at the centre reaches the fracture stress, so radial fracture is initiated from the centre. These results are consistent with that observed in dimensionless $I - K$ diagram for bi-linear distribution loaded plate. With increased intensity of impulse, a circumferential fracture is initiated at some distance away from the centre. Further increasing the intensity will result in the Type (c) failure mode as shown in Figure 5.9c. Type (c) is defined as two circumferential fracture connected by radial fracture within the two circles.

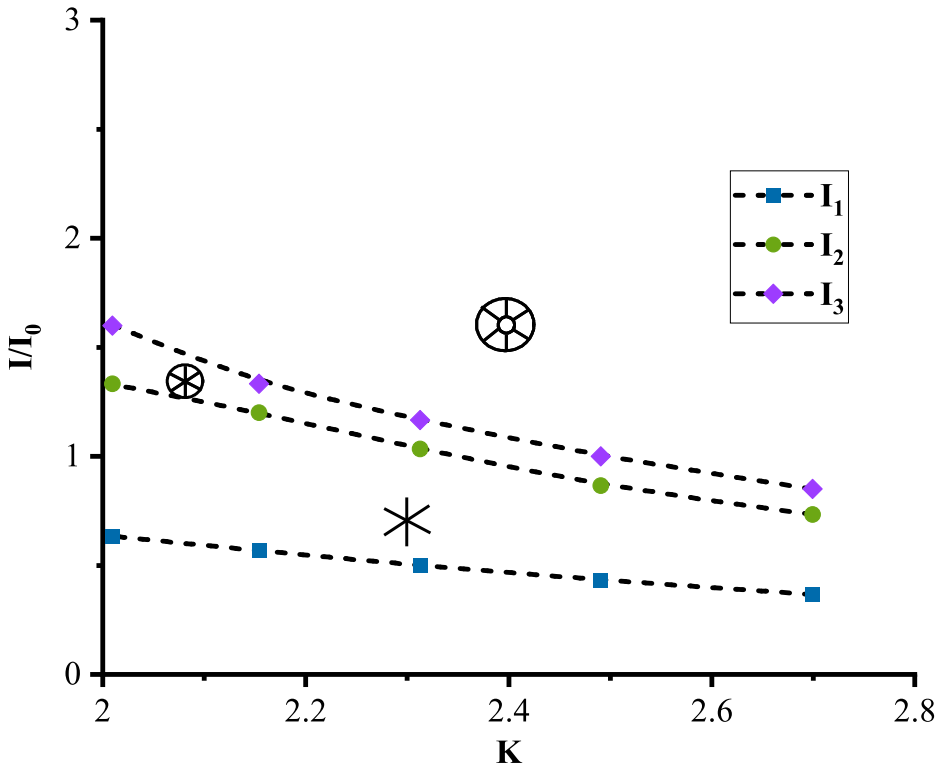

Figure 5.10: Idealised dimensionless I-K diagrams for linear-exponentially decaying distribution loaded plate, failure modes (a), (b), (c) defined in Figure 5.9 are expected to occur for points located between the critical line I_1 and I_2, between I_2 and I_3, and above I_3

5.5 Gaussian Load Distribution

5.5.1 Failure Modes

The fourth blast loading shape that investigated in this chapter is the Gaussian load distribution. The Gaussian blast loading is illustrated in Figure 5.11 (Pannell et al. 2021).

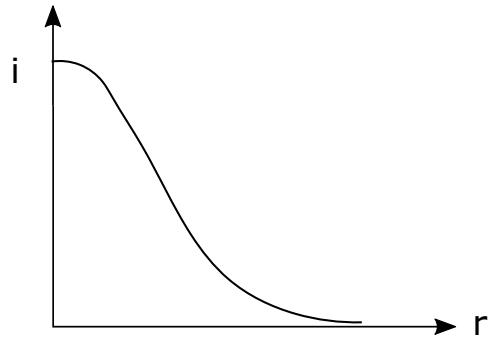

Figure 5.11: Gaussian blast distribution

This loading model has a constant velocity value V acting over a certain radius R and then followed by a linearly decaying velocity distribution on the remainder of the structure along the radial direction:

$$i(Z,\theta,W) = 0.557Z^{-1.663}exp(\frac{-\theta^2}{2007})W^{1/3} \;\; 0.11 \leq Z \leq 0.55m/kg^{1/3} \tag{5.5}$$

where i is the specific impulse, Z is the scaled distance, W is the charge weight and θ is the angle of incidence.

The results from the parametric study are provided in Table 5.8, Table 5.9, Table 5.10 and Table 5.11. There are 4 different failure modes may occur for a brittle plate under a Gaussian distribution blast loading as shown in Figure 5.12.

K	$I(Ns)$	Fracture time (μs)	Fracture location	Failure Modes
1.52	1.94	539.16	origin	Type (a)
	2.07	527.17	origin	Type (a)
	2.12	286.43	origin	Type (a)
	2.20	275.84	origin	Type (a)
	2.25	275.14 291.01	origin boundary	Type (b)
	2.28	15.56 290.39	origin boundary	Type (b)
	2.59	13.00 264.56	origin boundary	Type (b)
	2.84	11.80 253.97	origin boundary	Type (b)
	4.27	5.00 62.40	origin $\xi = 25.85$	Type (c)
	5.26	4.40 33.60	origin $\xi = 18.6$	Type (c)
	7.54	3.60 16.00	origin $\xi = 14.51$	Type (c)
	9.73	3.19 13.00	origin $\xi = 12.25$	Type (c)
	11.86	3.00 11.61	origin $\xi = 11.79$	Type (c)

Table 5.8: Failure response results for Gaussian distribution loaded plate when $K = 1.52$

K	$I(Ns)$	Fracture time (μs)	Fracture location	Failure Modes
1.39	2.29	538.02	origin	Type (a)
	2.47	508.03	origin	Type (a)
	2.51	290.83	boundary	Type (b)
		498.60	origin	
	2.71	271.96	boundary	Type (b)
		277.17	origin	
	2.91	265.79	boundary	Type (b)
		273.64	origin	
	3.11	259.18	boundary	Type (b)
		264.38	origin	
	3.15	104.41	origin	Type (b)
		255.21	boundary	
	3.21	104.76	origin	Type (b)
		255.38	boundary	
	3.30	101.77	origin	Type (b)
		250.80	boundary	
	4.27	23.20	origin	Type (b)
		232.02	boundary	
	4.98	14.99	origin	Type (d)
		155.21	$\xi = 15.42$	
		220.20	boundary	
	5.20	14.60	origin	Type (d)
		150.62	$\xi = 14.06$	
		212.79	boundary	
	5.71	13.40	origin	Type (d)
		138.98	$\xi = 11.79$	
		167.20	$\xi = 45.81$	
		209.00	boundary	
	5.75	14.00	origin	Type (d)
		138.01	$\xi = 11.79$	
		165.96	$\xi = 45.81$	
		204.77	boundary	
	6.11	13.00	origin	Type (d)
		131.22	$\xi = 8.165$	
		153.62	$\xi = 46.27$	
		203.80	boundary	

Table 5.9: Failure response results for Gaussian distribution loaded plate when $K = 1.39$

K	$I(Ns)$	Fracture time (μs)	Fracture location	Failure Modes
1.28	2.58	508.83	origin	Type (a)
	2.70	489.60	origin	Type (a)
	2.74	487.22	origin	Type (a)
	2.77	484.84	origin	Type (a)
	2.79	481.58	origin	Type (a)
	2.82	291.63 480.96	boundary origin	Type (b)
	3.04	272.40 470.03	boundary origin	Type (b)
	3.21	265.17 277.17	boundary origin	Type (b)
	3.38	259.18 265.61	boundary origin	Type (b)
	3.58	109.61 255.56	origin boundary	Type (b)
	3.71	103.00 251.24	origin boundary	Type (b)
	6.09	34.80 201.24	origin boundary	Type (b)
	6.86	26.40 194.01	origin boundary	Type (b)
	7.16	24.60 175.49	origin x=48.08	Type (c)
	8.36	21.52 145.77	origin $\xi = 47.63$	Type (c)

Table 5.10: Failure response results for Gaussian distribution loaded plate when when $K = 1.28$

K	$I(Ns)$	Fracture time (μs)	Fracture location	Failure Modes
1.21	2.77	499.22	origin	Type (a)
	3.01	475.76	origin	Type (a)
	3.13	291.98 468.62	boundary origin	Type (b)
	3.31	271.96 463.59	boundary origin	Type (b)
	3.3801	303.18 270.38	origin boundary	Type (b)
	4.06	108.82 253.00	origin boundary	Type (b)
	4.74	101.24 240.39	origin boundary	Type (b)
	6.12	93.56 195.24	$\xi = 5.443$ boundary	Type (b)
	6.79	77.20 144.01	origin $\xi = 14.06$	Type (c)
	7.46	52.80 140.39	origin $\xi = 13.61$	Type (c)
	10.05	34.39 44.80	origin boundary	Type (b)
1.16	2.93	498.42	origin	Type (a)
	2.99	487.58	origin	Type (a)
	3.42	290.83 459.18	boundary origin	Type (b)
	3.51	281.22 300.01	boundary origin	Type (b)
	3.64	290.39 270.38	origin boundary	Type (b)
	4.28	248.42 257.24	origin boundary	Type (b)
	4.53	108.38 249.56	origin boundary	Type (b)
	5.99	100.00 162.17	origin $\xi = 17.24$	Type (c)
	9.08	64.38 76.60	boundary origin	Type (2)

Table 5.11: Failure response results for Gaussian distribution loaded plate when $K = 1.21$ and 1.16

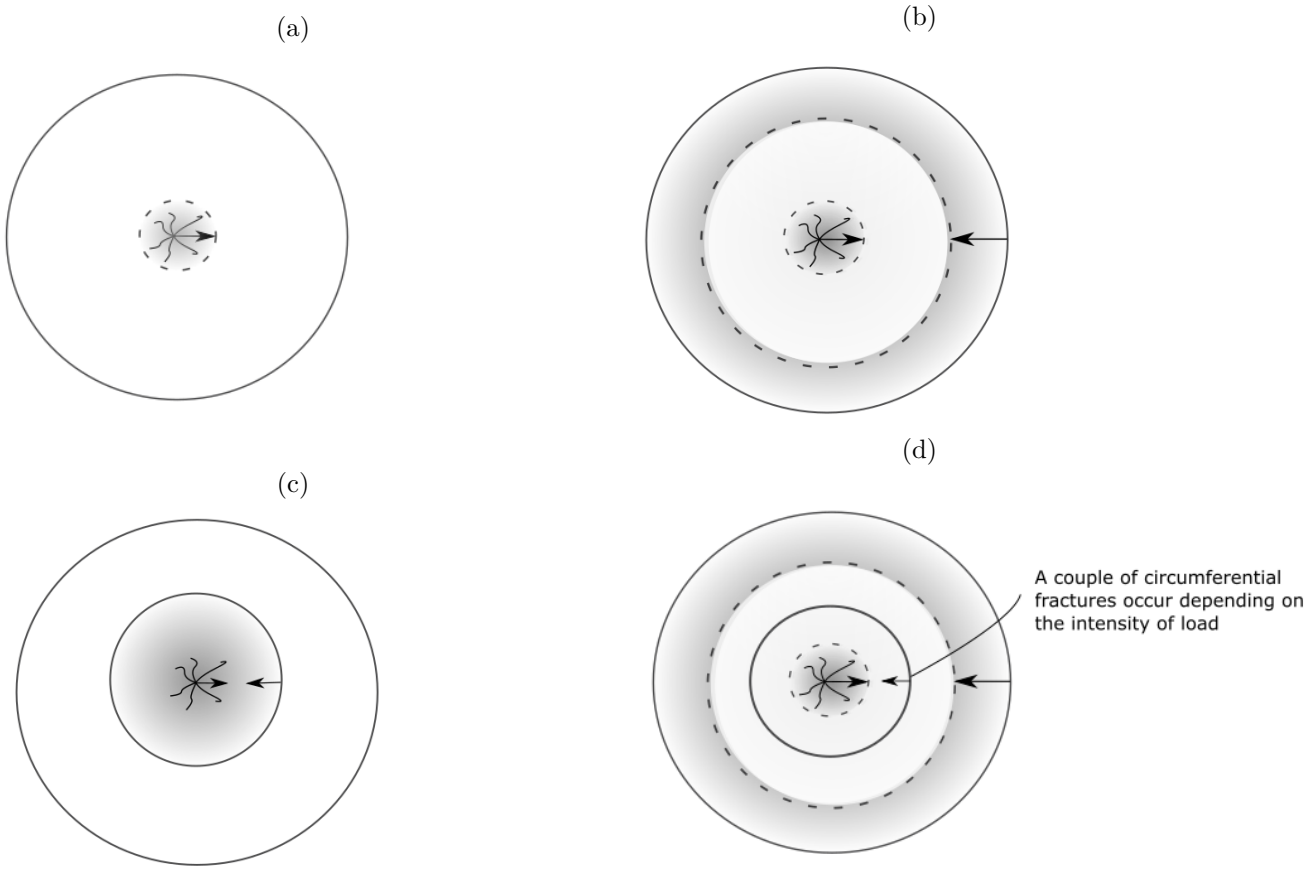

Figure 5.12: Propagation of radial and circumferential crack in the Gaussian distribution load--ed plate: (a) radial fracture initiated from the centre; (b) radial fracture initiated from the centre and circumferential fracture initiated at the boundary at later times; (c) radial fracture initiated at some distance away from the centre, one circumferential fracture initiated at some distance away from the centre; (d) radial fracture initiated from the centre firstly, one circumferential fracture initiated at some distance away from the centre secondly and one circumferential fracture initiated at the boundary finally

5.5.2 Dimensionless I-K diagram

Dimensionless I-K diagrams on the likely failure modes a target plate will sustain for a blast load with rectangular distribution is obtained from the parametric study.

It can be seen from the Figure 5.13 that for a small intensity of load, only the peak bending moment at the centre reaches the fracture stress, so radial fracture is initiated from the centre. This results is consistent with that observed in dimensionless $I - K$ diagram for bi-linear distribution loaded plate. With increased intensity of impulse, a circumferential fracture is initiated at the centre boundary which is different from those observed in previous loading cases. The reason to this is because of the smaller value of K here. As all the values of K considered in bi-linear distribution and linear-exponentially distribution are larger than 2 while for Gaussian load distribution, K is limited to be less than 2. Further increasing the intensity will result in the Type (c) failure mode as shown in Figure 5.12c. Type (c) is defined as two circumferential fracture connected by radial fracture within the two circles. It is worth mentioning that there is a small 'failure zone' in this dimensionless diagram which defines the Type (d) failure mode as shown in Figure 5.12d. It is described as radial fracture initiates from the centre firstly, then one circumferential fracture initiates at some distance away from the centre finally and one circumferential fracture initiated at the boundary.

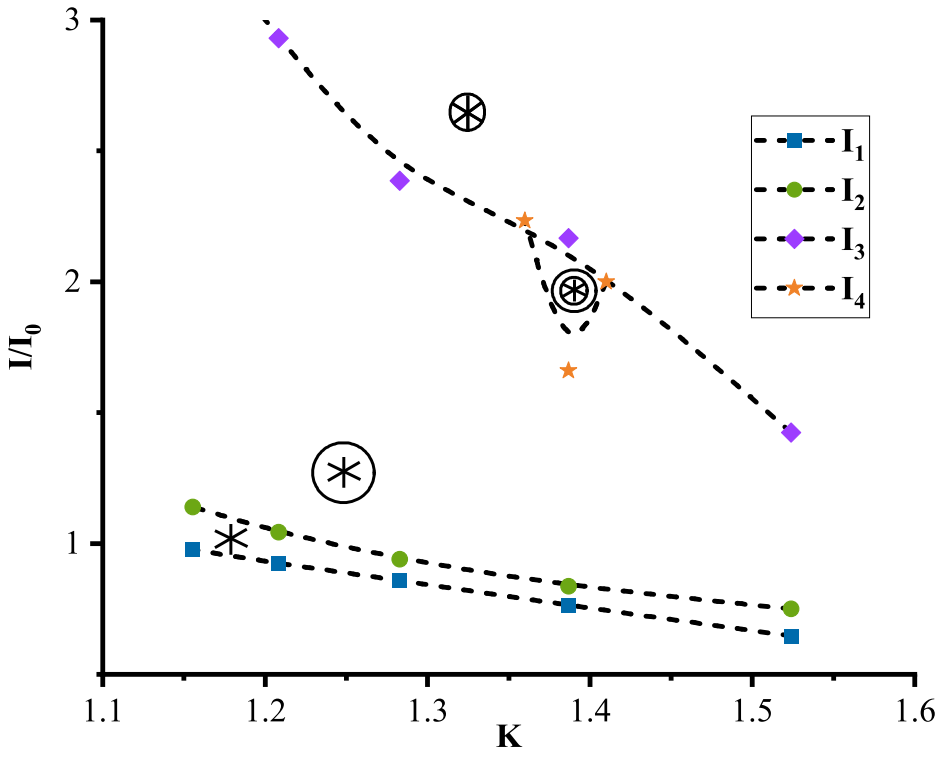

Figure 5.13: Idealised dimensionless I-K diagrams for Gaussian distribution loaded plate

5.6 Rectangular Load Distribution

5.6.1 Failure Modes

The fifth blast loading shape that investigated in this chapter is the Gaussian load distribution. The Gaussian shape of blast loading is illustrated in Figure 5.14.

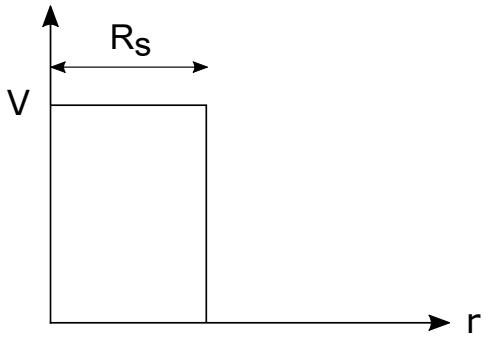

Figure 5.14: Rectangular blast distribution

This loading model has a constant velocity value V acting over a certain radius R and then followed by a sharp decrease to zero:

$$V(r) = V \;\; 0 \leq r \leq R_s \tag{5.6}$$

This case could be considered as a special case of the bi-linear distribution of which the taper length d_t is equal to zero.

The results from the parametric study are provided in Table 5.12, Table 5.13 and Table 5.14. There are 3 different failure modes may occur for a brittle plate under a rectangular distribution blast loading as shown in Figure 5.15.

K	$I(Ns)$	Fracture time (μs)	Fracture location	Failure Modes
10.04	0.09	8.60	origin	1
	0.10	5.19	origin	Type (a)
	0.12	5.07	origin	Type (a)
	0.15	5.00	origin	Type (a)
	0.22	3.00	origin	Type (b)
		4.80	$\xi = 8.17$	
6.96	0.15	13.60	origin	1
	0.20	12.40	origin	Type (a)
	0.22	7.66	origin	Type (a)
	0.30	7.41	$\xi = 2.27$	Type (b)
	0.37	5.00	$\xi = 4.54$	Type (b)
	0.38	4.40	$\xi = 5.44$	Type (b)
	0.47	4.80	$\xi = 10.89$	Type (c)
		3.40	$\xi = 5.44$	
5.21	0.27	13.60	origin	Type (a)
	0.55	9.80	origin	Type (a)
	0.65	5.40	$\xi = 7.26$	Type (b)
	0.70	4.40	$\xi = 8.17$	Type (b)
	0.80	3.60	$\xi = 8.17$	Type (c)
		5.00	$\xi = 13.61$	
	1.00	2.80	$\xi = 9.07$	Type (c)
		3.20	$\xi = 12.7$	
	1.20	2.40	$\xi = 9.53$	Type (c)
		2.60	$\xi = 12.25$	
	1.50	2.00	$\xi = 9.53$	Type (c)
		2.20	$\xi = 12.25$	
	2.00	1.04	$\xi = 9.98$	Type (c)
		1.04	$\xi = 11.79$	
4.23	0.44	33.60	origin	1Type (a)
	1.00	5.40	$\xi = 9.98$	Type (b)
	1.10	4.40	$\xi = 10.89$	Type (b)
	1.20	3.80	$\xi = 10.89$	Type (c)
		5.00	$\xi = 16.33$	
	1.50	3.00	$\xi = 11.34$	Type (c)
		3.20	$\xi = 15.42$	

Table 5.12: Failure response results for rectangular distributed loaded plate when $K = 10.04$, 6.96, 5.21 and 4.23

K	$I(Ns)$	Fracture time (μs)	Fracture location	Failure Modes
	0.64	43.60	origin	Type (a)
	1.00	31.20	origin	Type (a)
	1.10	30.80	origin	Type (a)
	1.15	22.40	$\xi = 6.35$	Type (b)
	1.20	22.20	$\xi = 5.90$	Type (b)
	1.50	5.40	$\xi = 12.70$	Type (b)
3.51	1.60	4.40	$\xi = 13.61$	Type (b)
	1.72	4.00	$\xi = 13.61$	Type (c)
		5.60	$\xi = 19.50$	
	2.00	3.20	$\xi = 14.51$	Type (c)
		3.60	$\xi = 18.60$	
	2.50	2.60	$\xi = 14.51$	Type (c)
		2.80	$\xi = 18.14$	
	0.88	54.40	origin	Type (a)
	0.92	45.20	origin	Type (a)
	1.00	31.20	origin	Type (a)
	1.60	25.60	$\xi = 7.71$	Type (b)
	1.75	24.40	$\xi = 8.68$	Type (b)
3.04	1.80	23.40	$\xi = 9.07$	Type (b)
	2.10	5.20	$\xi = 15.88$	Type (b)
	2.35	4.00	$\xi = 16.33$	Type (c)
		4.80	$\xi = 21.77$	
	3.00	3.00	$\xi = 17.24$	Type (c)
		3.20	$\xi = 20.87$	
	1.15	64.40	origin	Type (a)
	2.10	33.40	$\xi = 8.62$	Type (b)
	2.50	14.00	$\xi = 14.97$	Type (b)
2.65	3.00	4.20	$\xi = 19.05$	Type (c)
		5.20	$\xi = 24.95$	
	4.00	2.80	$\xi = 19.96$	Type (c)
		3.20	$\xi = 24.04$	

Table 5.13: Failure response results for rectangular distributed loaded plate when $K = 3.51$, 3.04 and 2.65

K	$I(Ns)$	Fracture time (μs)	Fracture location	Failure Modes
2.37	1.20	615.97	origin	Type (a)
	1.43	96.03	origin	Type (a)
	2.50	60.80	origin	Type (a)
	2.65	43.00	$\xi = 9.98$	Type (b)
	3.00	33.40	$\xi = 11.34$	Type (b)
	3.78	4.20	$\xi = 21.77$	Type (c)
		5.20	$\xi = 27.67$	
	4.50	3.20	$\xi = 22.68$	Type (c)
		3.60	$\xi = 26.76$	
2.13	1.30	625.59	origin	Type (a)
	2.00	85.80	origin	Type (a)
	2.50	42.60	origin	Type (a)
	3.20	52.20	$\xi = 10.43$	Type (b)
	4.65	4.20	$\xi = 24.49$	Type (c)
		5.20	$\xi = 30.39$	
	5.00	3.80	$\xi = 24.49$	Type (c)
		4.20	$\xi = 29.48$	

Table 5.14: Failure response results for rectangular distributed loaded plate when $K = 2.37$ and 2.13

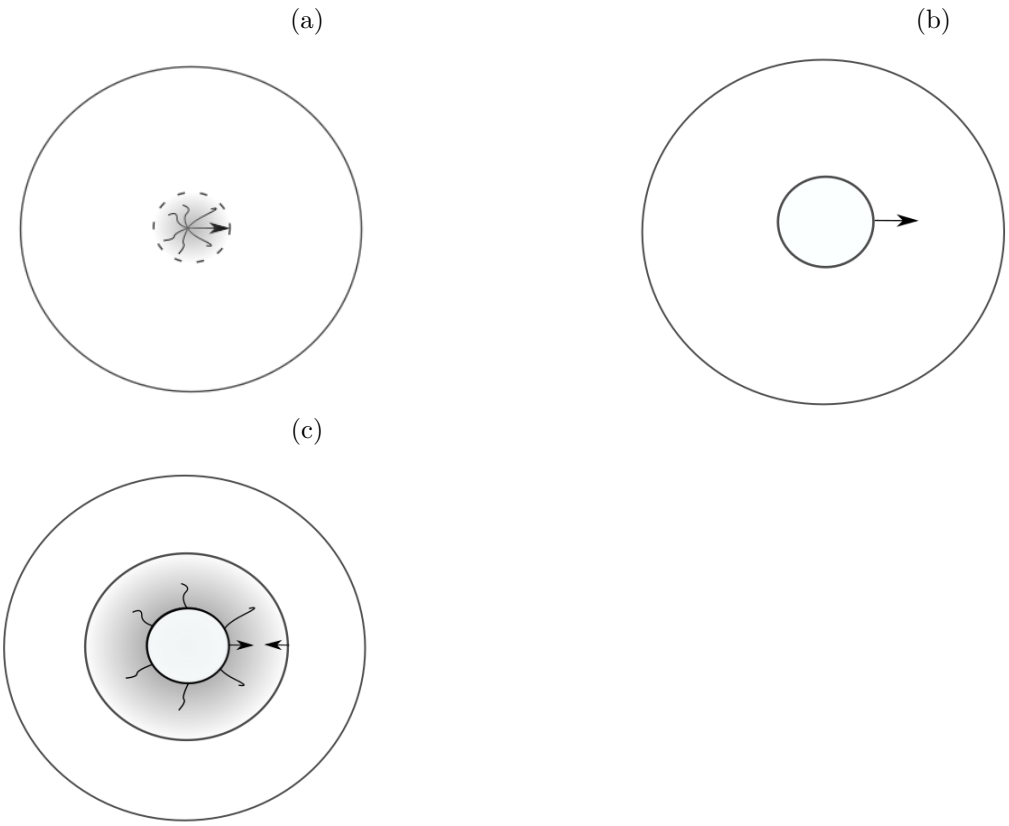

Figure 5.15: Propagation of radial and circumferential crack in the rectangular distributed loaded plate: (a) radial fracture initiated from the centre; (b) circumferential fracture initiated at distance away from the centre; (c) radial fracture initiated at some distance away from the centre, two circumferential fractures initiated at two different radii

5.6.2 Dimensionless I-K diagram

Dimensionless I-K diagrams on the likely failure modes a target plate will sustain for a blast load with rectangular distribution is obtained from the parametric study.

It can be seen from the Figure 5.16 that for a small intensity of load, only the peak bending moment at the centre reaches the fracture stress, so radial fracture is initiated from the centre. This results is consistent with that observed in dimensionless $I - K$ diagram for bi-linear distribution loaded plate. With increased intensity of impulse, a different failure type is observed that is a circumferential fracture initiating at a radius away from the centre. Further increasing the intensity will result in the Type (c) failure

mode as shown in Figure 5.15c. Type (c) is defined as two circumferential fracture connected by radial fracture within the two circles.

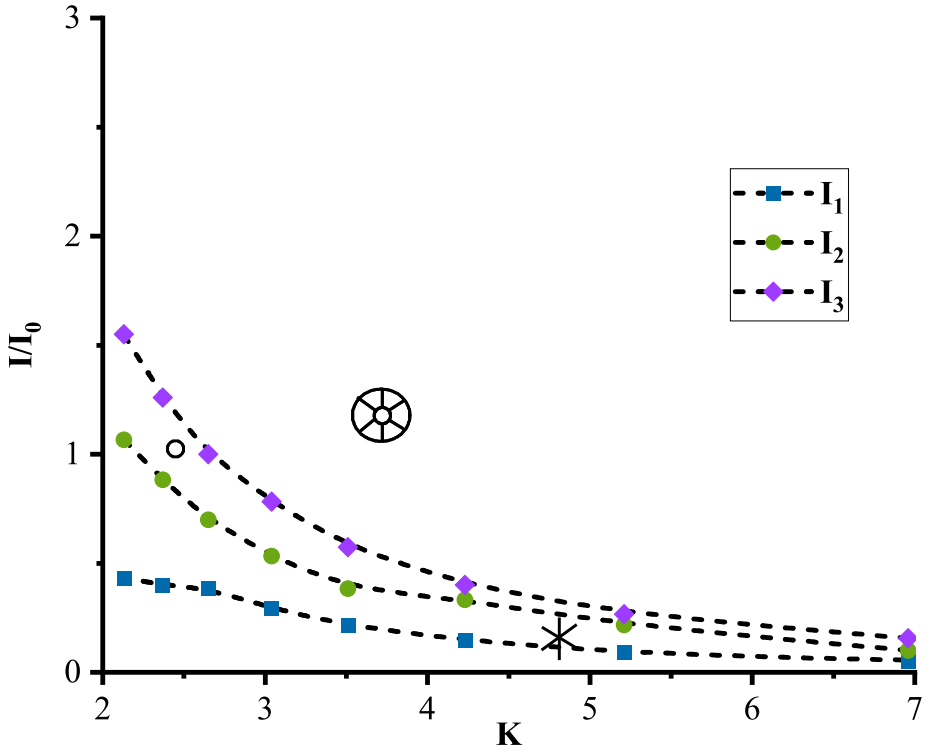

Figure 5.16: Idealised dimensionless I-K diagrams for rectangular distribution loaded plate, failure modes (a), (b), (c) defined in Figure 5.15 are expected to occur for points located between the critical line I_1 and I_2, between I_2 and I_3, and above I_3

5.7 Summary and Discussion

Results obtained from the parametric study show that for a plate subjected to blast loading, the failure response such as failure time, failure initiation location and failure modes are influenced by the loading shapes and magnitude. Dimensionless $I-K$ diagrams corresponding to each commonly used loading distribution were presented.

An interesting point is that the 'failure zones' in the dimensionless $I-K$ diagram for exponentially decaying load distribution (see Figure 5.10) and rectangular load distribution (see Figure 5.16) could overlap with those in the dimensionless $I-K$ diagram for bi-linear load distribution (see Figure 5.7) with a high level of quantitative agreement. In addition, if the results obtained from the Table 5.1 were plotted together with the dimensionless $I-K$ diagram for Gaussian load distribution (see Figure 5.13) which gives:

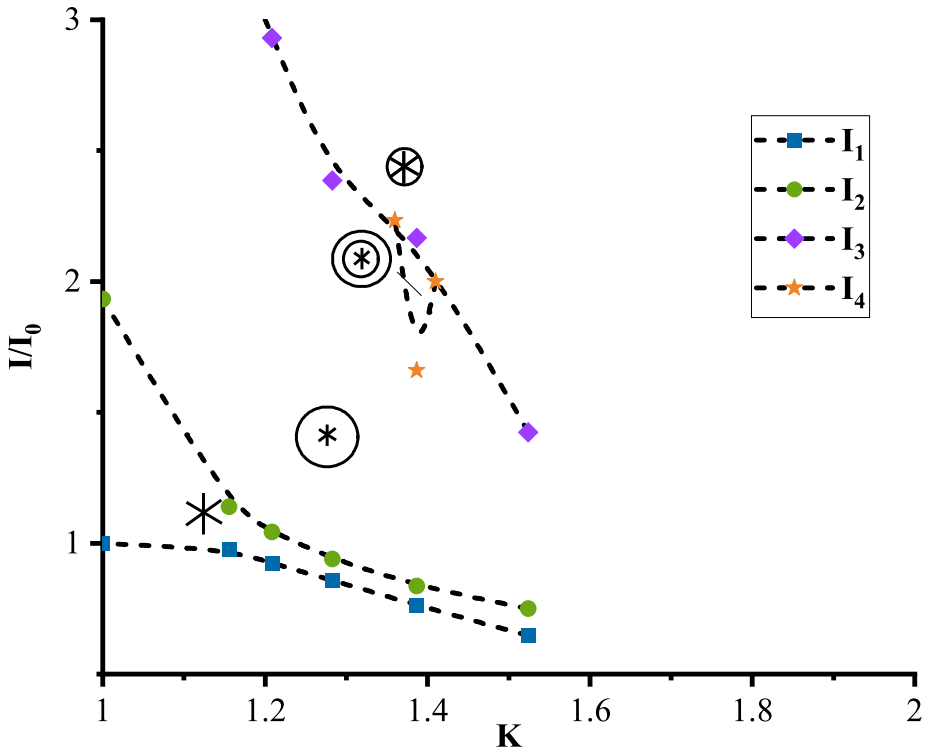

Figure 5.17: Idealised dimensionless $I-K$ diagrams for $1 \leq K \leq 2$

The 'break-off' of the critical lines in the Figure 5.17 is due to the lack of loading shapes for calculating the K value. In this study, we choose the 5 most commonly used loading shapes in the literature. However, some of the equation used for defining the spatial distribution is limited by some influencing factors, e.g., for the linear-exponentially load distribution (see (5.4)), the exponential decay parameter is limited to an interval $(0.15 \leq \frac{R_s}{R_p} \leq 0.6)$ such that limits the interval of K. Future work on calculating the K value for other loading shapes could complement this figure.

Combing the Figure 5.17 and Figure 5.7, failure modes of brittle plates subjected to blast loading with arbitrary distribution and magnitude could be determined.

A flowchart to determine the failure response of blast-loaded plate is shown in Figure 5.18. If engineers, designers, or researchers are given the task of determining the failure mode, failure time, and failure initiation locations, they could refer to this flowchart.

The proposed analytical method for predicting the failure response of plates subjected to blast loading has potential practical applications for protective design in certain scenarios. Specifically, this method can be used to evaluate the effectiveness of existing protection measures, such as brittle and linear elastic materials. Furthermore, this analytical solution can provide a valuable first stage of research towards the use of such materials in laminated panels or reinforced structures. Future research could extend the findings of this study to evaluate the effectiveness of these materials in more complex structures, leading to more comprehensive protective design strategies. In the event of a terrorist attack involving such materials, incorporating the insights provided by this study into current safety protocols and emergency response plans can help engineers and first responders better assess the potential damage and casualties resulting from such an event and develop more effective strategies for mitigating the impact.

It is the hope of this author that it could provide a strategy to develop a fast-running engineering tool for assessing the blast performance of the structures such that more robust and effective structural system could be provided.

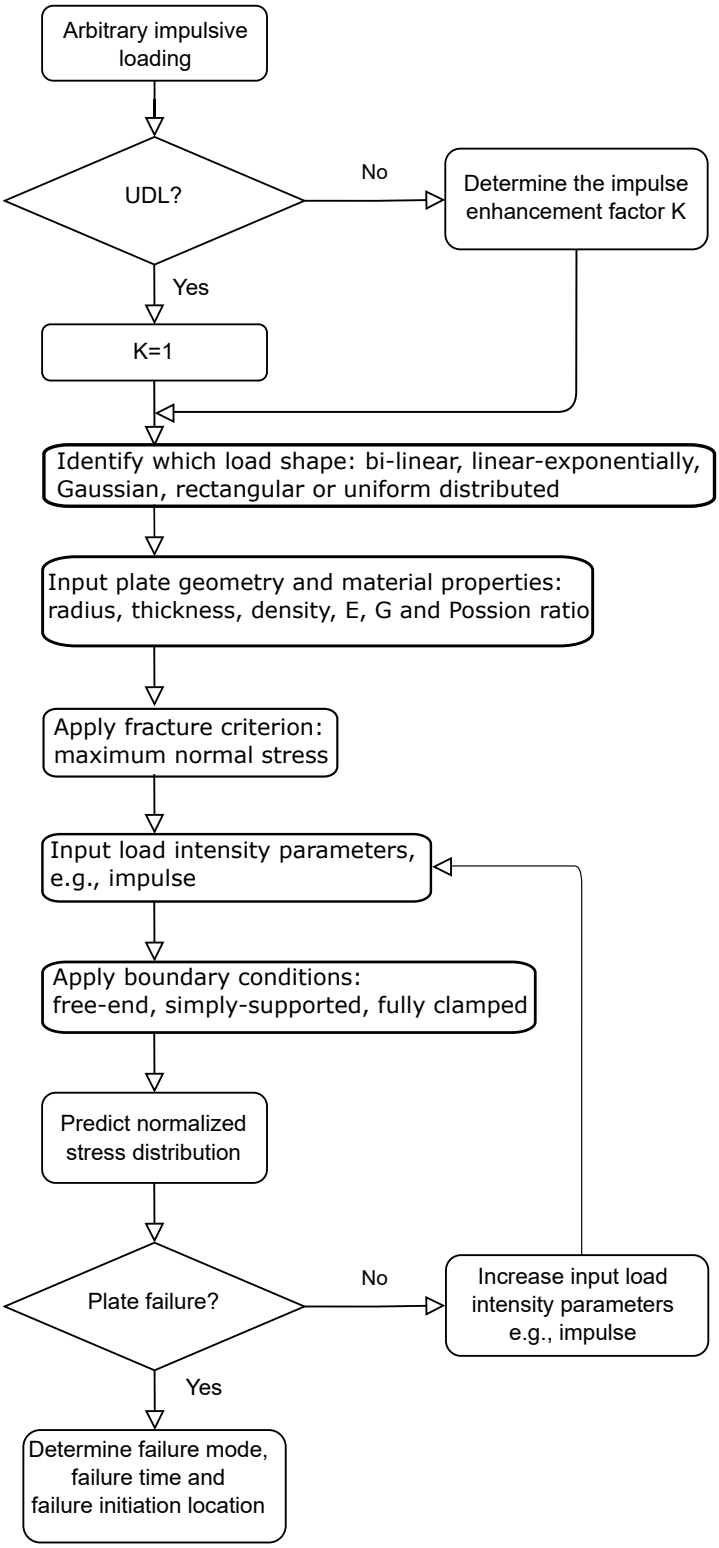

Figure 5.18: Flowchart of Matlab script given in Appendix A.1 to determine the failure behaviour of blast-loaded plates

Chapter 6

Summary and Conclusions

6.1 Summary

Terror attacks can range from large vehicle-borne explosives, to small hand-held devices. The portability and increased difficulty in detecting such devices means that they are more typically used to target a key building component or piece of critical infrastructure. Catastrophic failure of structural elements in these events can lead to loss of life and economic damage. Thus, there is a pressing need to improve the blast-resistant performance of the vulnerable structures and design adequate and efficient protective engineering systems against such threats. This requires a detailed understanding of the effects of the imparted explosion loading on the structure, i.e. the resultant deformation and failure behaviour. The present thesis has aimed to investigate the influence of loading distribution and magnitude on the failure response of brittle plates, specifically to create a "fast-running tool", that can predict the failure response given the shape of loading shape and its magnitude.

In Chapter 2, the current literature in the field of structural response prediction in a blast context is discussed, as well as the theoretical background of shock wave formation and the modes of deformation. It also provides a general overview into plate theories as a field of study, and how its application is used in a blast engineering context. In addition, existing predictive approaches for predicting failure response of plates are introduced.

In Chapter 3 this thesis presents the derivation of an analytical solution to predicting the failure response of a brittle plate. The characteristic method and finite difference scheme are used to solve the original hyperbolic partial differential equations describing the plate problem. It also provides a summary of most commonly used blast loading shapes in the blast engineering context and introduces the impulse enhancement factor for generalizing the predictive method.

Chapter 4 demonstrates a preliminary experimental validation and the numerical verification through LS-DYNA. Numerical model verification is performed considering the response of plates subjected to a bi-linear distribution of blast loading. Excellent agreement of stress time history, fracture time and fracture initiation location are shown and discussed against theoretical predictions.

In Chapter 5, this thesis performs a parametric study to investigate the dependence of failure response on the loading shape and intensity. Potential failure modes corresponding to each blast loading shapes are summarized and discussed. Non-dimensional $I - K$ diagrams are constructed for determining the failure modes when given the loading distribution and magnitude. Combing the non-dimensional $I - K$ diagrams for various K intervals allows the prediction for arbitrary blast loading. Further, a flowchart describing the procedure for failure response gives an insight into the development of a fas-running engineering tool for assessing the blast performance of structures.

6.2 Conclusions

The output of this thesis can be summarised in the following conclusions, which are listed in the order that they appear in the current work:

- An analytical solution is proposed to predict the failure response of brittle plates subjected to impulsive loadings as described in Chapter 3.
- The present method can be used to predict failure initiation location, failure time and failure modes of plates under blast loading with bi-linear distribution to a good level of agreement with data collected from experimental data by Colton (1976) and numerical results obtained from LS-DYNA.

- The present method can be used to predict stress time history of plates under blast loading with bi-linear distribution to a good level of agreement with numerical results obtained from LS-DYNA.
- Convergence study for the numerical analysis revealed that the fracture behaviour chould be predicted with good accuracy when the plate is divided into 5 layers through its thickness.
- From the parametric study, failure modes, failure time and failure initiation location of plates under impulsive loading with uniformly, bi-linear, linear-exponentially decaying, Gaussian and rectangular distributions are predicted by the proposed method. Potential failure modes that may occur for a brittle plate when subject to these blast loadings are summarized.
- The proposed method not only allows the failure response prediction for plates under uniform load distribution but also allows to predict the failure response of non-uniform loaded plates.
- Conducting the experimental research works dealing with blast loads need to consider both cost and safety issues. Besides, numerical analysis requires a high computational time. Therefore, the given analytical approach provides an alternative for failure response investigation.
- A flowchart to determine the failure behaviour of blast-loaded plates is proposed to provides a strategy to develop a fast-running engineering tool for assessing the blast performance of the structure.
- Dimensionless $I - K$ diagrams for 5 most commonly used blast loading in the literature are proposed to determine the potential failure modes a plate will sustain when given only the shape and magnitude of the load.
- Generalization work on dimensionless $I - K$ diagrams is conducted to allow the prediction for failure modes of plate under blast loading with arbitrary distribution and intensity. The obtained dimensionless $I - K$ diagrams could work for the value of K between 1 and 9.

6.3 Evaluation and Future Work

Further work within this thesis falls within two broad categories: the first, performing a more detailed parametric study; whilst the second is concerned with the non-brittle plates.

- Geometry of the plate

  This thesis focuses on the fracture behaviour of a circular plate with a fixed radius of $120mm$. Hence, it is apparent that further investigation is required to conduct the research on square plate and rectangular plate and identify the effect of plate geometry on failure response.

- Boundary conditions

  Dimensionless $I-K$ diagrams are obtained for fully clamped boundary conditions in this thesis, but the dimensionless $I-K$ diagrams for free end and simply supported plates remain topics for study. Efforts could be made to investigate the effect of boundary conditions on the fracture behaviour of plates subjected to blast loads. For simple supported and clamped ends, two state variables are given: $\overline{M}=0$ and $\overline{V}=0$ for simple support, and $\overline{w}=0$ and $\overline{V}=0$ for clamped ends, instead of the assumption given in Eq. 3.32.

- Eccentricity of the explosive

  In this thesis, explosive is assumed to be placed at the origin of the plate without eccentricity. Hence, it is valuable to investigate the effect of eccentricity on the results concluded from this thesis.

- Thickness of the plate

  In all above studies, the thickness of the plate is kept to be $6.35mm$. This is because a thick plate allows the use of Mindlin plate theory which takes the transverse shear deformation and rotary inertia into consideration. It would be interesting to see how the failure response is influenced by thickness and ascertain the validity of the analytical method and gives its effective range. For instance, for thin plates, classical plate theory is applicable for predicting the response of plate under blast loadings which implies the governing equations could be further simplified.

- Loading distributions

  This thesis has presented an analytical method for rapidly and accurately predicting failure response of brittle plate when subjected to blast loading with 5 most commonly-seen loading shapes (as summarized in Section 3.6). As better understanding of blast loading and more accurate characterisation of blast loading could be developed by other researchers for some specific explosion type, explosion configuration or stand-off distance. The tool developed in this thesis could be implemented to determine the dependence of failure response of plates on those new loading shapes so that further strengthen the generalizability of the tool.

- Accuracy of the tool

  The accuracy of the current analytical model is limited by the size of time step however after sensitivity analysis results have shown the predicted results become stable when $\Delta t = 0.2s$.

- Material of the plate

  In this thesis, the material under investigation is assumed to be brittle. To extend the work on failure response prediction for plates, it would be valuable to explore the quantification on the effect of loading shapes and magnitude on the failure response of non-brittle plates – in other words, allow plastic deformation exist in the plate. Improvements in the basic governing equations can be developed as response of metal plates and composite are better understood in recent years by other researchers (Jacob et al. 2007; Saeed Ahmad et al. 2018; McDonald et al. 2017, 2018; Langdon et al. 2014; Mohammadzadeh and Noh 2019).

- Number of radial fractures Since the analysis of blast response in plates is limited to axisymmetric conditions, it cannot account for the impact of non-axisymmetric failure modes. Consequently, the model can only make predictions for the radius of radial fracture but cannot predict the number of radial fracture.

- Comparison with other methods

  Due to the fact that existing methods for predicting the failure response of plates subjected to impulsive loading focus solely on metal plates, there is currently no available theoretical method for comparison in terms of predicting failure response for brittle plates, to the author's knowledge. However, it would also be worthwhile to compare the results predicted by the present method with other available methods

in the literature for predicting failure time, failure initiation location, and failure modes.

Most of research is based on the theoretical work due to the practical issue. By conducting a series of blast tests on brittle plates subjected to different explosion loadings, the accreditation of the method developed in this thesis could be improved. Approaching experimental work with an understanding of theoretical analysis will increase the integration between experimental and theoretical communities and further develop a reliable engineering tool which can be used for detailed mechanistic studies accelerating understanding of blast effects on structures.

Bibliography

Abrahamson, G. and Lindberg, H. (1976). Peak load-impulse characterization of critical pulse loads in structural dynamics. *Nuclear engineering and design*, 37(1):35–46.

ASM (2014). *ASM Handbook, Volume 14B: Metalworking: Sheet Forming*. American Society for Metals (ASM) International, USA.

Aune, V., Børvik, T., and Langseth, M. (2015). Behaviour of plated structures subjected to blast loading. In *11th International Conference on the Mechanical and Physical Behaviour of Materials under Dynamic Loading*, Lugano, Switzerland.

Babaei, H. and Darvizeh, A. (2012). Analytical study of plastic deformation of clamped circular plates subjected to impulsive loading. *Journal of Mechanics of Materials and Structures*, 7(4):309–322.

Babcock, S., Kumar, A., and Green, S. (1967). Response of materials to suddenly applied stress loads, part i: High strain-rate properties of eleven reentry-vehicle materials at elevated temperatures. Technical Report AFFDL-TR-67-3, Part I, Bergen, Norway.

Baker, W. (1973). *Explosions in Air*. University of Texas Press, Austin, TX, USA.

Ben-Ezra, M., Hamama-Raz, Y., and Mahat-Shamir, M. (2017). Psychological reactions to the 2017 manchester arena bombing: A population based study. *Journal of Psychiatric Research*, 95:235–237.

Bhaskar, K. and Varadan, T. (2014). *Plates: theories and applications*. John Wiley & Sons, Hoboken, NJ, USA.

Biggs, J. M. (1964). *Introduction to structural dynamics*. McGraw-Hill College, NY, USA.

Bimha, R. (1996). Response of thin circular plates to central blast loading. Master's thesis, University of Cape Town.

Birman, V. (2010). Plates and shells. *Eng. Educ. Cent*, 15:1–10.

Bodner, S. and Symonds, P. (1979). Experiments on viscoplastic response of circular plates to impulsive loading. *Journal of the Mechanics and Physics of Solids*, 27(2):91–113.

Chen, S., Chen, X., Li, G., and Lu, Y. (2017). A theoretical study on the pi diagram of framed monolithic glass window subjected to blast loading. *Engineering Structures*, 150:497–510.

Chen, S., Chen, X., Li, G., and Lu, Y. (2019). Development of pressure-impulse diagrams for framed pvb-laminated glass windows. *Journal of Structural Engineering*, 145(3):04018263.

Chou, P. and Mortimer, R. (1967). Solution of one-dimensional elastic wave problems by the method of characteristics. *Journal of Applied Mechanics*, 34(3):745–750.

Colton, J. (1974). *Multiple fracture of beams and plates under localized impulisve loading*. PhD thesis, Stanford University, USA.

Colton, J. (1976). Multiple fracture of plates under localized impulsive loading. *Journal of Applied Mechanics*, 43(1):33–38.

Cormie, D., Mays, G., and Smith, P. (2009). *Blast effects on buildings*. Thomas Telford Publishing, London, UK.

Corporation, L. S. T. (2021). *LS-DYNA Keyword User's Manual*. Livermore Software Technology Corporation.

Curry, R. and Langdon, G. (2017). Transient response of steel plates subjected to close proximity explosive detonations in air. *International Journal of Impact Engineering*, 102:102–116.

Curry, R. and Langdon, G. (2021). The effect of explosive charge backing in close-proximity air-blast loading. *International Journal of Impact Engineering*, 151:103822.

Dennis, A., Pannell, J., Smyl, D., and Rigby, S. (2020). Prediction of blast loading in an internal environment using artificial neural networks. *International Journal of Protective Structures*, 12(3):287–314.

Fallah, A., Nwankwo, E., and Louca, L. (2013). Pressure-impulse diagrams for blast loaded continuous beams based on dimensional analysis. *Journal of Applied Mechanics*, 80(5).

Feyerabend, P. (1996). *Killing time: the autobiography of Paul Feyerabend*. University of Chicago Press.

Flynn, B. (1995). Thoughts and reflections after the bombing of the alfred p. murrah federal building in oklahoma city. *Journal of the American Psychiatric Nurses Association*, 1(5):166–170.

Fuller, B. (2018). *Loading from Shallow Buried Blast Events and the Effect on Plate Deformations*. PhD thesis, University of Sheffield, UK.

Ganguly, S. (2009). India in 2008: Domestic turmoil and external hopes. *Asian Survey*, 49(1):39–52.

Gao, Y., Dong, Y., Xiao, L., Wang, F., and Feng, S. (2018). Preliminary similarity analysis on the deformation dynamic response of thin plates subjected to blast and impact loadings. *Propellants, Explosives, Pyrotechnics*, 43(6):583–594.

Hetherington, J. and Smith, P. (1994). *Blast and ballistic loading of structures*. CRC Press, NY, USA.

Irie, T., Yamada, G., and Aomura, S. (1980). Natural frequencies of mindlin circular plates. *Journal of Applied Mechanics*, 47(3):652–655.

Itao, K. and Crandall, S. (1979). Natural modes and natural frequencies of uniform, circular, free-edge plates. *Journal of Applied Mechanics*, 46(2):448–453.

Jacob, N., Nurick, G. N., and Langdon, G. S. (2007). The effect of stand-off distance on the failure of fully clamped circular mild steel plates subjected to blast loads. *Engineering Structures*, 29(10):2723–2736.

Jacob, N., Yuen, S., Nurick, G. N., and Bonorchis, D. (2004). Scaling aspects of quadrangular plates subjected to localised blast loads - Experiments and predictions. *International Journal of Impact Engineering*, 30(8):1179–1208.

Jahsman, W. (1958). Propagation of abrupt circular wave fronts in elastic sheets and plates. In *3rd US National Congress of Applied Mechanics*, pages 195–202, Brown University, Rhode Island, USA.

Jarrett, D. (1968). Derivation of the british explosives safety distances. *Annals of the New York Academy of Sciences*, 152(1):18–35.

Jones, N. (1971). A theoretical study of the dynamic plastic behavior of beams and plates with finite-deflections. *International Journal of Solids and Structures*, 7(8):1007–1029.

Jones, N. (1997). *Structural impact*. Cambridge University Press, Cambridge, UK.

Jureńczyk, Ł. (2018). Pojednanie narodowe pod presją zamachów–złudne nadzieje na przełom w afganistanie w pierwszym kwartale 2018 roku. *Rocznik Bezpieczeństwa Międzynarodowego*, 12(2):115–124.

Keane, B. and Esper, P. (2009). Forensic investigation of blast damage to british buildings. 162(5):4–11.

Kelly, P. (2013). *Solid mechanics part ii: Engineering solid mechanics small strain*. The University of Auckland, Auckland, New Zealand.

Kinney, G. F. and Graham, K. J. (1985). *Explosive shocks in air*. Springer, NY, USA.

Langdon, G., Cantwell, W., Guan, Z., and Nurick, G. (2014). The response of polymeric composite structures to air-blast loading: a state-of-the-art. *International Materials Reviews*, 59(3):159–177.

Langdon, G., Gabriel, S., von Klemperer, C., and Yuen, S. C. (2021). Transient response and failure of medium density fibreboard panels subjected to air-blast loading. *Composite Structures*, 273:114253.

Langdon, G., Yue, S. C. K., and Nurick, G. (2002). The response of stiffened square plates subjected to localised blast loading. *WIT Transactions on The Built Environment*, 63.

Langdon, G., Yuen, S. C. K., and Nurick, G. (2005). Experimental and numerical studies on the response of quadrangular stiffened plates. part ii: localised blast loading. *International Journal of Impact Engineering*, 31(1):85–111.

Langdon, G. S., Lee, W. C., and Louca, L. A. (2015). The influence of material type on the response of plates to air-blast loading. *International Journal of Impact Engineering*, 78:150–160.

Langran-Wheeler, C., Rigby, S., Clarke, S. D., Tyas, A., Stephens, C., and Walker, R. (2021). Near-field spatial and temporal blast pressure distributions from non-spherical charges: Horizontally-aligned cylinders. *International Journal of Protective Structures*, 12(4):492–516.

Langtangen, H. and Linge, S. (2017). *Finite difference computing with PDEs: a modern software approach*. Springer Nature, London, UK.

Lee, Y. and Wierzbicki, T. (2005a). Fracture prediction of thin plates under localized impulsive loading. part ii: discing and petalling. *International Journal of Impact Engineering*, 31(10):1277–1308.

Lee, Y. W. and Wierzbicki, T. (2005b). Fracture prediction of thin plates under localized impulsive loading. Part I: Dishing. *International Journal of Impact Engineering*, 31(10):1253–1276.

Lee, Y. W. and Wierzbicki, T. (2005c). Fracture prediction of thin plates under localized impulsive loading. Part II: Discing and Petalling. *International Journal of Impact Engineering*, 31(10):1277–1308.

Leissa, A. (1969). Vibration of plates. Technical Report NASA SP-160, National Aeronautics and Space Administration, Washington DC, USA.

Leonard, R. W. and Budiansky, B. (1955). On travelling waves in beams. Technical Report Report 1173, National Advisory Committee for Aeronautics, California, USA.

Li, Q. and Meng, H. (2002). Pressure-impulse diagram for blast loads based on dimensional analysis and single-degree-of-freedom model. *Journal of engineering mechanics*, 128(1):87–92.

Li, X., Yin, J., Zhao, P., Zhang, L., Xu, Y., Wang, Q., and Zhang, P. (2020). The effect of stand-off distance on damage to clamped square steel plates under enclosed explosion. *Structures*, 25:965–978.

Lomazzi, L., Giglio, M., and Manes, A. (2021). Analytical and empirical methods for the characterisation of the permanent transverse displacement of quadrangular metal plates subjected to blast load: comparison of existing methods and development of a novel methodological approach. *International Journal of Impact Engineering*, 154:103890.

LSTC, L. S. T. C. (2021). *LS-DYNA Keywords File*. Livermore Software Technology Corporation.

McDonald, B., Bornstein, H., Langdon, G., Curry, R., and Orifici, A. (2017). Deformation and rupture of armour grade steel under localised blast loading. *Procedia Engineering*, 197:13–22.

McDonald, B., Bornstein, H., Langdon, G. S., Curry, R., Daliri, A., and Orifici, A. C. (2018). Experimental response of high strength steels to localised blast loading. *International Journal of Impact Engineering*, 115(October 2017):106–119.

Mehreganian, N., Fallah, A., and Louca, L. (2018). Dynamic performance of simply supported rigid-plastic square plates subject to localized blast loading. *Journal of Engineering Mechanics*, 145(1):04018127.

Mehreganian, N., Fallah, A., and Louca, L. (2019a). Plastic dynamic response of simply supported thick square plates subject to localised blast loading. *International Journal of Impact Engineering*, 126:85–100.

Mehreganian, N., Fallah, A., and Louca, L. (2019b). Plastic dynamic response of simply supported thick square plates subject to localised blast loading. *International Journal of Impact Engineering*, 126:85–100.

Mendes, S. and Opat, H. (1973). Tearing and shear failures in explosively loaded clamped beams. *Exp. Mech*, 13:480–486.

Micallef, K., Fallah, A., Curtis, P., and Louca, L. (2016). On the dynamic plastic response of steel membranes subjected to localised blast loading. *International Journal of Impact Engineering*, 89:25–37.

Micallef, K., Fallah, A., Pope, D., and Louca, L. (2012). The dynamic performance of simply-supported rigid-plastic circular steel plates subjected to localised blast loading. *International Journal of Mechanical Sciences*, 65(1):177–191.

Micallef, K., Fallah, A., Pope, D., and Louca, L. (2014). Dynamic performance of simply supported rigid plastic circular thick steel plates subjected to localized blast loading. *Journal of Engineering Mechanics*, 140(1):159–171.

Mihailescu, S. and Wierzbicki, T. (2002). Wave solution for an impulsively loaded rigid-plastic circular membrane. *Archives of Mechanics*, 54(5-6):553–575.

Mindlin, R. (1951). Influence of rotatory inertia and shear on flexural motions of isotropic, elastic plates. *Journal of Applied Mechanics*, 18(1):31–38.

Minh Thanh, V., Santosa, S. P., Widagdo, D., and Putra, I. S. (2016). Steel plate behavior under blast loading-numerical approach using Ls-Dyna. *Applied Mechanics and Materials*, 842:200–207.

Mohammadzadeh, B. and Noh, H. C. (2019). An analytical and numerical investigation on the dynamic responses of steel plates considering the blast loads. *International Journal of Steel Structures*, 19(2):603–617.

Moriello, D., Bosi, F., Torii, R., and Tan, P. (2020). Failure and detachment path of impulsively loaded plates. *Thin-Walled Structures*, 155:106871.

Mostofi, T., Babaei, H., and Alitavoli, M. (2016). Theoretical analysis on the effect of uniform and localized impulsive loading on the dynamic plastic behaviour of fully clamped thin quadrangular plates. *Thin-Walled Structures*, 109:367–376.

Nagesh, C. and Gupta, N. (2022). Large deformations and failure of clamped circular steel plates under uniform impulsive loads using various phenomenological damage models. *International Journal of Impact Engineering*, 166:104255.

Neto, L., Saleh, M., Pickerd, V., Yiannakopoulos, G., Mathys, Z., and Reid, W. (2018). Rapid assessment of structures subjected to localised blast. In *25th International Symposium on Military Aspects of Blast and Shock*, The Hague, The Netherlands.

Nurick, G., Gelman, M., and Marshall, N. (1996). Tearing of blast loaded plates with clamped boundary conditions. *International Journal of Impact Engineering*, 18(7-8):803–827.

Nurick, G. and Radford, A. (1997). Deformation and tearing of clamped circular plates subjected to localised central blast loads. *Recent development in computational and applied mechanics*, 1(1):276–301.

Nurick, G. N. and Martin, J. B. (1989a). Deformation of thin plates subjected to impulsive loading- a review: Part I: theoretical considerations. *International Journal of Impact Engineering*, 8(2):159–170.

Nurick, G. N. and Martin, J. B. (1989b). Deformation of thin plates subjected to impulsive loading-a review Part II: Experimental studies. *International Journal of Impact Engineering*, 8(2):171–186.

Nurick, G. N. and Shave, G. C. (1996). The deformation and tearing of thin square plates subjected to impulsive loads—an experimental study. *International Journal of Impact Engineering*, 18:99–116.

Özişik, M., Orlande, H., Colaco, M., and Cotta, R. M. (2017). *Finite difference methods in heat transfer*. CRC press, NY, USA.

Pannell, J., Panoutsos, G., Cooke, S., Pope, D., and Rigby, S. E. (2021). Predicting specific impulse distributions for spherical explosives in the extreme near-field using a gaussian function. *International Journal of Protective Structures*, 12:2041419621993492.

Reissner, E. (1945). The effect of transverse shear deformation on the bending of elastic plates. *Journal of Applied Mechanics*, 12(2):A69–A77.

Rezasefat, M., M.T., M., Babaei, H., Ziya-Shamami, M., and Alitavoli, M. (2019). Dynamic plastic response of double-layered circular metallic plates due to localized impulsive loading. *Proceedings of the Institution of Mechanical Engineers, Part L: Journal of Materials: Design and Applications*, 233(7):1449–1471.

Rigby, S., Akintaro, O., Fuller, B., Tyas, A., Curry, R., Langdon, G., and Pope, D. (2019a). Predicting the response of plates subjected to near-field explosions using an energy equivalent impulse. *International Journal of Impact Engineering*, 8(2):171–186.

Rigby, S., Fay, S., Tyas, A., Clarke, S., Reay, J., Warren, J., Gant, M., and Elgy, I. (2018). Influence of particle size distribution on the blast pressure profile from explosives buried in saturated soils. *Shock Waves*, 28(3):613–626.

Rigby, S., Osborne, C., Langdon, G., Cooke, S., and Pope, D. (2021). Spherical equivalence of cylindrical explosives: Effect of charge shape on deflection of blast-loaded plates. *International Journal of Impact Engineering*, 155:103892.

Rigby, S., Tyas, A., Curry, R., and Langdon, G. (2019b). Experimental measurement of specific impulse distribution and transient deformation of plates subjected to near-field explosive blasts. *Experimental Mechanics*, 59(2):163–178.

Rigby, S. E. and Tyas, A. (2021). *Blast and Impact Effects on Structures CIV 4415/6415 Course Notes*. University of Sheffield, UK.

Rudrapatna, N., Vaziri, R., and Olson, M. (1999). Deformation and failure of blast-loaded square plates. *International journal of impact engineering*, 22(4):449–467.

Saeed Ahmad, M., Langdon, G. S., Nurick, G. N., and Chung Kim Yuen, S. (2018). A study on the response of single and double circular plates subjected to localised blast loading. *Latin American Journal of Solids and Structures*, 15(11):1679–7817.

Savović, S., Drljača, B., and Djordjevich, A. (2022). A comparative study of two different finite difference methods for solving advection–diffusion reaction equation for modeling exponential traveling wave in heat and mass transfer processes. *Ricerche di Matematica*, 71(1):245–252.

Shokrieh, M. and Karamnejad, A. (2014). Investigation of strain rate effects on the dynamic response of a glass/epoxy composite plate under blast loading by using the finite-difference method. *Mechanics of Composite Materials*, 50(3):295–310.

Shrestha, R. and Fluri, J. (2023). Geopolitics of security and surveillance in nepal and afghanistan: A comparative analysis. *Environment and Planning C: Politics and Space*, 41(1):92–108.

Shuaib, M., Yuen, S., and Nurick, G. (2016). Numerical simulation of blast loaded cfrp retrofitted steel plates. *Journal of Performance of Constructed Facilities*, 30(5):305–317.

Spillers, W. (1965). Wave propagation in a thin cylindrical shelg. *Journal of Applied Mechanics*, 32:346–350.

Sun, N.-Z. (1996). Finite difference methods and the method of characteristics for solving hydrodynamic dispersion equations. In *Mathematical Modeling of Groundwater Pollution*, pages 73–96, New York, NY, USA.

Symonds, P. and Wierzbicki, T. (2019). Membrane mode solutions for impulsively loaded circular plates. *Journal of Applied Mechanics*, 46(1):58–64.

Teeling-Smith, R. and Nurick, G. (1991a). The deformation and tearing of thin circular plates subjected to impulsive loads. *International Journal of Impact Engineering*, 11(1):77–91.

Teeling-Smith, R. G. and Nurick, G. N. (1991b). The deformation and tearing of thin circular plates subjected to impulsive loads. *International Journal of Impact Engineering*, 11(1):77–91.

Timoshenko, S. and Woinowsky-Krieger, S. (1959). *Theory of plates and shells*, volume 2. McGraw-hill, NY, USA.

Tresca, H. (1878). On the flow and rupture of metals. *Proceedings of the Royal Society of London*, 27:538–540.

Tyas, A. (2014). *Blast and Impact Loading on Structures*. University of Sheffield, UK.

Tyas, A. and Pope, D. J. (2003). The energy take-up of panels subjected to near-field blast loading. In *International Conference on the Response of Structures to Extreme Loading*. Toronto, Canada.

Ugural, A. (1999). *Stresses in plates and shells*. McGraw-Hill Science, Engineering & Mathematics, NY, USA.

US Department of Defence (2008). *Structures to resist the effects of accidental explosions*. TUS DoD, Washington DC, USA, UFC-3-340-02.

V., E. S. and Krauthammer, T. (2001). *Thin plates and shells: theory, analysis, and applications*. Marcel Dekker, NY, USA.

Wang, M., Feng, Y., Zhong, W., and Qiu, X. (2022). The equivalent method for arbitrary pulses loaded on the elastic-brittle panel. *International Journal of Impact Engineering*, 167:104278.

Wierzbicki, T. and Nurick, G. (1996). Large deformation of thin plates under localised impulsive loading. *International Journal of Impact Engineering*, 18(7-8):899–918.

Wierzbičk, T. and J., S. (1983). Wave solution for an impulsively loaded right plastic circular membrane. *International Journal of Solids and Structures*, 19(11):1005–1012.

Xing, Y. and Liu, B. (2009a). Characteristic equations and closed-form solutions for free vibrations of rectangular mindlin plates. *Acta Mechanica Solida Sinica*, 22(2):125–136.

Xing, Y. and Liu, B. (2009b). Closed form solutions for free vibrations of rectangular mindlin plates. *Acta Mechanica Sinica*, 25(5):689–698.

Xu, Z., Liu, Y., and Huang, F. (2019). Deformation and failure of thin plate structures under blast loading. *Advances in Mechanical Engineering*, 11(1):1–10.

Yuen, S. and Nurick, G. (2000). The significance of the thickness of a plate when subjected to localised blast loads. *Blast Impact Load. Struct*, 1:471–499.

Yuen, S., Nurick, G., Langdon, G., and Iyer, Y. (2017). Deformation of thin plates subjected to impulsive load: Part iii–an update 25 years on. *International Journal of Impact Engineering*, 107:108–117.

Yuen, S. C. and Nurick, G. (2005). Experimental and numerical studies on the response of quadrangular stiffened plates. part i: subjected to uniform blast load. *International Journal of Impact Engineering*, 31(1):55–83.

Yuen, S. C. K., Langdon, G., Nurick, G., Pickering, E., and Balden, V. (2012). Response of v-shape plates to localised blast load: Experiments and numerical simulation. *International journal of impact engineering*, 46:97–109.

Zakrisson, B. (2013). *Numerical simulations of blast loaded steel plates for improved vehicle protection*. PhD thesis, Luleå University of Technology.

Zhang, X., Hao, H., and Ma, G. (2013). Parametric study of laminated glass window response to blast loads. *Engineering Structures*, 56:1707–1717.

Appendix A

Matlab Scripts

A.1 Theoretical Stress Prediction

```
%E=6.83E9;% Young modulus,unit=N/m2 LN
E=4.78E9;% Young modulus,unit=N/m2  PMMA
%G=2.73E9;% Shear modulus,unit=N/m2 LN
G=1.91E9;% Shear modulus,unit=N/m2 PMMA
thickness=0.635E-2; %unit=m
Possion_ratio=0.25;
D=(E*(thickness.^3))/(12*(1-Possion_ratio.^2));
%pho=1.35E3; %density,unit=kg/m3
pho=1.18E3; %density,unit=kg/m3
de=1.52E-2; % unit=m
%diameter=5.08E-2;      % unit=m
diameter=5.08E-2;      % unit=m
r1=(diameter-de)/2;% unit=m
r2=(diameter+de)/2;% unit=m
k=0.76+0.3*Possion_ratio;
cp=sqrt(E/(pho*(1-Possion_ratio^2)))
cs=sqrt(k*G/pho);
```

```
beta=cp/cs
%impulseintensity=450; %unit N*s/m2
impulseintensity=690; %unit N*s/m2
Vmax=impulseintensity/(pho*thickness); %velcity, unit m/s
nonVmax=Vmax*sqrt(12)/(beta*cp) % nondimensional peak
   constant velocity
nonr1=r1*sqrt(12)/thickness;
nonr2=r2*sqrt(12)/thickness;
nonde=de*sqrt(12)/thickness;
%fracturestress=7.8E+7; %unit=N/m2 Material strength
fracturestress=8.4E+7; %unit=N/m2 Material strength
Fracturecriterion=fracturestress*(thickness.^2)/6; % maximum
    M and N
nonFracturecriterionforM=Fracturecriterion*thickness/D
nonFracturecriterionforN=Fracturecriterion*thickness/(
   Possion_ratio*D);
%fractureM=fracturestress.*(thickness.^2)/6;
%fractureN=fracturestress.*(thickness.^2)/6;

tmax=100E-6; % maximum time
dt=0.2E-6; % unit=s time step
nontmax=tmax*cp*sqrt(12)/thickness; % maximum nondimensional
    time =113.398
nondt=dt*cp*sqrt(12)/thickness % nondimensional dt
                =0.2268

n=round(nontmax/(2*nondt))          % number of
   nondimensional time step 2nondt interval n=250
rmax=8.5/2*2.54/100; % unsupported total radius unit=m
nonrmax=rmax*sqrt(12)/thickness % maximum nondimensional
   coordinate           =58.889
m=floor(nonrmax/(2*nondt))          % number of
   nondimensional space step 2nondt interval 129
% nondradius=nonrmax/m; % nondimensional space step
% nondradius=0.5; % nondimensional space step
```

```
% n=30; % number of nondimensional space steps
% nondradius=nonrmax/n; % nondimensional space step length

nonr=[];
nonV=[];
nonQ=[];
nonM=[];
nonP=[];
nonN=[];
nonW=[];
nont=[];
f1=[];
f2=[];
f3=[];
f4=[];
f5=[];
F1=[];
F2=[];
F3=[];
F4=[];
F5=[];
afa=(1-Possion_ratio.^2)/Possion_ratio;
%nonY=[];

for j=1:(n*2+1)
for i=1:(m+1)
nont(i,j)=(j-1)*nondt;
end
end


% nonradius axis nondt=0
for i=1:ceil((nonr2/(2*nondt)))

nonW(i,1)=0;
```

```
nonM(i,1)=0;
nonQ(i,1)=0;
nonN(i,1)=0;
nonP(i,1)=0;

nonr(i,1)=(i-1)*2*nondt;
%nonY(i,1)=0;
end
% zero point
for i=(ceil((nonr2/(2*nondt)))+1):(m+1)
nonr(i,1)=(i-1)*2*nondt;
end

%Initial condition  initial nondimensional velocity

for i=1:(m+1)
if i<=ceil((nonr1/(2*nondt)))
nonV(i,1)=nonVmax;
elseif i>ceil((nonr1/(2*nondt))) && i<=ceil((nonr2/(2*nondt)
   ))
nonV(i,1)=(-nonVmax/(nonr2-nonr1))*(i-1)*2*nondt-nonr2*(-
   nonVmax/(nonr2-nonr1));
else
nonV(i,1)=0;
end


end

% General point(2nd row)

% point(1,2)
nonr(1,2)=nondt;
f1(1,2)=0;
f2(1,2)=0;
```

```
%f3(1,2)=-nonV(1,1);
f3(1,2)=-nonV(1,1)+(nonV(2,1)-nonV(1,1))*(3-5*beta)/(8*beta)
   ;
%f4(1,2)=nonV(1,1);
f4(1,2)=nonV(1,1)+(nonV(2,1)-nonV(1,1))*(3+5*beta)/(8*beta);
f5(1,2)=0;
F1(1,2)=f1(1,2)+f2(1,2);
F2(1,2)=f2(1,2)-1/2*(f1(1,2)+f2(1,2))+Possion_ratio*nondt
   /(2*nonr(1,2))*(f5(1,2)+afa/(2*Possion_ratio)*(f1(1,2)+f2
   (1,2)))-nondt/4*(f3(1,2)+f4(1,2))+(Possion_ratio-1)/
   Possion_ratio*nondt/(4*nonr(1,2))*(f1(1,2)+f2(1,2));
F3(1,2)=f3(1,2)+f4(1,2);
F4(1,2)=f4(1,2)-1/2*(f3(1,2)+f4(1,2));
F5(1,2)=f5(1,2)+afa/(2*Possion_ratio)*(f1(1,2)+f2(1,2));
nonW(1,2)=F2(1,2)/(-1-(nondt.^2)/4*(1/(beta.^2)-(
   Possion_ratio-1)/(nonr(1,2).^2)));
nonM(1,2)=1/2*(F1(1,2)-Possion_ratio*nondt/nonr(1,2)*nonW
   (1,2));
nonQ(1,2)=1/2*(F3(1,2)-nondt/(beta.^2)*nonW(1,2));
nonV(1,2)=F4(1,2)+nondt/(2*beta*nonr(1,2))*nonQ(1,2);
nonN(1,2)=(1+afa/Possion_ratio)*nonM(1,2)-F5(1,2);
nonP(1,2)=0;
%nonY(1,2)=nondt*beta/4*(nonV(1,1)+2*nonV(1,2)+nonV(2,1))
   -0.5*(nonY(1,1)+nonY(2,1));

for i=2:(ceil((nonr2/(2*nondt)))-1)
nonP(i,2)=0;
nonr(i,2)=(2*i-1)*nondt;

f1(i,2)=nonM(i,1) + nonW(i,1) - (nondt*((nonM(i,1) - nonN(i
   ,1)*Possion_ratio)/nonr(i,1) - nonQ(i,1) + (Possion_ratio
   *nonW(i,1))/nonr(i,1)))/2;
f2(i,2)=nonM(i+1,1) - nonW(i+1,1) - (nondt*(nonQ(i+1,1) - (
   nonM(i+1,1) - nonN(i+1,1)*Possion_ratio)/nonr(i+1,1) + (
   Possion_ratio*nonW(i+1,1))/nonr(i+1,1)))/2;
```

```
f3(i,2)=nonQ(i,1) - nonV(i,1) - (nondt*((nonW(i,1) - ((nonW(
   i,1) - nonW(i+1,1))*(beta - 1))/(2*beta))/beta^2 + (nonQ(
   i,1)/nonr(i,1) - ((nonQ(i,1)/nonr(i,1) - nonQ(i+1,1)/nonr
   (i+1,1))*(beta - 1))/(2*beta))/beta))/2 - ((nonQ(i,1) -
   nonQ(i+1,1))*(beta - 1))/(2*beta) + ((nonV(i,1) - nonV(i
   +1,1))*(beta - 1))/(2*beta);
f4(i,2)=nonQ(i,1) + nonV(i,1) - (nondt*((nonW(i,1) - ((nonW(
   i,1) - nonW(i+1,1))*(beta + 1))/(2*beta))/beta^2 - (nonQ(
   i,1)/nonr(i,1) - ((nonQ(i,1)/nonr(i,1) - nonQ(i+1,1)/nonr
   (i+1,1))*(beta + 1))/(2*beta))/beta))/2 - ((nonQ(i,1) -
   nonQ(i+1,1))*(beta + 1))/(2*beta) - ((nonV(i,1)- nonV(i
   +1,1))*(beta + 1))/(2*beta);
f5(i,2)=nonM(i,1)/2 + nonM(i+1,1)/2 - nonN(i,1)/2 - nonN(i
   +1,1)/2 + (afa*nondt*(nonW(i,1)/(2*nonr(i,1)) + nonW(i
   +1,1)/(2*nonr(i+1,1))))/2;
F1(i,2)=f1(i,2)+f2(i,2);
F2(i,2)=f2(i,2)-0.5*(f1(i,2)+f2(i,2))+Possion_ratio*nondt
   /(2*nonr(i,2))*(f5(i,2)+afa/(2*Possion_ratio)*(f1(i,2)+f2
   (i,2)))-nondt/4*(f3(i,2)+f4(i,2))+(Possion_ratio-1)/
   Possion_ratio*nondt/(4*nonr(i,2))*(f1(i,2)+f2(i,2));
F3(i,2)=f3(i,2)+f4(i,2);
F4(i,2)=f4(i,2)-0.5*(f3(i,2)+f4(i,2));
F5(i,2)=f5(i,2)+afa/(2*Possion_ratio)*(f1(i,2)+f2(i,2));

nonW(i,2)=F2(i,2)/(-1-(nondt.^2)/4*(1/(beta.^2)-(
   Possion_ratio-1)/(nonr(i,2).^2)));
nonM(i,2)=0.5*(F1(i,2)-Possion_ratio*nondt/nonr(i,2)*nonW(i
   ,2));
nonQ(i,2)=0.5*(F3(i,2)-nondt/(beta.^2)*nonW(i,2));
nonV(i,2)=F4(i,2)+nondt/(2*beta*nonr(i,2))*nonQ(i,2);
nonN(i,2)=(1+afa/Possion_ratio)*nonM(i,2)-F5(i,2);
%nonY(i,2)=nondt*beta/4*(nonV(i,1)+2*nonV(i,2)+nonV(i+1,1))
   -0.5*(nonY(i,1)+nonY(i+1,1));
end
nonP(ceil((nonr2/(2*nondt))),2)=0;
```

```
nonQ(ceil((nonr2/(2*nondt))),2)=0;
nonW(ceil((nonr2/(2*nondt))),2)=0;
nonM(ceil((nonr2/(2*nondt))),2)=0;
nonV(ceil((nonr2/(2*nondt))),2)=0;
nonN(ceil((nonr2/(2*nondt))),2)=0;
nonr(ceil((nonr2/(2*nondt))),2)=(2*ceil((nonr2/(2*nondt)))
   -1)*nondt;
nonY(ceil((nonr2/(2*nondt))),2)=0;

nnn=ceil((nonr2/(2*nondt)));

% General point (3nd row)

for j=3:(n*2+1)
if mod(j,2)==0 && j<((m+1-ceil((nonr2/(2*nondt))))*2+2)
% first point
nonP(1,j)=0;
nonr(1,j)=nondt;

f1(1,j)=nonM(1,j-1) + Possion_ratio/(4*(1+Possion_ratio))*(
   nonM(2,j-1)-nonM(1,j-1));
f2(1,j)=nonM(2,j-1) - nonW(2,j-1) - (nondt*(nonQ(2,j-1) - (
   nonM(2,j-1) - nonN(2,j-1)*Possion_ratio)/nonr(2,j-1) + (
   Possion_ratio*nonW(2,j-1))/nonr(2,j-1)))/2;
f3(1,j)=-nonV(1,j-1)-nondt*((nonW(2,j-1)*(beta-1))/(2*beta
   .^3)+(nonV(2,j-1)-nonV(1,j-1))/(4*nondt)-(beta-1)/(2*beta
   .^2)*(1/4*beta*(nonV(2,j-1)-nonV(1,j-1))/nondt-nonQ(2,j
   -1)/nonr(2,j-1)))+nonQ(2,j-1)*(beta-1)/(2*beta)+(nonV(1,j
   -1)-nonV(2,j-1))*(beta-1)/(2*beta);
f4(1,j)=nonV(1,j-1)-nondt*(nonW(2,j-1)*(beta+1)/(2*beta.^3)
   -(nonV(2,j-1)-nonV(1,j-1))/(4*nondt)+(beta+1)/(2*beta.^2)
   *(1/4*beta*(nonV(2,j-1)-nonV(1,j-1))/nondt-nonQ(2,j-1)/
   nonr(2,j-1)))+nonQ(2,j-1)*(beta+1)/(2*beta)-(nonV(1,j-1)-
   nonV(2,j-1))*(beta+1)/(2*beta);
```

```
f5(1,j)=nonM(1,j-1)/2 + nonM(2,j-1)/2 - nonN(1,j-1)/2 - nonN
   (2,j-1)/2 + 0.25*afa*nondt*((nonM(1,j-1)-nonM(2,j-1))
   /(2*(1+Possion_ratio)*nondt)+nonW(2,j-1)/nonr(2,j-1));
F1(1,j)=f1(1,j)+f2(1,j);
F2(1,j)=f2(1,j)-0.5*(f1(1,j)+f2(1,j))+Possion_ratio*nondt
   /(2*nonr(1,j))*(f5(1,j)+afa/(2*Possion_ratio)*(f1(1,j)+f2
   (1,j)))-nondt/4*(f3(1,j)+f4(1,j))+(Possion_ratio-1)/
   Possion_ratio*nondt/(4*nonr(1,j))*(f1(1,j)+f2(1,j));
F3(1,j)=f3(1,j)+f4(1,j);
F4(1,j)=f4(1,j)-0.5*(f3(1,j)+f4(1,j));
F5(1,j)=f5(1,j)+afa/(2*Possion_ratio)*(f1(1,j)+f2(1,j));
nonW(1,j)=F2(1,j)/(-1-(nondt.^2)/4*(1/(beta.^2)-(
   Possion_ratio-1)/(nonr(1,j).^2)));
nonM(1,j)=0.5*(F1(1,j)-Possion_ratio*nondt/nonr(1,j)*nonW(1,
   j));
nonQ(1,j)=0.5*(F3(1,j)-nondt/(beta.^2)*nonW(1,j));
nonV(1,j)=F4(1,j)+nondt/(2*beta*nonr(1,j))*nonQ(1,j);
nonN(1,j)=(1+afa/Possion_ratio)*nonM(1,j)-F5(1,j);
nonP(1,j)=0;
%nonY(1,j)=nondt*beta/4*(nonV(1,j)+2*nonV(i,2)+nonV(i+1,1))
   -0.5*(nonY(i,1)+nonY(i+1,1));

for  i=2:nnn
nonP(i,j)=0;
nonr(i,j)=(2*i-1)*nondt;

f1(i,j)=nonM(i,j-1) + nonW(i,j-1) - (nondt*((nonM(i,j-1) -
   nonN(i,j-1)*Possion_ratio)/nonr(i,j-1) - nonQ(i,j-1) + (
   Possion_ratio*nonW(i,j-1))/nonr(i,j-1)))/2;
f2(i,j)=nonM(i+1,j-1) - nonW(i+1,j-1) - (nondt*(nonQ(i+1,j
   -1) - (nonM(i+1,j-1) - nonN(i+1,j-1)*Possion_ratio)/nonr(
   i+1,j-1) + (Possion_ratio*nonW(i+1,j-1))/nonr(i+1,j-1)))
   /2;
f3(i,j)=nonQ(i,j-1) - nonV(i,j-1) - (nondt*((nonW(i,j-1) -
   ((nonW(i,j-1) - nonW(i+1,j-1))*(beta - 1))/(2*beta))/beta
```

```
   ^2 + (nonQ(i,j-1)/nonr(i,j-1) - ((nonQ(i,j-1)/nonr(i,j-1)
    - nonQ(i+1,j-1)/nonr(i+1,j-1))*(beta - 1))/(2*beta))/
   beta))/2 - ((nonQ(i,j-1) - nonQ(i+1,j-1))*(beta - 1))/(2*
   beta) + ((nonV(i,j-1) - nonV(i+1,j-1))*(beta - 1))/(2*
   beta);
f4(i,j)=nonQ(i,j-1) + nonV(i,j-1) - (nondt*((nonW(i,j-1) -
   ((nonW(i,j-1) - nonW(i+1,j-1))*(beta + 1))/(2*beta))/beta
   ^2 - (nonQ(i,j-1)/nonr(i,j-1) - ((nonQ(i,j-1)/nonr(i,j-1)
    - nonQ(i+1,j-1)/nonr(i+1,j-1))*(beta + 1))/(2*beta))/
   beta))/2 - ((nonQ(i,j-1) - nonQ(i+1,j-1))*(beta + 1))/(2*
   beta) - ((nonV(i,j-1)- nonV(i+1,j-1))*(beta + 1))/(2*beta
   );
f5(i,j)=nonM(i,j-1)/2 + nonM(i+1,j-1)/2 - nonN(i,j-1)/2 -
   nonN(i+1,j-1)/2 + (afa*nondt*(nonW(i,j-1)/(2*nonr(i,j-1))
    + nonW(i+1,j-1)/(2*nonr(i+1,j-1))))/2;

F1(i,j)=f1(i,j)+f2(i,j);
F2(i,j)=f2(i,j)-0.5*(f1(i,j)+f2(i,j))+Possion_ratio*nondt
   /(2*nonr(i,j))*(f5(i,j)+afa/(2*Possion_ratio)*(f1(i,j)+f2
   (i,j)))-nondt/4*(f3(i,j)+f4(i,j))+(Possion_ratio-1)/
   Possion_ratio*nondt/(4*nonr(i,j))*(f1(i,j)+f2(i,j));
F3(i,j)=f3(i,j)+f4(i,j);
F4(i,j)=f4(i,j)-0.5*(f3(i,j)+f4(i,j));
F5(i,j)=f5(i,j)+afa/(2*Possion_ratio)*(f1(i,j)+f2(i,j));

nonW(i,j)=F2(i,j)/(-1-(nondt.^2)/4*(1/(beta.^2)-(
   Possion_ratio-1)/(nonr(i,j).^2)));
nonM(i,j)=0.5*(F1(i,j)-Possion_ratio*nondt/nonr(i,j)*nonW(i,
   j));
nonQ(i,j)=0.5*(F3(i,j)-nondt/(beta.^2)*nonW(i,j));
nonV(i,j)=F4(i,j)+nondt/(2*beta*nonr(i,j))*nonQ(i,j);
nonN(i,j)=(1+afa/Possion_ratio)*nonM(i,j)-F5(i,j);
% nonyA=0.5*(nonyB+nonyF)+nondt/4*(nonV(i,1)+2*nonvA+nonr(i
   +1,1));
end
```

```
wert=1;

elseif mod(j,2)==1 && j<=((m+1-ceil((nonr2/(2*nondt))))*2+1)
for i=2:nnn
nonP(i,j)=0;
nonr(i,j)=(i-1)*2*nondt;

f1(i,j)=nonM(i-1,j-1) + nonW(i-1,j-1) - (nondt*((nonM(i-1,j
   -1) - nonN(i-1,j-1)*Possion_ratio)/nonr(i-1,j-1) - nonQ(i
   -1,j-1) + (Possion_ratio*nonW(i-1,j-1))/nonr(i-1,j-1)))
   /2;
f2(i,j)=nonM(i,j-1) - nonW(i,j-1) - (nondt*(nonQ(i,j-1) - (
   nonM(i,j-1) - nonN(i,j-1)*Possion_ratio)/nonr(i,j-1) + (
   Possion_ratio*nonW(i,j-1))/nonr(i,j-1)))/2;
f3(i,j)=nonQ(i-1,j-1) - nonV(i-1,j-1) - (nondt*((nonW(i-1,j
   -1) - ((nonW(i-1,j-1) - nonW(i,j-1))*(beta - 1))/(2*beta)
   )/beta^2 + (nonQ(i-1,j-1)/nonr(i-1,j-1) - ((nonQ(i-1,j-1)
   /nonr(i-1,j-1) - nonQ(i,j-1)/nonr(i,j-1))*(beta - 1))/(2*
   beta))/beta))/2 - ((nonQ(i-1,j-1) - nonQ(i,j-1))*(beta -
   1))/(2*beta) + ((nonV(i-1,j-1) - nonV(i,j-1))*(beta - 1))
   /(2*beta);
f4(i,j)=nonQ(i-1,j-1) + nonV(i-1,j-1) - (nondt*((nonW(i-1,j
   -1) - ((nonW(i-1,j-1) - nonW(i,j-1))*(beta + 1))/(2*beta)
   )/beta^2 - (nonQ(i-1,j-1)/nonr(i-1,j-1) - ((nonQ(i-1,j-1)
   /nonr(i-1,j-1) - nonQ(i,j-1)/nonr(i,j-1))*(beta + 1))/(2*
   beta))/beta))/2 - ((nonQ(i-1,j-1) - nonQ(i,j-1))*(beta +
   1))/(2*beta) - ((nonV(i-1,j-1)- nonV(i,j-1))*(beta + 1))
   /(2*beta);
f5(i,j)=nonM(i-1,j-1)/2 + nonM(i,j-1)/2 - nonN(i-1,j-1)/2 -
   nonN(i,j-1)/2 + (afa*nondt*(nonW(i-1,j-1)/(2*nonr(i-1,j
   -1)) + nonW(i,j-1)/(2*nonr(i,j-1))))/2;

F1(i,j)=f1(i,j)+f2(i,j);
```

```
F2(i,j)=f2(i,j)-0.5*(f1(i,j)+f2(i,j))+Possion_ratio*nondt
   /(2*nonr(i,j))*(f5(i,j)+afa/(2*Possion_ratio)*(f1(i,j)+f2
   (i,j)))-nondt/4*(f3(i,j)+f4(i,j))+(Possion_ratio-1)/
   Possion_ratio*nondt/(4*nonr(i,j))*(f1(i,j)+f2(i,j));
F3(i,j)=f3(i,j)+f4(i,j);
F4(i,j)=f4(i,j)-0.5*(f3(i,j)+f4(i,j));
F5(i,j)=f5(i,j)+afa/(2*Possion_ratio)*(f1(i,j)+f2(i,j));

nonW(i,j)=F2(i,j)/(-1-(nondt.^2)/4*(1/(beta.^2)-(
   Possion_ratio-1)/(nonr(i,j).^2)));
nonM(i,j)=1/2*(F1(i,j)-Possion_ratio*nondt/nonr(i,j)*nonW(i,
   j));
nonQ(i,j)=1/2*(F3(i,j)-nondt/(beta.^2)*nonW(i,j));
nonV(i,j)=F4(i,j)+nondt/(2*beta*nonr(i,j))*nonQ(i,j);
nonN(i,j)=(1+afa/Possion_ratio)*nonM(i,j)-F5(i,j);
% nonyA=0.5*(nonyB+nonyF)+nondt/4*(nonV(i,1)+2*nonvA+nonr(i
   +1,1));

% origin point
nonP(1,j)=0;
nonQ(1,j)=0;
nonW(1,j)=0;
%nonM(1,j)=4*(1+Possion_ratio)/(4+Possion_ratio*(4-sqrt(12))
   )*((-Possion_ratio*sqrt(12))/(4*(1+Possion_ratio))*nonM
   (1,j-2)+(1+nondt/(2*nonr(1,j-1)))*nonM(1,j-1)-(1+
   Possion_ratio*nondt/(2*nonr(1,j-1)))*nonW(1,j-1)-nondt/2*
   nonQ(1,j-1)-Possion_ratio*nondt/(2*nonr(1,j-1))*nonN(1,j
   -1));
nonM(1,j)=(nonM(1,j-1)*(1+nondt/(2*nonr(1,j-1)))-nondt*
   Possion_ratio/(2*nonr(1,j-1))*nonN(1,j-1)-(1+
   Possion_ratio*nondt/(2*nonr(1,j-1)))*nonW(1,j-1)-0.5*
   nondt*nonQ(1,j-1)-Possion_ratio/(4*(1+Possion_ratio))*
   nonM(1,j-2))/((4+3*Possion_ratio)/(4+4*Possion_ratio));
if j==3
```

```
%nonV(1,j)=-(nonQ(1,j-1)/beta-nonV(1,j-2)/8+nonV(1,j-1)/beta
   +(nonV(1,j-2)*(beta - 1))/(2*beta)+(nondt*(nonQ(1,j-1)/(
   beta*nonr(1,j-1))-((beta - 1)*(nonP(1,j)/4+nonP(1,j-2)
   /4-0+(nonV(1,j-2)*beta)/(4*nondt)))/(2*beta)))/(2*beta)+(
   nondt*(nonP(1,j)+nonP(1,j-1)/beta+((beta - 1)*(nonP(1,j)+
   nonP(1,j-2)))/(2*beta)))/(2*beta)-(nonP(1,j)*nondt)/(8*
   beta)-(nonP(1,j-2)*nondt)/(8*beta)-(nonW(1,j-1)*nondt)
   /(2*beta^3))/((9*(beta - 1))/(16*beta)-7/8);
nonV(1,j)=(1/beta*nonQ(1,j-1)+1/beta*nonV(1,j-1)-nondt/(2*
   beta.^3)*nonW(1,j-1)+nondt/(2*beta.^2)*nonQ(1,j-1)/nonr
   (1,j-1)+(5*beta-7)/(16*beta)*nonV(1,j-2))/((5*beta+9)
   /(16*beta));
else
%nonV(1,j)=-(nonQ(1,j-1)/beta-nonV(1,j-2)/8+nonV(1,j-1)/beta
   +(nonV(1,j-2)*(beta - 1))/(2*beta)+(nondt*(nonQ(1,j-1)/(
   beta*nonr(1,j-1))-((beta - 1)*(nonP(1,j)/4+nonP(1,j-2)
   /4-0.25*(beta*(nonV(1,j-2)-nonV(1,j-4))/nondt-nonP(1,j-2)
   -nonP(1,j-4))+(nonV(1,j-2)*beta)/(4*nondt)))/(2*beta)))
   /(2*beta)+(nondt*(nonP(1,j)+nonP(1,j-1)/beta+((beta - 1)
   *(nonP(1,j)+nonP(1,j-2)))/(2*beta)))/(2*beta)-(nonP(1,j)*
   nondt)/(8*beta)-(nonP(1,j-2)*nondt)/(8*beta)-(nonW(1,j-1)
   *nondt)/(2*beta^3))/((9*(beta - 1))/(16*beta)-7/8);
nonV(1,j)=(1/beta*nonQ(1,j-1)+1/beta*nonV(1,j-1)-nondt/(2*
   beta.^3)*nonW(1,j-1)+nondt/(2*beta.^2)*nonQ(1,j-1)/nonr
   (1,j-1)+(3*beta-4)/(8*beta)*nonV(1,j-2)-(beta-1)/(16*beta
   )*nonV(1,j-4))/((5*beta+9)/(16*beta));
end
nonN(1,j)=1/Possion_ratio*nonM(1,j);
nonr(1,j)=0;

end

wert=2;

elseif mod(j,2)==0
```

```
% first point
nonP(1,j)=0;
nonr(1,j)=nondt;

f1(1,j)=nonM(1,j-1) + Possion_ratio/(4*(1+Possion_ratio))*(
   nonM(2,j-1)-nonM(1,j-1));
f2(1,j)=nonM(2,j-1) - nonW(2,j-1) - (nondt*(nonQ(2,j-1) - (
   nonM(2,j-1) - nonN(2,j-1)*Possion_ratio)/nonr(2,j-1) + (
   Possion_ratio*nonW(2,j-1))/nonr(2,j-1)))/2;
f3(1,j)=-nonV(1,j-1)-nondt*((nonW(2,j-1)*(beta-1))/(2*beta
   .^3)+(nonV(2,j-1)-nonV(1,j-1))/(4*nondt)-(beta-1)/(2*beta
   .^2)*(1/4*beta*(nonV(2,j-1)-nonV(1,j-1))/nondt-nonQ(2,j
   -1)/nonr(2,j-1)))+nonQ(2,j-1)*(beta-1)/(2*beta)+(nonV(1,j
   -1)-nonV(2,j-1))*(beta-1)/(2*beta);
f4(1,j)=nonV(1,j-1)-nondt*(nonW(2,j-1)*(beta+1)/(2*beta.^3)
   -(nonV(2,j-1)-nonV(1,j-1))/(4*nondt)+(beta+1)/(2*beta.^2)
   *(1/4*beta*(nonV(2,j-1)-nonV(1,j-1))/nondt-nonQ(2,j-1)/
   nonr(2,j-1)))+nonQ(2,j-1)*(beta+1)/(2*beta)-(nonV(1,j-1)-
   nonV(2,j-1))*(beta+1)/(2*beta);
f5(1,j)=nonM(1,j-1)/2 + nonM(2,j-1)/2 - nonN(1,j-1)/2 - nonN
   (2,j-1)/2 + 0.25*afa*nondt*((nonM(1,j-1)-nonM(2,j-1))
   /(2*(1+Possion_ratio)*nondt)+nonW(2,j-1)/nonr(2,j-1));
F1(1,j)=f1(1,j)+f2(1,j);
F2(1,j)=f2(1,j)-0.5*(f1(1,j)+f2(1,j))+Possion_ratio*nondt
   /(2*nonr(1,j))*(f5(1,j)+afa/(2*Possion_ratio)*(f1(1,j)+f2
   (1,j)))-nondt/4*(f3(1,j)+f4(1,j))+(Possion_ratio-1)/
   Possion_ratio*nondt/(4*nonr(1,j))*(f1(1,j)+f2(1,j));
F3(1,j)=f3(1,j)+f4(1,j);
F4(1,j)=f4(1,j)-0.5*(f3(1,j)+f4(1,j));
F5(1,j)=f5(1,j)+afa/(2*Possion_ratio)*(f1(1,j)+f2(1,j));
nonW(1,j)=F2(1,j)/(-1-(nondt.^2)/4*(1/(beta.^2)-(
   Possion_ratio-1)/(nonr(1,j).^2)));
nonM(1,j)=0.5*(F1(1,j)-Possion_ratio*nondt/nonr(1,j)*nonW(1,
   j));
nonQ(1,j)=0.5*(F3(1,j)-nondt/(beta.^2)*nonW(1,j));
```

```
nonV(1,j)=F4(1,j)+nondt/(2*beta*nonr(1,j))*nonQ(1,j);
nonN(1,j)=(1+afa/Possion_ratio)*nonM(1,j)-F5(1,j);
nonP(1,j)=0;

for  i=2:m

nonP(i,j)=0;
nonr(i,j)=(2*i-1)*nondt;

f1(i,j)=nonM(i,j-1) + nonW(i,j-1) - (nondt*((nonM(i,j-1) -
   nonN(i,j-1)*Possion_ratio)/nonr(i,j-1) - nonQ(i,j-1) + (
   Possion_ratio*nonW(i,j-1))/nonr(i,j-1)))/2;
f2(i,j)=nonM(i+1,j-1) - nonW(i+1,j-1) - (nondt*(nonQ(i+1,j
   -1) - (nonM(i+1,j-1) - nonN(i+1,j-1)*Possion_ratio)/nonr(
   i+1,j-1) + (Possion_ratio*nonW(i+1,j-1))/nonr(i+1,j-1)))
   /2;
f3(i,j)=nonQ(i,j-1) - nonV(i,j-1) - (nondt*((nonW(i,j-1) -
   ((nonW(i,j-1) - nonW(i+1,j-1))*(beta - 1))/(2*beta))/beta
   ^2 + (nonQ(i,j-1)/nonr(i,j-1) - ((nonQ(i,j-1)/nonr(i,j-1)
    - nonQ(i+1,j-1)/nonr(i+1,j-1))*(beta - 1))/(2*beta))/
   beta))/2 - ((nonQ(i,j-1) - nonQ(i+1,j-1))*(beta - 1))/(2*
   beta) + ((nonV(i,j-1) - nonV(i+1,j-1))*(beta - 1))/(2*
   beta);
f4(i,j)=nonQ(i,j-1) + nonV(i,j-1) - (nondt*((nonW(i,j-1) -
   ((nonW(i,j-1) - nonW(i+1,j-1))*(beta + 1))/(2*beta))/beta
   ^2 - (nonQ(i,j-1)/nonr(i,j-1) - ((nonQ(i,j-1)/nonr(i,j-1)
    - nonQ(i+1,j-1)/nonr(i+1,j-1))*(beta + 1))/(2*beta))/
   beta))/2 - ((nonQ(i,j-1) - nonQ(i+1,j-1))*(beta + 1))/(2*
   beta) - ((nonV(i,j-1)- nonV(i+1,j-1))*(beta + 1))/(2*beta
   );
f5(i,j)=nonM(i,j-1)/2 + nonM(i+1,j-1)/2 - nonN(i,j-1)/2 -
   nonN(i+1,j-1)/2 + (afa*nondt*(nonW(i,j-1)/(2*nonr(i,j-1))
    + nonW(i+1,j-1)/(2*nonr(i+1,j-1))))/2;

F1(i,j)=f1(i,j)+f2(i,j);
```

```
F2(i,j)=f2(i,j)-0.5*(f1(i,j)+f2(i,j))+Possion_ratio*nondt
   /(2*nonr(i,j))*(f5(i,j)+afa/(2*Possion_ratio)*(f1(i,j)+f2
   (i,j)))-nondt/4*(f3(i,j)+f4(i,j))+(Possion_ratio-1)/
   Possion_ratio*nondt/(4*nonr(i,j))*(f1(i,j)+f2(i,j));
F3(i,j)=f3(i,j)+f4(i,j);
F4(i,j)=f4(i,j)-0.5*(f3(i,j)+f4(i,j));
F5(i,j)=f5(i,j)+afa/(2*Possion_ratio)*(f1(i,j)+f2(i,j));

nonW(i,j)=F2(i,j)/(-1-(nondt.^2)/4*(1/(beta.^2)-(
   Possion_ratio-1)/(nonr(i,j).^2)));
nonM(i,j)=0.5*(F1(i,j)-Possion_ratio*nondt/nonr(i,j)*nonW(i,
   j));
nonQ(i,j)=0.5*(F3(i,j)-nondt/(beta.^2)*nonW(i,j));
nonV(i,j)=F4(i,j)+nondt/(2*beta*nonr(i,j))*nonQ(i,j);
nonN(i,j)=(1+afa/Possion_ratio)*nonM(i,j)-F5(i,j);

end

wert=3;

else
for i=2:m
nonP(i,j)=0;
nonr(i,j)=(2*i-1)*nondt;

f1(i,j)=nonM(i-1,j-1) + nonW(i-1,j-1) - (nondt*((nonM(i-1,j
   -1) - nonN(i-1,j-1)*Possion_ratio)/nonr(i-1,j-1) - nonQ(i
   -1,j-1) + (Possion_ratio*nonW(i-1,j-1))/nonr(i-1,j-1)))
   /2;
f2(i,j)=nonM(i,j-1) - nonW(i,j-1) - (nondt*(nonQ(i,j-1) - (
   nonM(i,j-1) - nonN(i,j-1)*Possion_ratio)/nonr(i,j-1) + (
   Possion_ratio*nonW(i,j-1))/nonr(i,j-1)))/2;
f3(i,j)=nonQ(i-1,j-1) - nonV(i-1,j-1) - (nondt*((nonW(i-1,j
   -1) - ((nonW(i-1,j-1) - nonW(i,j-1))*(beta - 1))/(2*beta)
   )/beta^2 + (nonQ(i-1,j-1)/nonr(i-1,j-1) - ((nonQ(i-1,j-1)
```

```
   /nonr(i-1,j-1) - nonQ(i,j-1)/nonr(i,j-1))*(beta - 1))/(2*
   beta))/beta))/2 - ((nonQ(i-1,j-1) - nonQ(i,j-1))*(beta -
   1))/(2*beta) + ((nonV(i-1,j-1) - nonV(i,j-1))*(beta - 1))
   /(2*beta);
f4(i,j)=nonQ(i-1,j-1) + nonV(i-1,j-1) - (nondt*((nonW(i-1,j
   -1) - ((nonW(i-1,j-1) - nonW(i,j-1))*(beta + 1))/(2*beta)
   )/beta^2 - (nonQ(i-1,j-1)/nonr(i-1,j-1) - ((nonQ(i-1,j-1)
   /nonr(i-1,j-1) - nonQ(i,j-1)/nonr(i,j-1))*(beta + 1))/(2*
   beta))/beta))/2 - ((nonQ(i-1,j-1) - nonQ(i,j-1))*(beta +
   1))/(2*beta) - ((nonV(i-1,j-1)- nonV(i,j-1))*(beta + 1))
   /(2*beta);
f5(i,j)=nonM(i-1,j-1)/2 + nonM(i,j-1)/2 - nonN(i-1,j-1)/2 -
   nonN(i,j-1)/2 + (afa*nondt*(nonW(i-1,j-1)/(2*nonr(i-1,j
   -1)) + nonW(i,j-1)/(2*nonr(i,j-1))))/2;

F1(i,j)=f1(i,j)+f2(i,j);
F2(i,j)=f2(i,j)-0.5*(f1(i,j)+f2(i,j))+Possion_ratio*nondt
   /(2*nonr(i,j))*(f5(i,j)+afa/(2*Possion_ratio)*(f1(i,j)+f2
   (i,j)))-nondt/4*(f3(i,j)+f4(i,j))+(Possion_ratio-1)/
   Possion_ratio*nondt/(4*nonr(i,j))*(f1(i,j)+f2(i,j));
F3(i,j)=f3(i,j)+f4(i,j);
F4(i,j)=f4(i,j)-0.5*(f3(i,j)+f4(i,j));
F5(i,j)=f5(i,j)+afa/(2*Possion_ratio)*(f1(i,j)+f2(i,j));

nonW(i,j)=F2(i,j)/(-1-(nondt.^2)/4*(1/(beta.^2)-(
   Possion_ratio-1)/(nonr(i,j).^2)));
nonM(i,j)=0.5*(F1(i,j)-Possion_ratio*nondt/nonr(i,j)*nonW(i,
   j));
nonQ(i,j)=0.5*(F3(i,j)-nondt/(beta.^2)*nonW(i,j));
nonV(i,j)=F4(i,j)+nondt/(2*beta*nonr(i,j))*nonQ(i,j);
nonN(i,j)=(1+afa/Possion_ratio)*nonM(i,j)-F5(i,j);

% clamped point
nonr(m+1,j)=(m+1)*2*nondt;
nonP(m+1,j)=0;
```

```
nonQ(m+1,j)=(1/beta*(nonQ(m,j-1)-nonV(m,j-1))+(beta-1)/(2*
   beta)*nonQ(m+1,j-2)-nondt/(2*beta.^3)*nonW(m,j-1)-nondt
   /(2*beta.^2)*nonQ(m,j-1)/nonr(m,j-1)-(beta-1)/(4*beta.^2)
   *nondt*nonQ(m+1,j-2)/nonr(m+1,j-2))/((beta+1)/(2*beta)
   +(3*beta-1)/(4*(beta.^2)*nonr(m+1,j))*nondt);
%nonM(m+1,j)=(-nondt*Possion_ratio/nonr(m+1,j)*nonM(m+1,j-2)
   +nondt*Possion_ratio/(2*nonr(m+1,j))*nonN(m+1,j-2)+nonM(m
   ,j-1)+nonW(m,j-1)-nondt*Possion_ratio/(2*nonr(m,j-1))*
   nonW(m,j-1)-nondt/(2*nonr(m,j-1))*(nonM(m,j-1)-
   Possion_ratio*nonN(m,j-1))+0.5*nondt*(nonQ(m+1,j)+nonQ(m,
   j-1)))/(1+nondt/(2*nonr(m+1,j))-nondt*Possion_ratio/nonr(
   m+1,j));
nonM(m+1,j)=(-nondt*Possion_ratio/(2*nonr(m+1,j))*nonM(m+1,j
   -2)+nondt*Possion_ratio/(2*nonr(m+1,j))*nonN(m+1,j-2)+
   nonM(m,j-1)+nonW(m,j-1)-nondt*Possion_ratio/(2*nonr(m,j
   -1))*nonW(m,j-1)-nondt/(2*nonr(m,j-1))*(nonM(m,j-1)-
   Possion_ratio*nonN(m,j-1))+0.5*nondt*(nonQ(m+1,j)+nonQ(m,
   j-1)))/(1+nondt/(2*nonr(m+1,j))-nondt*Possion_ratio/(2*
   nonr(m+1,j)));
%nonN(m+1,j)=2*nonM(m+1,j)-2*nonM(m+1,j-2)+nonN(m+1,j-2);
nonN(m+1,j)=nonM(m+1,j)-nonM(m+1,j-2)+nonN(m+1,j-2);
nonW(m+1,j)=0;
nonV(m+1,j)=0;

% origin point

nonP(1,j)=0;
nonQ(1,j)=0;
nonW(1,j)=0;
%nonM(1,j)=4*(1+Possion_ratio)/(4+Possion_ratio*(4-sqrt(12))
   )*((-Possion_ratio*sqrt(12))/(4*(1+Possion_ratio))*nonM
   (1,j-2)+(1+nondt/(2*nonr(1,j-1)))*nonM(1,j-1)-(1+
   Possion_ratio*nondt/(2*nonr(1,j-1)))*nonW(1,j-1)-nondt/2*
   nonQ(1,j-1)-Possion_ratio*nondt/(2*nonr(1,j-1))*nonN(1,j
   -1));
```

```
nonM(1,j)=(nonM(1,j-1)*(1+nondt/(2*nonr(1,j-1)))-nondt*
   Possion_ratio/(2*nonr(1,j-1))*nonN(1,j-1)-(1+
   Possion_ratio*nondt/(2*nonr(1,j-1)))*nonW(1,j-1)-0.5*
   nondt*nonQ(1,j-1)-Possion_ratio/(4*(1+Possion_ratio))*
   nonM(1,j-2))/((4+3*Possion_ratio)/(4+4*Possion_ratio));
%nonV(1,j)=-(nonQ(1,j-1)/beta-nonV(1,j-2)/8+nonV(1,j-1)/beta
   +(nonV(1,j-2)*(beta - 1))/(2*beta)+(nondt*(nonQ(1,j-1)/(
   beta*nonr(1,j-1))-((beta - 1)*(nonP(1,j)/4+nonP(1,j-2)
   /4-0.25*(beta*(nonV(1,j-2)-nonV(1,j-4))/nondt-nonP(1,j-2)
   -nonP(1,j-4))+(nonV(1,j-2)*beta)/(4*nondt)))/(2*beta)))
   /(2*beta)+(nondt*(nonP(1,j)+nonP(1,j-1)/beta+((beta - 1)
   *(nonP(1,j)+nonP(1,j-2)))/(2*beta)))/(2*beta)-(nonP(1,j)*
   nondt)/(8*beta)-(nonP(1,j-2)*nondt)/(8*beta)-(nonW(1,j-1)
   *nondt)/(2*beta^3))/((9*(beta - 1))/(16*beta)-7/8);
nonV(1,j)=(1/beta*nonQ(1,j-1)+1/beta*nonV(1,j-1)-nondt/(2*
   beta.^3)*nonW(1,j-1)+nondt/(2*beta.^2)*nonQ(1,j-1)/nonr
   (1,j-1)+(3*beta-4)/(8*beta)*nonV(1,j-2)-(beta-1)/(16*beta
   )*nonV(1,j-4))/((5*beta+9)/(16*beta));
nonN(1,j)=1/Possion_ratio*nonM(1,j);
nonr(1,j)=0;

end

wert=4;

end

if wert==1

nnn=nnn+1;
% points on the boudary line

nonP(nnn,j)=0;
nonQ(nnn,j)=0;
nonW(nnn,j)=0;
```

```
nonM(nnn,j)=0;
nonV(nnn,j)=0;
nonN(nnn,j)=0;
nonr(nnn,j)=(2*nnn-1)*nondt;

elseif wert==2

% points on the boudary line
nonP(nnn+1,j)=0;
nonQ(nnn+1,j)=0;
nonW(nnn+1,j)=0;
nonM(nnn+1,j)=0;
nonV(nnn+1,j)=0;
nonN(nnn+1,j)=0;
nonr(nnn+1,j)=nnn*2*nondt;

end

end

% 3D plot
%delete the points on the right y-axis

for j=((m+1-ceil((nonr2/(2*nondt))))*2+2):2:(n*2)
nonP(130,j)=NaN;
nonQ(130,j)=NaN;
nonW(130,j)=NaN;
nonM(130,j)=NaN;
nonV(130,j)=NaN;
nonN(130,j)=NaN;
nonr(130,j)=NaN;
nont(130,j)=NaN;
end

%delete the points on the blank area triangle
```

```
limit=ceil((nonr2/(2*nondt)))+1;
for j=1:((m+1-ceil((nonr2/(2*nondt))))*2-1)

if mod(j,2)==0
nonP(limit,j)=NaN;
nonQ(limit,j)=NaN;
nonW(limit,j)=NaN;
nonM(limit,j)=NaN;
nonV(limit,j)=NaN;
nonN(limit,j)=NaN;
nonr(limit,j)=NaN;
nont(limit,j)=NaN;

for i=(limit+1):m
nonP(i,j)=NaN;
nonQ(i,j)=NaN;
nonW(i,j)=NaN;
nonM(i,j)=NaN;
nonV(i,j)=NaN;
nonN(i,j)=NaN;
nonr(i,j)=NaN;
nont(i,j)=NaN;
end
www=1;

else
nonP(limit,j)=NaN;
nonQ(limit,j)=NaN;
nonW(limit,j)=NaN;
nonM(limit,j)=NaN;
nonV(limit,j)=NaN;
nonN(limit,j)=NaN;
nonr(limit,j)=NaN;
nont(limit,j)=NaN;
```

```
for i=(limit+1):m
nonP(i,j)=NaN;
nonQ(i,j)=NaN;
nonW(i,j)=NaN;
nonM(i,j)=NaN;
nonV(i,j)=NaN;
nonN(i,j)=NaN;
nonr(i,j)=NaN;
nont(i,j)=NaN;
end
www=2;
end

if      www==1
limit=limit+1;
elseif  www==2
nonP(m+1,j)=NaN;
nonQ(m+1,j)=NaN;
nonW(m+1,j)=NaN;
nonM(m+1,j)=NaN;
nonV(m+1,j)=NaN;
nonN(m+1,j)=NaN;
nonr(m+1,j)=NaN;
nont(m+1,j)=NaN;
end


end

% use meshgrid to plot 3D figure

rrr=1:1:(m+1);
ttt=1:1:(2*n+1);
[T,R]=meshgrid(ttt,rrr);
```

```
mesh((R-1)*2*nondt,(T-1)*nondt,nonM)
%mesh((R-1)*2*nondt,(T-1)*nondt,nonN*Possion_ratio)
%xlabel(' Normalized coordinate \xi','fontsize',4);
%ylabel('Normalized time \tau','fontsize',4);
%zlabel('$\overline{\it M}$','Interpreter','latex','fontsize
   ',4,'Rotation',0,'FontWeight','bold');
%set(get(gcf,'CurrentAxes'),'FontSize',8);

xlabel('Normalized coordinate \xi','rotation',25,'Position'
   ,[25,-50,-0.05]);
ylabel('Normalized time \tau','rotation',-23,'Position'
   ,[70,60,-0.05]);
zlabel('$\overline{\it M}$','Interpreter','latex','fontsize'
   ,4,'Rotation',0,'FontWeight','bold','Position'
   ,[-22,20,0]);
set(get(gcf,'CurrentAxes'),'FontSize',8);


%set(get(gca, 'xlabel'), 'Rotation', 25);
%set(get(gca, 'ylabel'), 'Rotation', -23);
grid on
grid minor
%view(90,0);
view(0,90)

view(-45,45)
view(45,45)
%zlim([-0.033 0.033])

% use normal mesh to plot
%nonN*Possion_ratio
%plot(nont(39,1:166),-E*nonM(39,1:166))

%mesh(nonr,nont,nonM)
%view(180,180)
```

```
%colorbar;

nonNN=nonN*Possion_ratio;

% use normal mesh to plot
%nonN*Possion_ratio
%plot(nont(39,1:166),-E*nonM(39,1:166))

%mesh(nonr,nont,nonM)
%view(180,180)
%view(90,0)
%colorbar;
%axis([0 60 -0.07 0.07]);
```

A.2 K and I Calculation

```
clear;
clc;
%clf;
close all

plate1 = importdata('plate2.csv');

filename = 'load_CYL.k';%gave my own name
fp = fopen(filename,'w'); %opens the plate1.k, the 'w' means
    write access, fp is the file ID?
fprintf(fp, '*KEYWORD\n');
fprintf(fp, '*INITIAL_VELOCITY_NODE\n');
fprintf(fp,'$#   nid        vx        vy        vz\n');

x = plate1(:,2);
```

```
y = plate1(:,3);
Scale_c = 1; %Factor to scale between the two universities
%W = 78 / (Scale_c^3);
CylinderFit = importdata('Fit.csv');
xc = CylinderFit(:,1)/Scale_c; %scaled distance in m
yc = CylinderFit(:,2)/Scale_c; %specific impulse in Ns/m^2

distance = (x.^2 + y.^2).^(0.5); %distance
p = 1180; %density kg/m3
th = 6.35*10^-3; %thickness m
specific_impulse = pchip(xc,yc,distance);
specific_impulse(distance>108) = 0;
velocity = specific_impulse/(p*th);
plot3(x,y,velocity,'k.','linestyle','none')
view([-187 32])

for k = 1:size(plate1,1)
if distance(k) < 108
fprintf(fp,'%10s',num2str(plate1(k,1))); %node number
fprintf(fp,'%10s',num2str(0));
fprintf(fp,'%10s',num2str(0));
fprintf(fp,'%10s',num2str(velocity(k)));
fprintf(fp,'\n');
end
end


elearea = ones(size(x)) * (2E-3)^2;
elearea(x==0) = elearea(x==0)*0.5;
elearea(y==0) = elearea(y==0)*0.5;

span = 108E-3;
KElower_model = (sum(specific_impulse .* elearea))^2 / (2 *
   p * th * ((pi * span^2)/4));
```

```
KEupper_model = sum(specific_impulse.^2 .* elearea / (2 * p
   * th));

KElower_plate = 4 * KElower_model;
KEupper_plate = 4 * KEupper_model;
K=sqrt(KEupper_plate/KElower_plate)
Impulse = (sum(specific_impulse .* elearea)) * 4
```

Appendix B

Sensitivity Analysis Results

B.1 Sensitivity Analysis Results

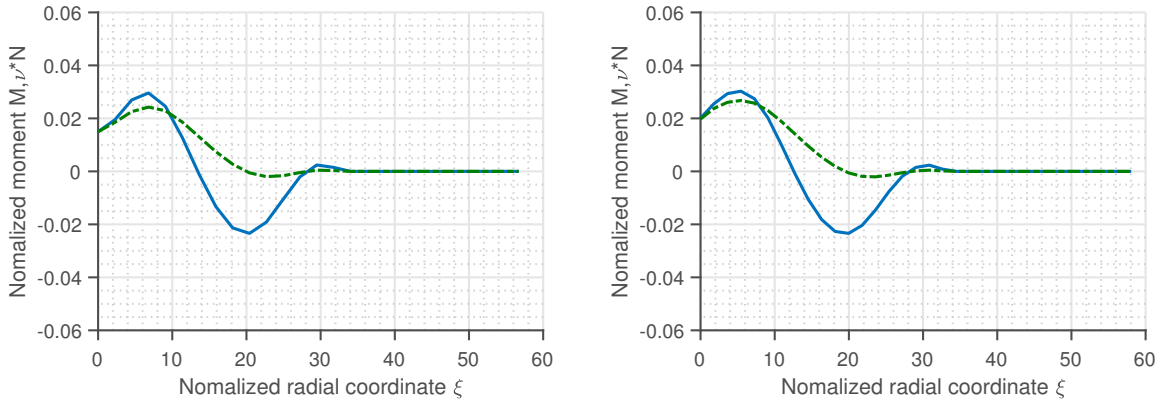

(a) $t = 15\ \mu s, \Delta t = 1\ \mu s$

(b) $t = 15\ \mu s, \Delta t = 0.8\ \mu s$

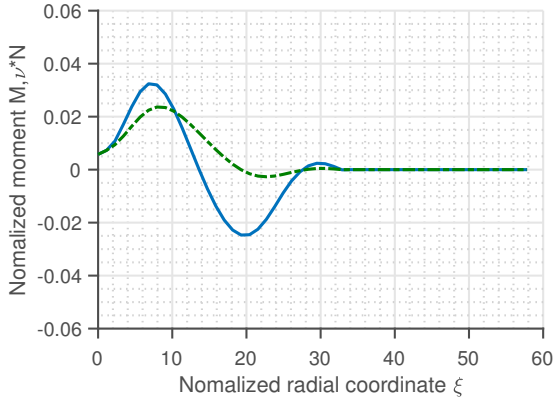

(c) $t = 15\ \mu s, \Delta t = 0.6\ \mu s$

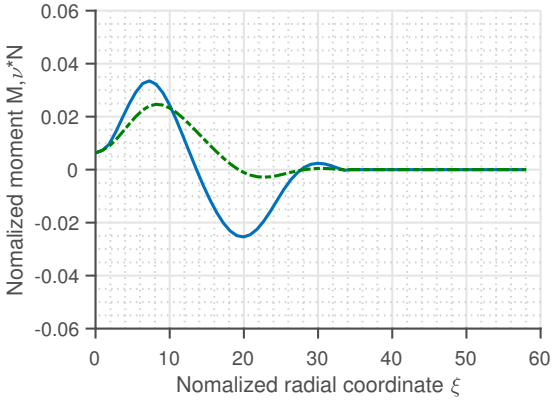

(d) $t = 15\ \mu s, \Delta t = 0.4\ \mu s$

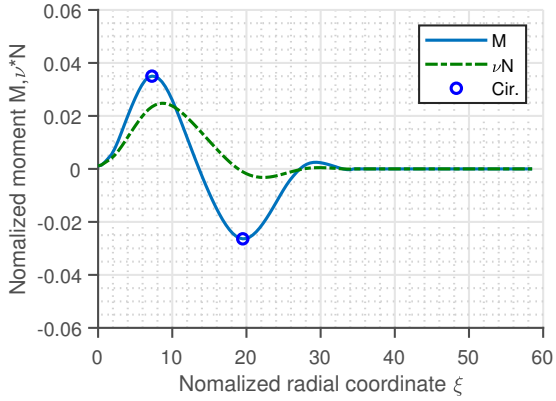

(e) $t = 15\ \mu s, \Delta t = 0.2\ \mu s$

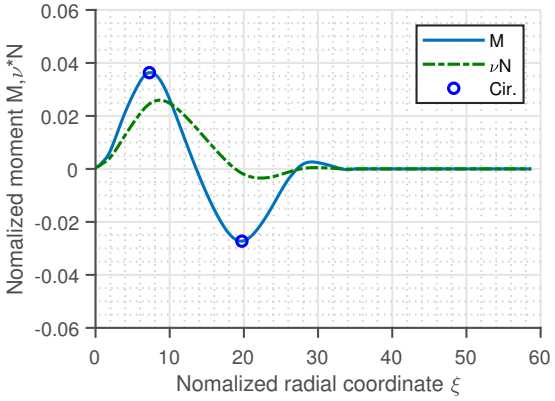

(f) $t = 15\ \mu s, \Delta t = 0.1\ \mu s$

Figure B.1: Calculated bending distribution for a PMMA plate under a bi-linearly initial velocity distribution with $I = 1.44\ Ns$ and $K = 3.76$, "Cir." denotes the circumferential fracture